

NUMERICAL INVESTIGATION OF THICKNESS-TO-CHORD RATIO ON
AERODYNAMIC CHARACTERISTICS AND FLOW FIELD OF A LOW SWEPT
DELTA WING

A THESIS SUBMITTED TO
THE GRADUATE SCHOOL OF NATURAL AND APPLIED SCIENCES
OF
MIDDLE EAST TECHNICAL UNIVERSITY

BY

İSMAİL SADI CESUR

IN PARTIAL FULFILLMENT OF THE REQUIREMENTS
FOR
THE DEGREE OF MASTER OF SCIENCE
IN
MECHANICAL ENGINEERING

SEPTEMBER 2019

Approval of the thesis:

**NUMERICAL INVESTIGATION OF THICKNESS-TO-CHORD RATIO ON
AERODYNAMIC CHARACTERISTICS AND FLOW FIELD OF A LOW
SWEPT DELTA WING**

submitted by **İSMAİL SADI CESUR** in partial fulfillment of the requirements for the degree of **Master of Science in Mechanical Engineering Department, Middle East Technical University** by,

Prof. Dr. Halil Kalıpçılar
Dean, Graduate School of **Natural and Applied Sciences**

Prof. Dr. M. A. Sahir Arıkan
Head of Department, **Mechanical Engineering**

Prof. Dr. Kahraman Albayrak
Supervisor, **Mechanical Engineering, METU**

Assoc. Prof. Dr. M. Metin Yavuz
Co-Supervisor, **Mechanical Engineering, METU**

Examining Committee Members:

Assoc. Prof. Dr. Cüneyt Sert
Mechanical Engineering, METU

Prof. Dr. Kahraman Albayrak
Mechanical Engineering, METU

Assoc. Prof. Dr. M. Metin Yavuz
Mechanical Engineering, METU

Assist. Prof. Dr. Ö. Uğraş Baran
Mechanical Engineering, METU

Assist. Prof. Dr. Ekin Özgirgin Yapıçı
Mechanical Engineering, Çankaya University

Date: 03.09.2019

I hereby declare that all information in this document has been obtained and presented in accordance with academic rules and ethical conduct. I also declare that, as required by these rules and conduct, I have fully cited and referenced all material and results that are not original to this work.

Name, Surname: İsmail Sadi Cesur

Signature:

ABSTRACT

NUMERICAL INVESTIGATION OF THICKNESS-TO-CHORD RATIO ON AERODYNAMIC CHARACTERISTICS AND FLOW FIELD OF A LOW SWEPT DELTA WING

Cesur, İsmail Sadi
Master of Science, Mechanical Engineering
Supervisor: Prof. Dr. Kahraman Albayrak
Co-Supervisor: Assoc. Prof. Dr. M. Metin Yavuz

September 2019, 108 pages

Recent years revealed the increased interest in Unmanned Combat Air Vehicles (UCAVs) and Unmanned Air Vehicles (UAVs) which utilize delta wing planforms, making the Delta wing studies more prominent. Delta wings are characterized by two counter-rotating vortices on leading edges formed by the detached shear layer from the windward side of the planform. Those vortical structures lower the pressures on the suction side of the wing therefore contributes to the increase of the lifting and maneuvering capacity of the wing. Present study, involving Computational Fluid Dynamics (CFD) simulations, investigates the effects of the thickness-to-chord ratio of a low swept delta wing on the aerodynamic characteristics and the flow field.

In the present study, a delta wing planform having a 35 degrees of sweep angle with two thickness-to-chord ratios are numerically examined at Reynolds Numbers, $RE = 35000 \text{ & } 300000$ and angles of attack ranging from 4° to 40° . A mesh independence study is conducted and CFD results are validated by the data of an experimental

study. SST k- ω turbulence model with the extension of curvature correction function is utilized due to its success of yielding the most accurate results.

When flow field results are investigated it is seen that the vortex breakdown phenomena and three-dimensional flow separation occur much sooner with the increase of both thickness-to-chord ratio and Reynolds number, such that in some cases steady vortex structure breaks down right at the apex of the wing. The results also indicate that thickness-to-chord ratio has a significant effect on the aerodynamic coefficients and the flow field, such that, with the increase in t/c ratio drag coefficient, CD increases at all angles of attack, ratio of the lift and drag coefficients, CL/CD decreases. Moreover, CL and Cm values are decreasing with the increase of t/c ratio with the exception for the region till the stall angle of attack is reached. Post stall values of CL and Cm are higher for the thin wing. With the increase in the Reynolds number, all aerodynamic coefficients are increased when it is compared to the lower Reynolds Number results. However, individual trend of the aerodynamic coefficients mentioned above remains the same.

To conclude, the aerodynamic coefficients and flow field are highly affected by the thickness-to-chord ratio, which in turn might prove to be a useful tool to control the flow field, and a step to improve the numerical calculation methods to acquire the vortical structures.

Keywords: Delta Wing, Leading Edge Vortices, CFD, Thickness Effects, Vortex Breakdown, Aerodynamics

ÖZ

KALINLIK VETER ORANININ DÜŞÜK OK AÇILI DELTA KANAT AERODİNAMİK KARAKTERİSTİĞİNE VE AKIŞ YAPISINA ETKİSİNİN NÜMERİK YÖNTEMLERLE İNCELENMESİ

Cesur, İsmail Sadi
Yüksek Lisans, Makina Mühendisliği
Tez Danışmanı: Prof. Dr. Kahraman Albayrak
Ortak Tez Danışmanı: Doç. Dr. M. Metin Yavuz

Eylül 2019, 108 sayfa

Son yıllarda basitleştirilmiş Delta Kanat planfomu kullanan İnsansız Hava Araçları (UAV'ler), Muharip İnsansız Hava Araçlarına (UCAV'ler) olan ilgi artmış, bu yüzden de Delta Kanatlar hakkında yapılan çalışmalar daha önemli hale gelmiştir. Delta Kanatlar hücum kenarından oluşan iki adet tersinir dönüye sahip girdaplı yapılar ile karakterize edilirler. Bu girdaplı yapılar kanatların vakum tarafı olarak adlandırılan üst yüzeylerindeki basınçları düşürerek kaldırma kuvveti manevra kabiliyetlerinin artmasına katkı sağlar. Hesaplamlı Akışkanlar Dinamiği (HAD) içeren bu çalışmada, kalınlık-veter oranının, düşük ok açılı bir Delta Kanadın aerodinamik karakteristiğine ve akış alanına etkileri incelenmektedir.

Çalışmada kullanılan Delta Kanat iki farklı kalınlık-veter oranına ve 35 derece ok açısına sahiptir. HAD çalışması Reynolds Sayısı, $RE = 35000 \text{ & } 300000$ ve hücum açısı $4^\circ, 40^\circ$ arasında yapılmış ve sonuçların bir kısmı daha önce yapılmış deneysel bir çalışmadan alınan veriler ile karşılaştırılmıştır. Analizler sırasında sayısal ağdan bağımsızlık çalışması yapılmış ve isabetli sonuçlar vermesi nedeniyle, SST $k-\omega$ türbülans modeli curvature correction uzantısı ile birlikte kullanılmıştır.

Akım görüntülemeleri yapıldığında fark edilmiştir ki, artan kalınlık-veter oranı ve Reynolds Sayısında girdap bozunumu ve kanat üst yüzeyinden akım ayrılması daha erken kanat istasyonlarında meydana gelmektedir. Bazı koşullarda ise girdaplı yapının bozulmasının direk kanat hücum kenarı uç noktasında meydana geldiği gözükmeğtedir. Bununla beraber, kalınlık-veter oranının kanatların aerodinamik karakteristiği ve akış alanı üzerinde önemli etkileri bulunmaktadır. Kalınlık-veter oranındaki artış ile, tüm hücum açılarında sürükleme kuvveti katsayısı, CD değerlerinin arttığı gözlemlenmiştir. Bununla beraber, taşıma ve sürükleme katsayıları oranı olan CL/CD nin azlığı ortaya çıkmıştır. Ek olarak, kalınlık-veter oranındaki artışla beraber kanatların perdövites hücum açılarının düşüğü gözlemlenmiştir. Taşıma kuvveti katsayısı, CL ve yunuslama momenti katsayısı, Cm değerlerine bakıldığında, kalınlık-veter oranı artışı ile beraber perdövites hücum açısına kadar kalın kanadın daha yüksek değerlere sahip olduğu ancak perdövites sonrasında ince kanadın daha yüksek performansa sahip olduğu görülmektedir. Reynolds Sayısındaki artışla beraber tüm aerodinamik katsayırlarda artış görülmüştür ancak bu katsayılar tek tek incelendiğinde yukarıda bahsedilen davranışın yüksek Reynolds Sayısında da benzer olduğu ortaya çıkmıştır.

Sonuç olarak, aerodinamik karakteristiğin ve akım özelliklerinin, kanadın kalınlık-veter oranından ciddi şekilde etkilendiği ortaya çıkmıştır ki bu durum Delta Kanatlarda akım kontrolü, ve girdaplı yapıların nümerik elde edilmesi konularında önemli bir adım oluşturacağı düşünülmektedir.

Anahtar Kelimeler: Delta Kanat, Hücum Kenarı Girdapları, HAD, Kalınlık Etkileri, Girdap Bozunumu, Aerodinamik

To my parents

ACKNOWLEDGEMENTS

I would like to express my heartfelt appreciation to my thesis supervisors, Prof. Dr. Kahraman Albayrak and Assoc. Prof. Dr. Mehmet Metin Yavuz for their ever-ending guidance, criticism and insight throughout this thesis work.

I would like to express my deepest gratitude to my parents Feride and Raşit Cesur for their eternal love, patience and understanding, for they have provided me a motivational reserve that can never be depleted and a relentless support, giving me strength to get through all the tight spots that I have encountered in my life.

I would also like to thank my friends Dr. Ender Özden, Dr. Fatih Sağlam, Gökay Canal, Görkem Demir and Burak Gülsaçan for their mindful advices and mentoring without which this thesis would not have been realized.

TABLE OF CONTENTS

ABSTRACT	v
ÖZ	vii
ACKNOWLEDGEMENTS	x
TABLE OF CONTENTS	xi
LIST OF TABLES	xiii
LIST OF FIGURES	xiv
LIST OF SYMBOLS	xix
CHAPTERS	
1. INTRODUCTION	1
1.1. Motivation of the Study	6
1.2. Aim of the Study	7
2. LITERATURE REVIEW	9
2.1. Flow Over Delta Wings.....	9
2.1.1. Leading Edge Vortices.....	9
2.1.2. Vortex Breakdown.....	12
2.1.3. Aerodynamic Characteristics	14
2.1.4. Vortex Wandering.....	16
2.1.5. Shear Layer Instability.....	16
2.2. Vortex Flow Control Over Delta Wings	18
2.3. Effects of Thickness-to-Chord Ratio.....	26
2.4. Numerical Studies	32
3. SIMULATION MODEL AND VALIDATION STUDY	41

3.1. Flow Domain, Boundary Conditions	41
3.2. Grid Generation.....	44
3.3. Solver Parameters	46
3.3.1. Reynolds Averaging and Boussinesq Approximation.....	47
3.3.2. Shear-Stress Transport (SST) k- ω Turbulence Model	48
3.4. Grid Independence	51
3.5. The Validation Study	61
4. EFFECTS OF THICKNESS-TO-CHORD RATIO	69
4.1. Flow Visualization	71
4.1.1. Near Surface Patterns	72
4.1.2. Cross-Flow Patterns	82
4.2. Aerodynamic Performance	91
5. CONCLUSIONS	99
5.1. Summary and Conclusions.....	99
5.2. Recommendations for Future Work.....	100
REFERENCES	101

LIST OF TABLES

TABLES

Table 2.1. Vortex Breakdown Location of Turbulence Models [34].....	37
Table 3.1. Dimensions of the flow domain in the simulations in terms of root chord	41
Table 3.2. Details of the boundary conditions	43
Table 3.3. Mesh information.....	44
Table 3.4. Mesh quality metrics	44
Table 3.5. Under-Relaxation factors	46
Table 3.6. Coordinates of the tracking points	53
Table 3.7. The location and Cp value of the suction peak with $t/c = 0.0475$ at varying angles of attack.....	63
Table 3.8. The location and Cp value of the suction peak with $t/c = 0.1900$ at varying angles of attack.....	65
Table 4.1. The CFD matrix used in the numerical analysis	70

LIST OF FIGURES

FIGURES

Figure 1.1. A slender delta wing with vortical structures formed from leading edge [3].....	2
Figure 1.2. Vortex breakdown visualization of a slender delta wing in a water tunnel test, resulting from a colored dye emission near apex [4]	3
Figure 1.3. Interaction of burst strake vortex with control surfaces and twin tail of NASA's F-18 High Angle of Attack Research Vehicle (HARV) [5]	4
Figure 1.4. Near surface streamlines on non-dimensional velocity magnitude contours [6].....	5
Figure 2.1. A generic schematic of the flow field over the top surface of a delta wing [5].....	10
Figure 2.2. Relation between vortical structure and the pressure variation [10]	11
Figure 2.3. Axial velocity distribution of the vortex core before breakdown [8].....	11
Figure 2.4. Spiral and bubble type vortex breakdown [12]	12
Figure 2.5. Spiral type vortex breakdown [14]	13
Figure 2.6. Iso-surfaces of Q-criterion: Standard Roe's scheme (left); Hybrid scheme (middle and right) [16].....	14
Figure 2.7. Lifting characteristics for flat plate delta wings having different sweep angles [8]	15
Figure 2.8. Illustration of free shear layer, viscous sub core and rotational core over a delta wing [25].....	17
Figure 2.9. Illustration of free shear layer, viscous sub core and rotational core over a delta wing [28].....	18
Figure 2.10. Passive flow control and delayed vortex breakdown in tandem configuration [29]	20

Figure 2.11. Surface pressure coefficient distribution variance affected by passive bleeding technique [31].....	21
Figure 2.12. Aerodynamic coefficients with varying apex and leading-edge flap angles [4].....	22
Figure 2.13. Joint PIV measurements and dye flow visualization photos showing the LEV breakdown location at 25 degrees angle of attack [4].....	22
Figure 2.14. Plasma actuator control conducted on a slender delta wing [32]	23
Figure 2.15. Avoiding vortex breakdown by trailing edge blowing [33]	24
Figure 2.16. Non-dimensional axial velocity contour at a plane passing through the vortex core for a) non-controlled case, and b) controlled case [34].....	25
Figure 2.17. Maximum lift-drag ratio as a function of thickness-to-chord ratio [40]	27
Figure 2.18. Pressure coefficient distribution at axial station at $x/c = 0.5$ [43]	28
Figure 2.19. Lift coefficient CL with respect to angle of attack for varying t/c at RE = 35000 [43].....	29
Figure 2.20. Lift and drag coefficients, Cl and Cd [44].....	30
Figure 2.21. Lift-drag ratio with varying angle of attack [44]	30
Figure 2.22. Effect of thickness-to-chord ratio on drag coefficient with varying Mach number [45]	31
Figure 2.23. Comparison of surface pressures and experimental data (a) $x/c = 0.5$, (b) $x/c = 0.8$ [16]	32
Figure 2.24. Isosurface of non-dimensional axial vorticity & non-dimensional axial vorticity contour at $x/c = 0.53$ [46]	33
Figure 2.25. Numerical (left) and experimental (right) axial and transversal velocity contours [47]	34
Figure 2.26. Cp distribution extracted from unsteady (DES) and steady (SARC&SST) computations along with experimental data [48]	35
Figure 2.27. Results for numerical models, SA (left), EARSM (middle), HBY0 (right) a) Streamlines at $x/c = 0.4$, b) Surface pressure coefficient distributions [49]	36

Figure 2.28. Vorticity contours at axial station $x/c = 0.3$ with a flap angle of 70° on the leading edge [50]	36
Figure 2.29. Axial velocity contour passing through vortex line with base wing (left) and trailing-edge jet flap (right) [53]	38
Figure 2.30. Comparison of normalized velocity components at $x/c = 0.4$ [61]	39
Figure 3.1. Wing models with $t/c = 0.019, 0.047, 0.1142, 0.1900$	42
Figure 3.2. Representation of the flow field and boundary conditions	43
Figure 3.3. Surface and body of influence meshes: a) Mesh 4, b) Mesh 6.....	45
Figure 3.4. Near wing symmetry plane meshes: a) Mesh 4, b) Mesh 6	46
Figure 3.5. Scaled residual history of Mesh 5	52
Figure 3.6. Monitor points distribution on leeward and leading-edge surfaces	53
Figure 3.7. Velocity magnitude though iterations a) Point 2 b) Point 7 c) Point 11 .	55
Figure 3.8. $y+$ contour of Mesh 5	56
Figure 3.9. Chordwise stations of pressure coefficient, C_p data extract	57
Figure 3.10. Pressure coefficient, $-C_p$ profiles of chordwise stations a) $x/c = 0.4$, b) $x/c = 0.6$	58
Figure 3.11. Pressure coefficient, $-C_p$ Contours a) Mesh 1 b) Mesh 2 c) Mesh 3 d) Mesh 4, e) Mesh 5, f) Mesh 6.....	59
Figure 3.12. Aerodynamic coefficients of four meshes, a) CL, b) CD.....	60
Figure 3.13. The comparison of the dimensionless pressure coefficient distribution, - C_p of $t/c = 0.0475$ along spanwise direction at $x/c = 0.44$ at $RE = 35000$	63
Figure 3.14. The comparison of the dimensionless pressure coefficient distribution, - C_p of $t/c = 0.1900$ along spanwise direction at $x/c = 0.44$ at $RE = 35000$	65
Figure 3.15. The comparisons of the near surface velocity streamlines of delta wings, a) Experiment with $t/c = 0.0475$ (left) & 0.1900 (right), b) CFD with $t/c = 0.0475$ (left) & 0.1900 (right), at $\alpha = 10^\circ$	67
Figure 4.1. Near surface streamlines and surface C_p distributions of delta wing with $t/c = 0.0475$ at $RE = 35000$ and $\alpha = 3^\circ, 5^\circ$ (top), $7^\circ, 9^\circ$ (bottom)	73
Figure 4.2. Near surface streamlines and surface C_p distributions of delta wing with $t/c = 0.1900$ at $RE = 35000$ and $\alpha = 3^\circ, 5^\circ$ (top), $7^\circ, 9^\circ$ (bottom)	74

Figure 4.3. Near surface streamlines and surface Cp distributions of delta wing with $t/c = 0.0475$ at $RE = 300000$ and $\alpha = 3^\circ, 5^\circ$ (top), $7^\circ, 9^\circ$ (bottom)	75
Figure 4.4. Near surface streamlines and surface Cp distributions of delta wing with $t/c = 0.1900$ at $RE = 300000$ and $\alpha = 3^\circ, 5^\circ$ (top), $7^\circ, 9^\circ$ (bottom)	76
Figure 4.5. Near surface streamlines and surface Cp distributions of delta wing with $t/c = 0.0475$ at $RE = 35000$ and $\alpha = 12^\circ, 14^\circ$ (top), $16^\circ, 18^\circ$ (bottom)	77
Figure 4.6. Near surface streamlines and surface Cp distributions of delta wing with $t/c = 0.1900$ at $RE = 35000$ and $\alpha = 12^\circ, 14^\circ$ (top), $16^\circ, 18^\circ$ (bottom).....	78
Figure 4.7. Near surface streamlines and surface Cp distributions of delta wing with $t/c = 0.0475$ at $RE = 300000$ and $\alpha = 12^\circ, 14^\circ$ (top), $16^\circ, 18^\circ$ (bottom)	79
Figure 4.8. Near surface streamlines and surface Cp distributions of delta wing with $t/c = 0.1900$ at $RE = 300000$ and $\alpha = 12^\circ, 14^\circ$ (top), $16^\circ, 18^\circ$ (bottom).....	80
Figure 4.9. Near surface streamlines and surface Cp distributions of delta wing with $t/c = 0.0475$ (left), 0.1900 (right) at $RE = 35000$ (top), 300000 (bottom) at $\alpha = 30^\circ$..	81
Figure 4.10. The comparisons of azimuthal vorticity contours of delta wing with $t/c = 0.0475$ at $RE = 35000$ and $\alpha = 3^\circ, 9^\circ$ (top), $14^\circ, 20^\circ$ (bottom) located at $x/c = 0.44$	83
Figure 4.11. The comparisons of turbulent kinetic energy contours of delta wing with $t/c = 0.0475$ at $RE = 35000$ and $\alpha = 3^\circ, 9^\circ$ (top), $14^\circ, 20^\circ$ (bottom) located at $x/c = 0.44$	84
Figure 4.12. The comparisons of azimuthal vorticity contours of delta wing with $t/c = 0.1900$ at $RE = 35000$ and $\alpha = 3^\circ, 9^\circ$ (top), $14^\circ, 20^\circ$ (bottom) located at $x/c = 0.44$	85
Figure 4.13. The comparisons of turbulent kinetic energy contours of delta wing with $t/c = 0.1900$ at $RE = 35000$ and $\alpha = 3^\circ, 9^\circ$ (top), $14^\circ, 20^\circ$ (bottom) located at $x/c = 0.44$	86
Figure 4.14. The comparisons of azimuthal vorticity contours of delta wing with $t/c = 0.0475$ at $RE = 300000$ and $\alpha = 3^\circ, 9^\circ$ (top), $14^\circ, 20^\circ$ (bottom) located at $x/c = 0.44$	87

Figure 4.15. The comparisons of turbulent kinetic energy contours of delta wing with $t/c = 0.0475$ at $RE = 300000$ and $\alpha = 3^\circ, 9^\circ$ (top), $14^\circ, 20^\circ$ (bottom) located at $x/c = 0.44$	88
Figure 4.16. The comparisons of azimuthal vorticity contours of delta wing with $t/c = 0.1900$ at $RE = 300000$ and $\alpha = 3^\circ, 9^\circ$ (top), $14^\circ, 20^\circ$ (bottom) located at $x/c = 0.44$	89
Figure 4.17. The comparisons of turbulent kinetic energy contours of delta wing with $t/c = 0.1900$ at $RE = 300000$ and $\alpha = 3^\circ, 9^\circ$ (top), $14^\circ, 20^\circ$ (bottom) located at $x/c = 0.44$	90
Figure 4.18. Comparison of the lift coefficient, CL at $RE = 35000 & 300000$ for $t/c = 0.0475, 0.1900$	91
Figure 4.19. Comparison of the drag coefficient, CD at $RE = 35000 & 300000$ for $t/c = 0.0475, 0.1900$	92
Figure 4.20. Comparison of the CL/CD at $RE = 35000 & 300000$ for $t/c = 0.0475, 0.1900$	93
Figure 4.21. Comparison of the pitching moment coefficient, C_m at $RE = 35000 & 300000$ for $t/c = 0.0475, 0.1900$	94
Figure 4.22. Comparison of the location of the center of pressure ($X_{c.p.}$) at x -axis with respect to angle of attack, at $RE = 35000 & 300000$ for $t/c = 0.0475, 0.1900$..	95
Figure 4.23. Comparison of the lift coefficient, CL at $RE = 35000 & 300000$ for $t/c = 0.0190, 0.0475, 0.1143, 0.1900$	96
Figure 4.24. Comparison of the drag coefficient, CD at $RE = 35000 & 300000$ for $t/c = 0.0190, 0.0475, 0.1143, 0.1900$	96
Figure 4.25. Comparison of the CL/CD values at $RE = 35000 & 300000$ for $t/c = 0.0190, 0.0475, 0.1143, 0.1900$	97

LIST OF SYMBOLS

SYMBOLS

c	Root Chord (RC)
S	Wing Planform Area (m^2)
C _p	Pressure Coefficient
C _L	Lift Coefficient
C _D	Drag Coefficient
C _m	Pitching Moment Coefficient
μ_t	Turbulent Viscosity (Pa.s)
RE	Reynolds Number
U	Axial Velocity (m/s)
α	Angle of Attack (°)
SST	Shear Stress Transport
k	Turbulent Kinetic Energy (m^2/s^2)
X	Cartesian Coordinate – x direction
Y	Cartesian Coordinate – y direction
Z	Cartesian Coordinate – z direction
TKE	Non-dimensional Turbulent Kinetic Energy
CC	Curvature Correction
CFD	Computational Fluid Dynamics
Ω	Vorticity (1/s)

Λ	Sweep Angle ($^{\circ}$)
$y+$	y-plus, A Non-Dimensional Wall Distance
ω	Specific Turbulence Dissipation Rate (1/s)
ρ	Fluid Density (kg/m 3)
ψ	Stream Function
t/c	Thickness-to-chord Ratio
P	Pressure (Pa)
t	Thickness of the Wing

CHAPTER 1

INTRODUCTION

One of the most prominent considerations of the aircraft aerodynamic design process is to maximize the maneuvering capability and to reduce the angle of attack limitations of the planform. For that reason, delta wings have been a topic of great interest due to their characteristics such as high stall angle of attack and cruise speed, even in supersonic speeds, sharp maneuvering capabilities and structural integrity. Many high-performance aircrafts are known to have high-swept delta wings [1].

Delta wings with adequate sweep angles can continue to produce lift up to an angle attack value of 40° [2]. The flow separation from the wing upper surface, the stall, is observed to be at much lower angles of attack for a conventional high aspect ratio wing.

The major classification of the delta wings is based on their sweep angles (Λ). Such wings are called “slender or high swept” as their Λ is higher than 50° and “non slender or low swept” as their Λ is between 35° and 50° . While such geometric difference produces many varieties in the flow field, the general characteristic for the delta wing flows are the same. At certain angles of attack and Reynolds Numbers, two counter-rotating vorticities emanating from the leading edge dominate the flow field on the suction side of delta wing. Those primary vorticities from the leading edge, interacts with the boundary layer at their reattachment region and leads to the formation of secondary, even tertiary vortices. Figure 1.1 gives an example of a delta wing with the vortical flow structures [3].

Another important geometric feature of the delta wings is the leading-edge shape. It can be sharp, rounded with different radii values and it significantly affects the flow field such as the number of stable vorticities and their swirling strengths, how close

the vortex core line is to the leading edge, how soon the vortices are going to breakdown.

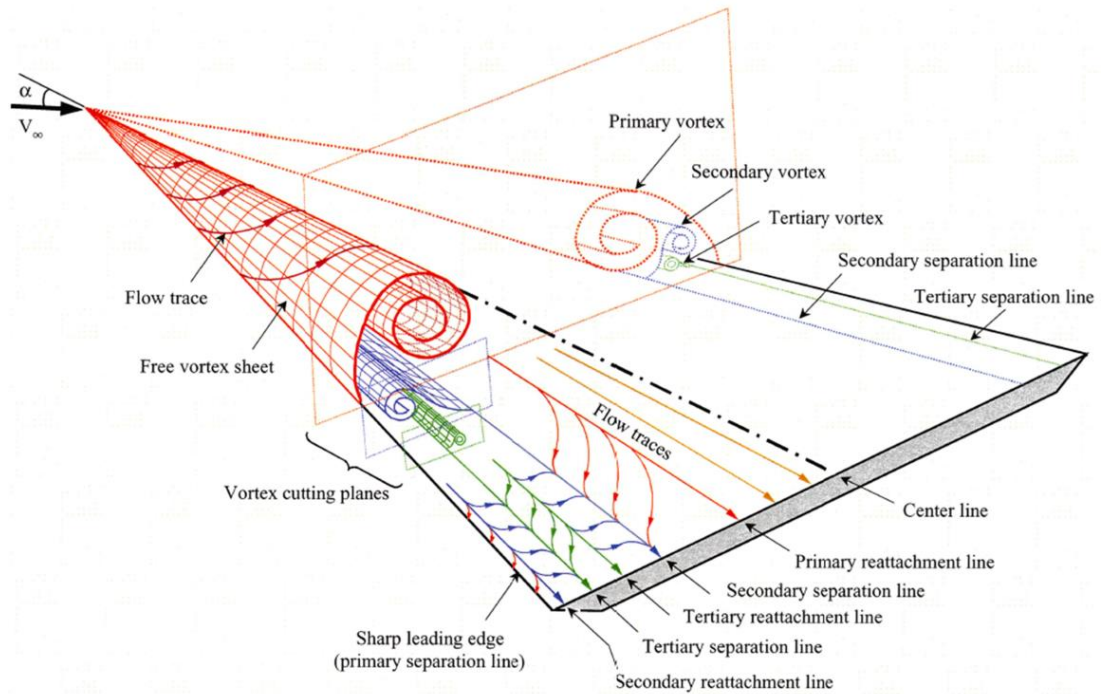


Figure 1.1. A slender delta wing with vortical structures formed from leading edge [3]

When lift generation characteristics are examined for a wing, it is seen that the major component of the force is derived from the momentum difference. For a conventional wing it is the only mechanism in play. On the other hand, when delta wing flows are investigated, it is clear that the stable and strong vortical structures acting as a suction agent on the upper surface (suction side) of the wing, therefore contributing to the lift. However, at a certain angle of attack, depending on the geometry and flight conditions, strong leading-edge vorticities undergo a sudden expansion over the wing, which is known as vortex breakdown or burst. Investigated in detail, axial velocity of the vortex core begins to decrease and eventually reaches a stop. At that instant, pressure and turbulent kinetic energy of the vortex core rises

up and expands. This phenomenon is called Vortex Breakdown, Figure 1.2 shows an apt visualization of vortex breakdown on a slender delta wing in a water tunnel by Lee and Ko [4].

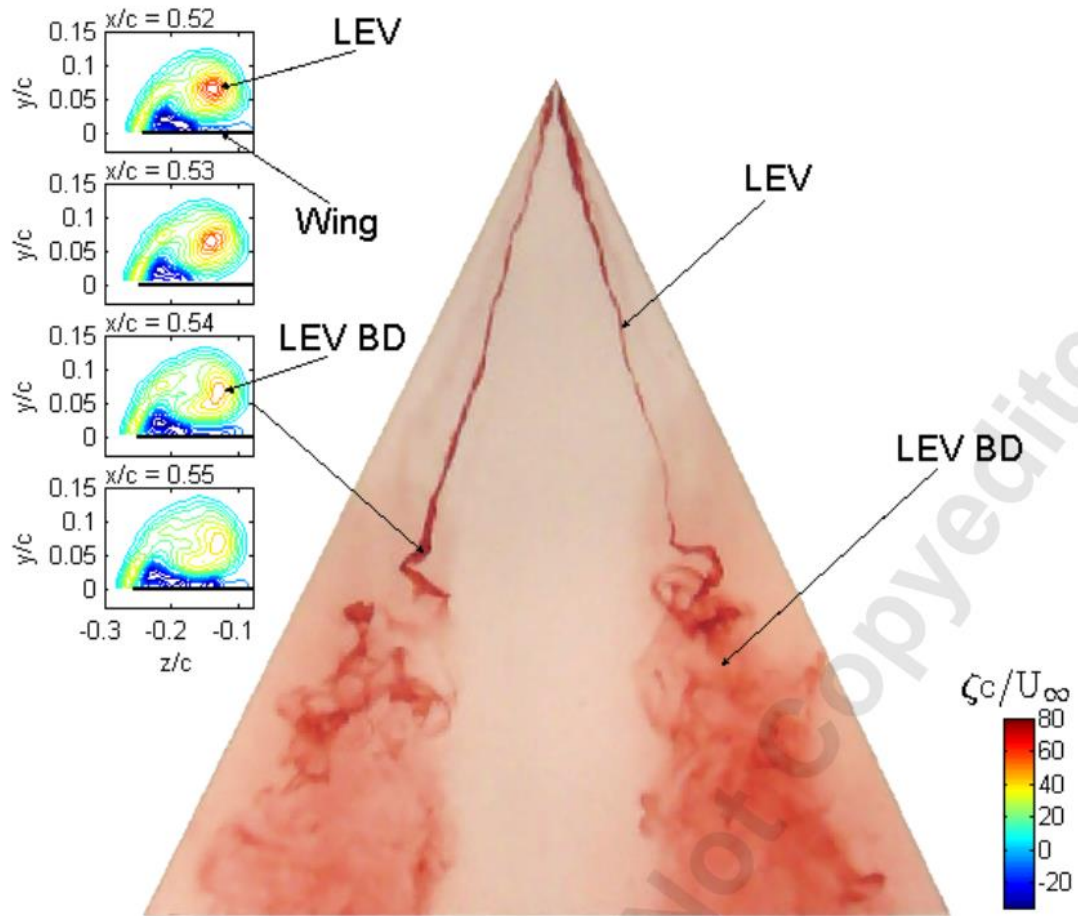


Figure 1.2. Vortex breakdown visualization of a slender delta wing in a water tunnel test, resulting from a colored dye emission near apex [4]

From that point vortical structure loses its strength and increases the pressure on the surface therefore have an adverse effect on lift and also remaining turbulent nature of the vortical structure can lead to unexpected aerodynamics instability and non-uniform loads on the wing surface. As an example, the interaction between the broken-down strake vorticity and the twin tail of NASA's F-18 High Angle of Attack Research Vehicle (HARV) is show in Figure 1.3. These interactions are the

cause of the tail buffet which leads to the structural fatigue and decrease in the performance of aft control surfaces of the aircraft. This severe interaction also causes wing rock phenomena [5].



Figure 1.3. Interaction of burst strake vortex with control surfaces and twin tail of NASA's F-18 High Angle of Attack Research Vehicle (HARV) [5]

Another important phenomenon experienced in the delta wing flows is the 3-D flow separation from the leeward surface. As the angle of attack increase, vortical structure and induced flow begin to move away from the top surface of the wing, making it harder to get attached to the surface. Taylor and Gursul [6] studied the changes in the reattachment lines and found out that as angle of attack increases primary reattachment line move inboards and when it reaches to wing centerline flow separation is about to occur at which delta wing undergoes a sudden loss of lift and stability as it is depicted in Figure 1.4 For that reason, eliminating the 3-D flow

separation is considered to be even more crucial than delaying the vortex breakdown.

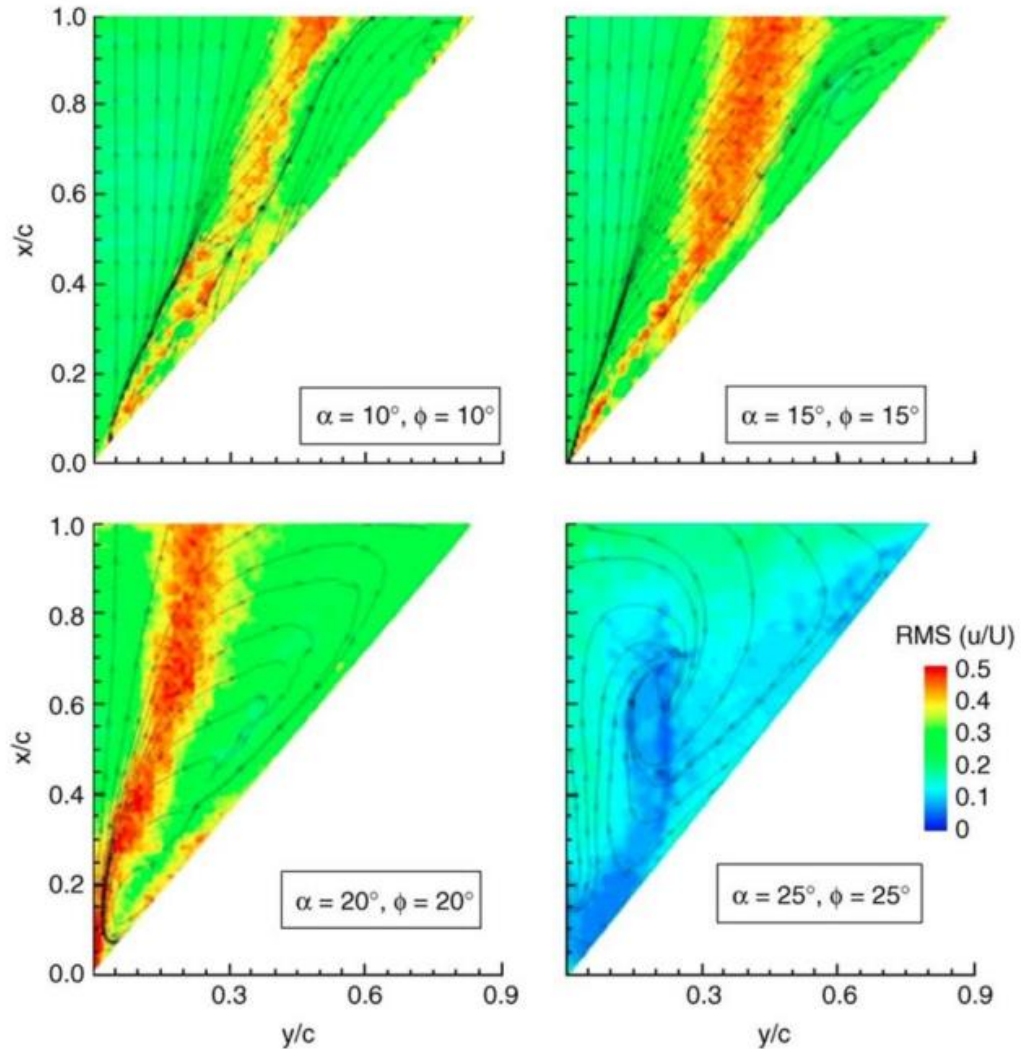


Figure 1.4. Near surface streamlines on non-dimensional velocity magnitude contours [6]

1.1. Motivation of the Study

Delta wing profiles are generally used in the design of unmanned combat aerial vehicles (UCAVs) and micro air vehicles (MAVs) for their additional lift gain from vortical structures and maneuvering capabilities. At adequate Reynolds Numbers and angles of attack those vortical structures break down and three-dimensional separation occurs causing adverse effects on the aerodynamic characteristics such as instability and non-linear aerodynamic coefficients as well as unsteady loading on the wing structure. In order not to suffer from those adverse effects, flow structures are often examined and geometric modifications are applied to eliminate three-dimensional separation.

In the delta wing literature, a small number of studies have been conducted to examine the thickness effects on the aerodynamic forces and flow structure of slender delta wings. An experimental thesis study conducted by Gülsuçan [7] includes the effects of thickness-to-chord ratio of a 35° swept delta wings with t/c of 0.0475, 0.0950, 0.1425 and 0.1900. The free stream velocities were 1.42 and 4.97 m/s which corresponds to Reynolds Numbers of 10000 and 35000 respectively. The results revealed that effects of t/c are as significant as the variations in the angle of attack in terms of vortex breakdown and three-dimensional separation. However, lacking the force balance system, examining effects of high angles of attack and higher Reynolds numbers on the 3-D separation characteristics and aerodynamics performances could not be realized at the time.

CFD modelling of delta wing flow fields are an efficient way to determine what work best under various flight conditions and geometries. Utilizing CFD simulations, models of delta wings with different thickness-to-chord ratios will be analyzed numerically to determine possibility to delay or even eliminate three-dimensional separation and effects on aerodynamic characteristics.

1.2. Aim of the Study

In the present study, effects of the thickness-to-chord ratio (t/c) on the aerodynamics characteristics and flow field of a 35° swept delta wing will be investigated numerically solving steady Reynolds-Averaged Navier-Stokes (RANS) equations with turbulence modelling. For method verification, CFD results are compared with the experimental results for $RE = 35000$ at angles of attack 4° to 10° . After the verification process is completed, simulation models are analyzed on higher Reynolds number and increased angles of attack to examine the thickness effects and to determine aerodynamic forces. Finally, two additional thickness values are considered to see intermediary properties which could not be examined in the previous experimental study [7].

CHAPTER 2

LITERATURE REVIEW

This chapter includes the literature review of leading-edge vortices (LEVs), vortex breakdown on delta wings, aerodynamics characteristics of delta wings, flow instabilities over delta wings regarding, movement of vortices (vortex wandering), shear layer instabilities, flow control techniques, effects of thickness-to-chord ratio and numerical studies which are investigated in detail.

2.1. Flow Over Delta Wings

2.1.1. Leading Edge Vortices

Vorticities are formed as flow separates from the leading-edge of the delta wing by the roll up movement forced by the shear layer and it results in counter-rotating swirling structures. Figure 2.1 shows a generic flow structure above a delta wing [5] where free shear layers created by the separation of the flow forms a line called primary separation line depicted as S1 and reattaches itself at the primary reattachment line A1. Then leading-edge vorticity can enforce the adjacent flow elements to move in the spanwise direction. In some cases, this outward flow may get separated from the leeward surface of the delta wing at the secondary separation line denoted as S2 due to the change in direction of the pressure gradient and form a secondary vortical structure having a negative directional sign with respect to the primary vorticity. This phenomenon can repeat itself to form even tertiary vortices if the flow conditions and geometrical definition of the delta wing allows.

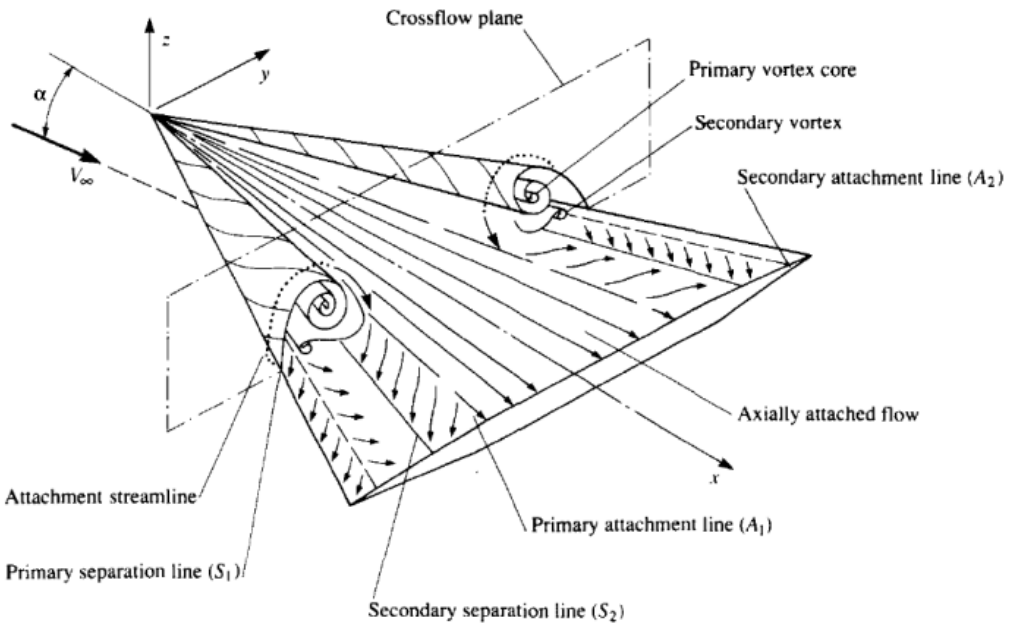


Figure 2.1. A generic schematic of the flow field over the top surface of a delta wing [5]

On the leeward surface, it is observed that, by the influence of the vortical structures, pressures are lowered and higher velocity profiles are achieved with respect to the free-stream properties of the flow. By its nature, stable vortical structures tend to have the highest axial velocity located at the vortex core, meaning that pressures are also going to be the lowest. For that reason, suction peak occurs on the top surface of the delta wing right below the vortex core. Figure 2.2 depicts the relation between vortical structure and pressure variation of the delta wing surface. Moreover, it is seen that the velocity distribution of the primary vortex of is a function of angle of attack [8]. As angle of attack increases, both of the axial and the tangential velocity magnitude of the vortex core increase. The velocity of the vortex core can rise up to 3-4 times of the free-stream velocity depending on the sweep angle of the delta wing [8]. Figure 2.3 shows the relation of the vortex core velocity with increasing angle of attack. Location of the primary vortex core line relocates itself to upwards and more inward as the results of the formation of secondary vorticities. Visbal's work [9] reveals that position and the magnitude of the secondary vortex depends on sweep angle, angle of attack and also Reynolds number. With the increase in the sweep

angle, vortex core line moves inwards and with the increase in the angle of attack, same line tends to move out from the leeward surface. Reynolds number, on the other hand, affects the size of the vortex core.

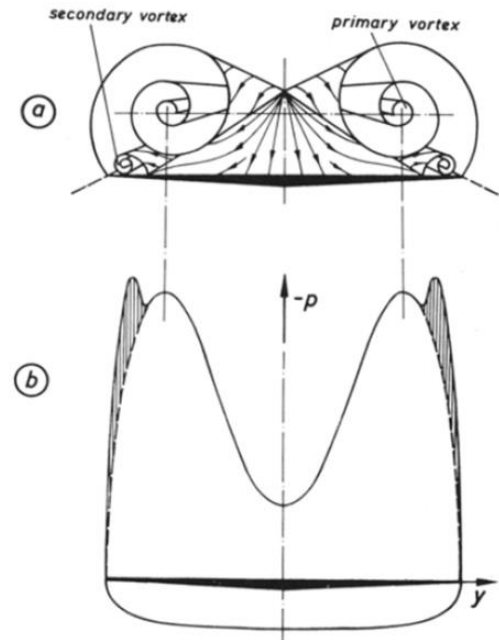


Figure 2.2. Relation between vortical structure and the pressure variation [10]

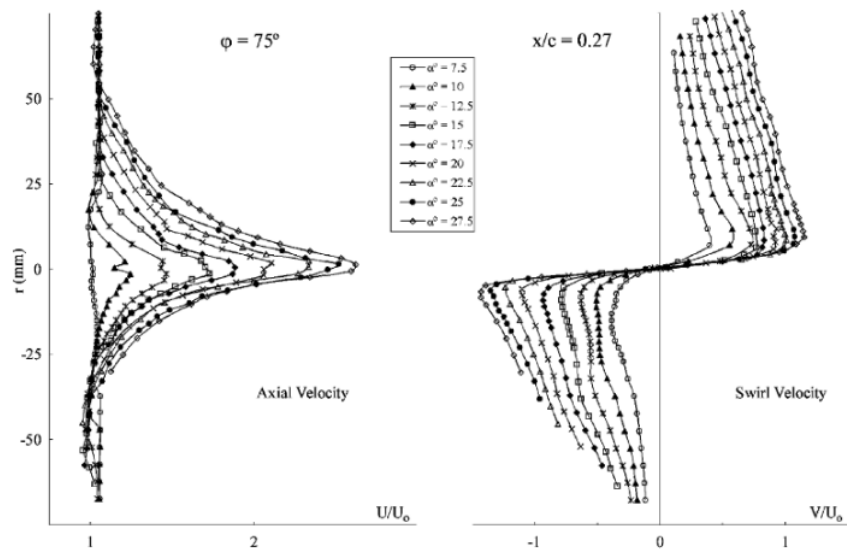


Figure 2.3. Axial velocity distribution of the vortex core before breakdown [8]

2.1.2. Vortex Breakdown

With sufficiently high angle of attack and Reynolds number, also depending on the geometric features of the delta wing, the leading-edge vorticities lose its stability and undergo a sudden expansion on the leeward surface. It is when the axial velocity of the vortex core drops to zero which sometimes called as “vortex stagnation”. Due to the decrease in the velocities, pressure on top surface suddenly increase after breakdown causing the loss of lift of the wing. Vortex breakdown phenomena was first explained by the work of Werle [11].

Studies revealed that there are two different types of breakdown which are called spiral and bubble type breakdown [12]. A detailed view of these types of break down structures are given in the Figure 2.4.

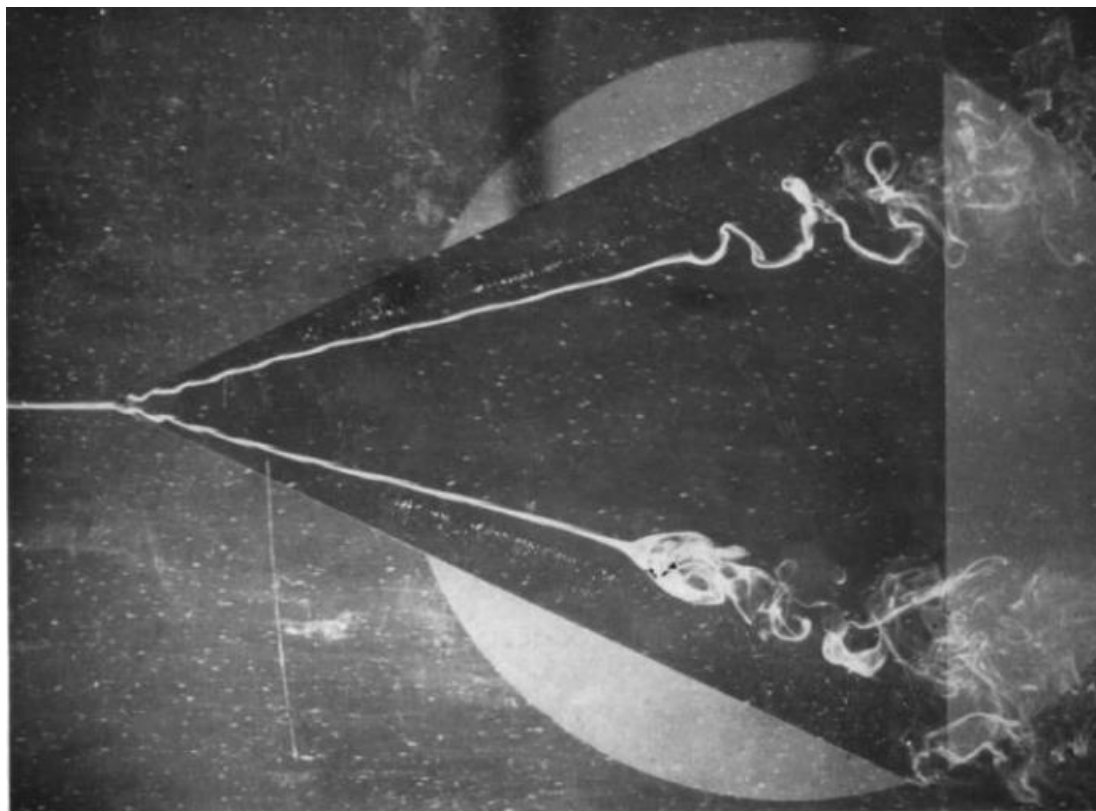


Figure 2.4. Spiral and bubble type vortex breakdown [12]

When the bubble structure is examined, it is seen that the upstream part of the bubble is axisymmetric while the downstream part is breaking into irregular shedding, forming a turbulent wake [13]. On the other hand, the spiral mode puts forth an immediate deceleration of the vortex core, then a sudden kink to take the form of a spiral. Vortex core begins to spiral and continues to do so for two more rotations before breaking into a large-scale turbulence [13]. Figure 2.5 explains the spiral type vortex breakdown.

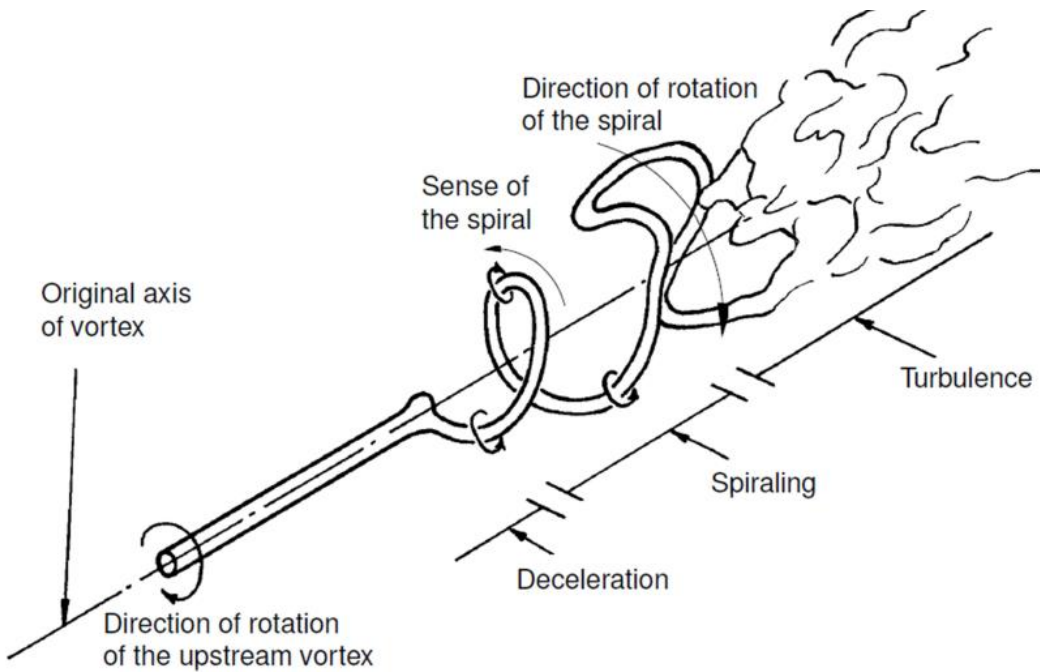


Figure 2.5. Spiral type vortex breakdown [14]

The leading-edge vorticities in the spiral mode also rotates in the same direction with the rotating vortex but the sense of the spiral of the spiral is at the opposite direction. Extensive research suggest that the spiral mode breakdown of the leading-edge vorticities are the most common ones. Moreover, a study conducted by Gursul [15] shows that even bubble type breakdowns switches to spiral mode in tunnel tests. A numerical by Zhang et al. [16] contributed that even bubble and spiral breakdowns are so intertwined that a change in the numerical scheme can turn a bubble

breakdown in to double spiral breakdown. Figure 2.6 shows the numerical results of vortical structures solved with different numerical models.

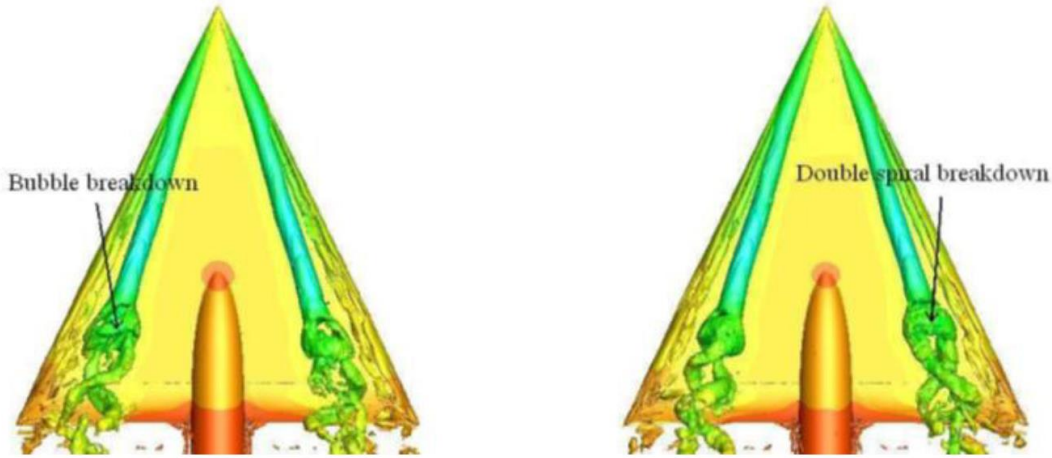


Figure 2.6. Iso-surfaces of Q-criterion: Standard Roe's scheme (left); Hybrid scheme (middle and right) [16]

Due to the adverse effects on the wing performance, vortex breakdown location of the leading-edge vorticities is an important research subject. It is found out that the leading-edge vorticities have a very delicate structure and more than one flow parameter can determine the location of the vortex burst. Most prominent parameters that can affect the location of the vortex breakdown is the sweep angle and the angle of attack of the wing [13]. However, studies showed that flight conditions [17] and shape of the leading edge [18] are also significant.

2.1.3. Aerodynamic Characteristics

Leading-edge vorticities accelerate flow on delta wing leeward surface locally. This accelerated flow field lowers the pressures on top surface leading a decrease in the pressure field forming a suction peak under primary vorticities. Acting as a suction agent, leading-edge vorticities creates additional lift to the potential lift created by the momentum difference induces by wing geometry. This contribution, which is non-linear with respect to the angle of attack, is also known as the vortex lift. Though depending on the sweep angle of the delta wing, lift coefficients are on the

order at most 1.4 for a slender delta wing. Leading-edge vorticities can increase the lift potential up to 60% of the total lift at high angles of attack [5].

Sweep angle is a significant parameter which can determine the location of the vortex breakdown on the wing surface. Hence it holds a significant importance on the delta wing aerodynamic performance. Figure 2.7 reveals the relation between vortex breakdown and lift characteristics of a delta wing with different sweep angles [8].

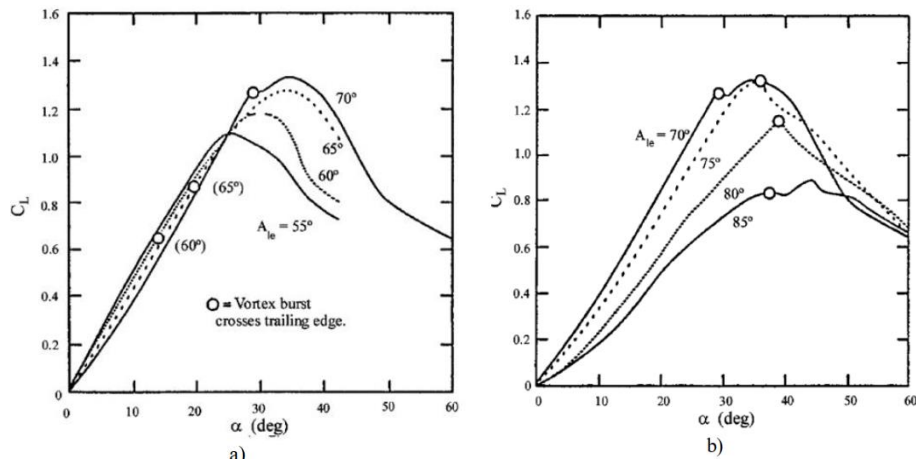


Figure 2.7. Lifting characteristics for flat plate delta wings having different sweep angles [8]

Vortex breakdown occurs at earlier stations on the leeward surface as the angle of attack increase. For non-slender delta wings, vortex breakdown can be seen before the delta wing reaches its maximum lift coefficient (before stall). However, when it comes to the case with highly swept delta wings, vortex breakdown is much closer to the trailing edge of the wing when it is subjected to same angles of attack.

In both cases, the effects of the vortex breakdown phenomenon are the same. The loss of lift and pitching moment coefficient [15]. Moreover, vortex breakdown is also the source of the well-known adverse effect, wing buffeting on slender delta wings [6]. Wing buffeting is highly unsteady and known to cause loss in stability.

2.1.4. Vortex Wandering

Vortex wandering can be defined as the arbitrary change in the location of the vortex core axis at the leeward surface of the delta wing [19]. In the work of Menke et al. [20], large velocity oscillations are present while the vortex breakdown does not even exist. Same observations for the shifting behavior of the vortex core line are made by other studies as well [20, 21]. Another study by Cornelius [22] exhibits the wandering phenomena over an aircraft model. Degani. et al. [23] examined this behavior for an ogive cylinder geometry.

Though it is known to be irrespective of Reynolds number, there are some studies made to understand the reasons behind vortex wandering. One of the reasons of vortex wandering was suggested is the amplitude of freestream turbulence intensity [23, 24]. However, work of Menke and Gursul contradicted those suggestions by showing that the displacement in the vortex core line is much higher to be caused by the free stream turbulence [20]. Since the exact nature of the vortical structures are still elusive, the strongest arguments about the reason for the wandering behavior are currently the unsteady turbulent wake effects and highly non-linear interactions of small eddies with the leading-edge vorticities.

2.1.5. Shear Layer Instability

As viscous flow theory explains, the boundary layer separation occurs because of the creation of the adverse pressure gradient caused by the interaction between the free stream flow and the body. When separation occurs mainline boundary layer profile distribution becomes invalid and the flow then becomes highly turbulent. On delta wings separation always occurs at the sharp leading-edge and creates three distinct regions in the flow field. By Earnshaw's study [25], those regions are identified in the Figure 2.8 as the viscous sub core, rotational core and free shear layer.

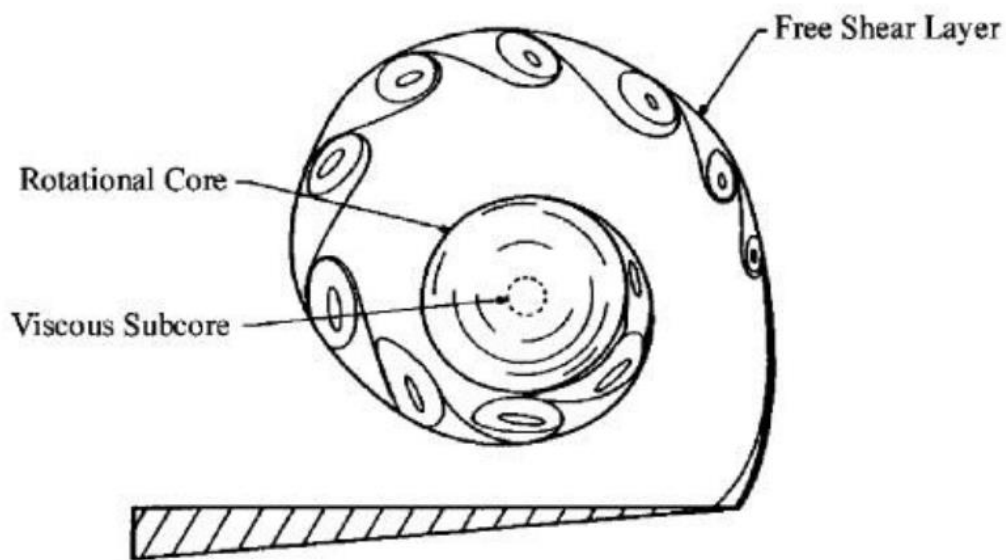


Figure 2.8. Illustration of free shear later, viscous sub core and rotational core over a delta wing [25]

Moreover, Özgören et al. [26] explains that the shear layer instabilities are also caused by the unsteady nature of the delta wing flows which is consistent with the results of the study by Riley and Lawson [27].

Another study by Gordnier and Visbal [28] suggested that the shear layer instability is arises from the vortex wandering caused by the expansion from the secondary vortex structure interacting with the leading-edge vorticities. Figure 2.9 shows the vortical structure and shear layer instability on a slender delta wing.

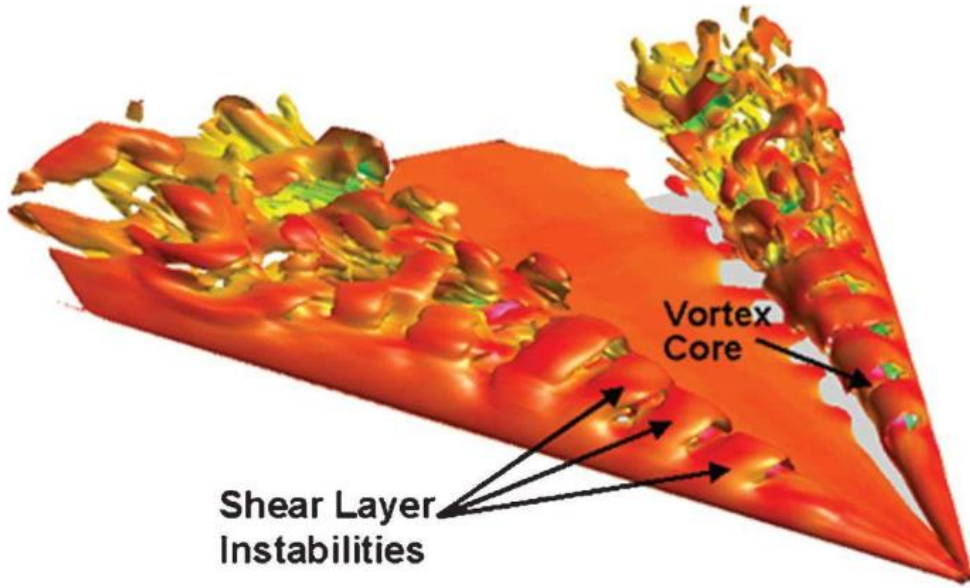


Figure 2.9. Illustration of free shear layer, viscous sub core and rotational core over a delta wing [28]

2.2. Vortex Flow Control Over Delta Wings

As aforementioned before, vortical structures have significant effects on flow field and aerodynamics characteristics of the delta wings. Since presence of a strong and stable vorticities with vortex cores having high axial velocities contributes to the lift capacity of the wing, contrarily a prematurely broken vortex structure has adverse effects as loss in lift and pitching moments, creating non-linear aerodynamic characteristics and making control of the wing much harder. For apparent reasons, scientists began searching for successful and applicable control methods to delay or even eliminate vortex breakdown phenomena on the leeward surface of the delta wings. Though current control methods do not possess a conclusive superior effectiveness to one another regarding vortex breakdown location or increasing aerodynamic capabilities, methods can be individually applied to solve a specific problem on a platform to achieve the desired results.

Two important parameters play a significant role resulting in the vorticities to breakdown in the flow field. One is the swirl ratio which is responsible for

decreasing the tangential velocity component. Methods that aim to adjust the swirl level to delay the vortex breakdown simply tries to increase the longevity of the stable vortex and increase the axial velocity of the vortex core. This is achieved by adding streamwise momentum to vortical structures to overcome the adverse pressure gradient effects which is the other parameter at hand to control the life of a stable vortex. Vortical flows on delta wings tend to create a high-pressure field propagating from the trailing edge to the apex of the wing. Confronting an adverse pressure gradient stable vortical structures cannot push through and lose its core velocity at each station getting closer to the trailing edge. Methods involving the manipulation of this adverse pressure gradient tries to lower the pressure at the trailing edge, creating less resistance for stable vortex structure to overcome while changing the whole flow field at the downstream.

Generally, the flow control methods for leading-edge vorticities and vortex breakdown falls under two categories as passive and active control techniques. Passive control methods involve mechanical devices such as canards, strakes and forebodies used in combination with the main wing body to form multiple vortex structures. Idea is to generate an energizing flow field at the upstream for the vortical flow on the main wing and by that interaction, delaying the vortex breakdown of leading-edge vorticities. Multiple vortex structures can be seen at tandem or canard-wing configurations. Figure 2.10 [29] depicts a tandem delta wing configuration and the location change of vortex breakdown with varying angle of attack. Due to the geometry change, life of the stable vortex structure is prolonged in different angles of attack and since the vortex breakdown is delayed at much later stages on the leeward surface, aerodynamic characteristics are improved. Also, the structural oscillation effects of the elastic wing with shear layer instabilities supports the reattachment of the flow causing an increase in the lift [30].

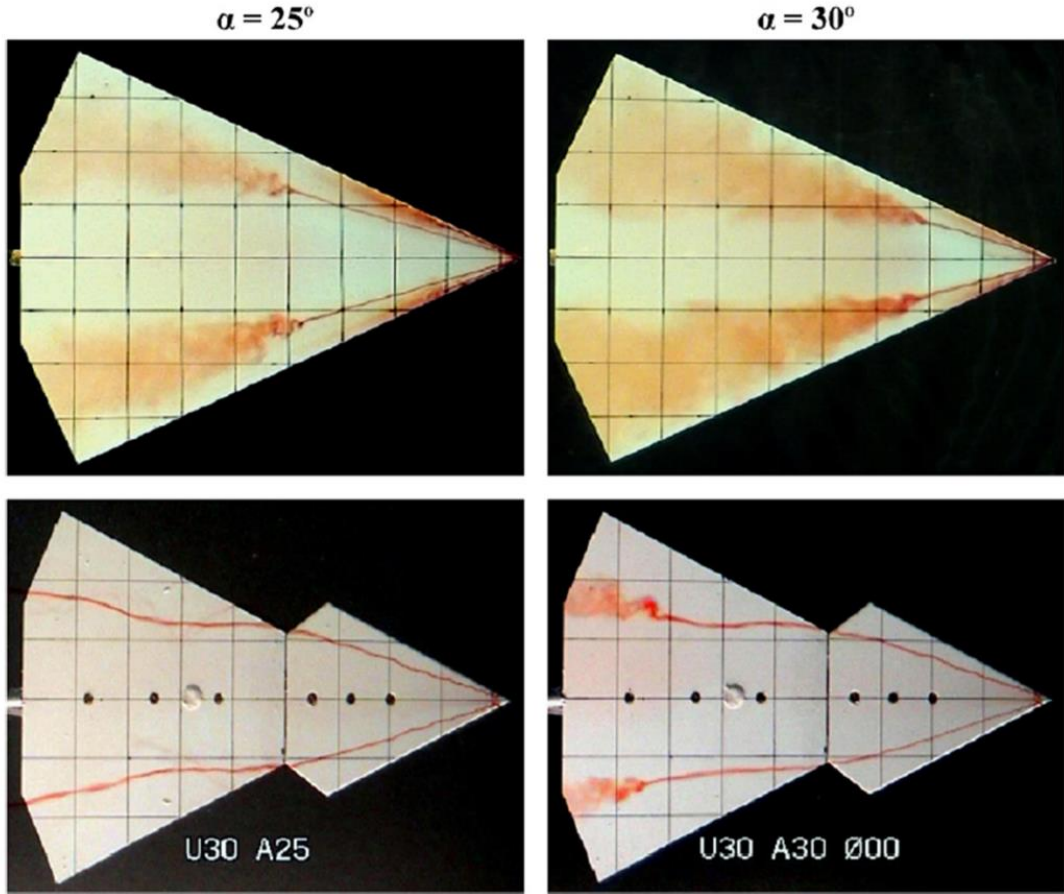


Figure 2.10. Passive flow control and delayed vortex breakdown in tandem configuration [29]

Another passive control technique, a novel method modifying the flow field of the delta wing, is bleeding which involves the passage of air from the pressure side to the suction side. Yavuz et al. [31] employed passive bleeding on a 45° swept delta wing in a low speed wind tunnel using laser-illuminated smoke visualization, surface pressure measurements and PIV. Platforms are tested under various angles of attack and Reynolds numbers. Results show that passive bleeding method alter the flow field over the platform providing a significant improvement on the flow patterns. Figure 2.11 shows the distribution of pressure coefficient distribution on the leeward surface where the base wing experiences a three-dimensional surface separation.

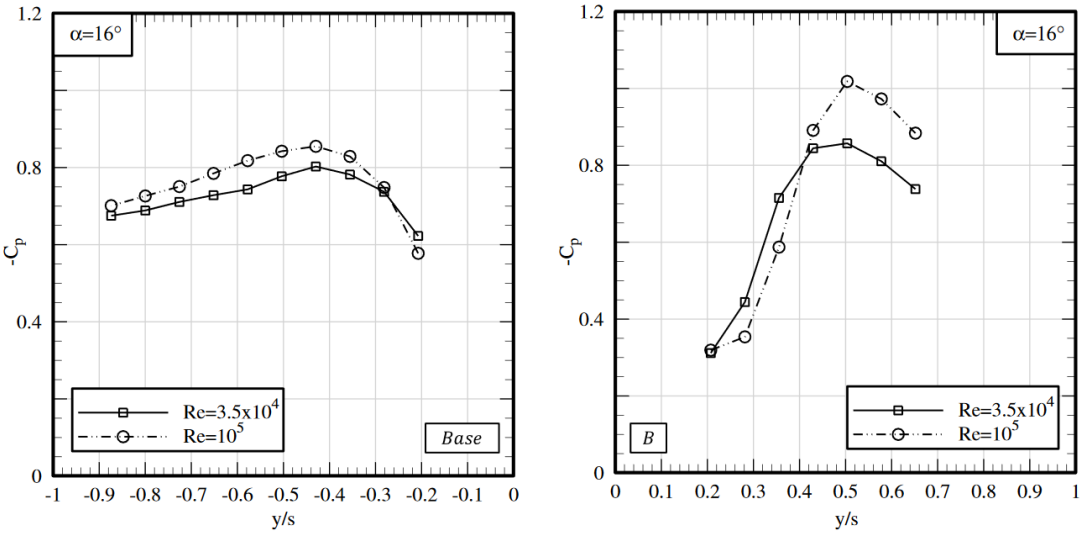


Figure 2.11. Surface pressure coefficient distribution variance affected by passive bleeding technique [31]

As it is widely known that surface pressure coefficient distribution becomes flattened after vortex breakdown occurs. By passive bleeding technique, suction peak is still present at the station where the base wing is experiencing vortex breakdown and three-dimensional surface separation.

Active flow control techniques can be summarized under three categories as being control surfaces, plasma actuators and blowing or suction with pneumatic devices. Leading-edge and apex flaps or extensions are utilized mainly to alter the angle of attack or sweep angle or to manipulate the separation at both leading edges to affect creation and the strength of the vortical structure whose nature determines the location of vortex breakdown and aerodynamic characteristics of the delta wing. A study conducted by Lee et al. [4] utilized the control of apex and leading-edge flaps to investigate its effects on the vortex breakdown location and found out that joint apex and leading-edge flap deflections gave a delayed leading-edge vortex breakdown and enhanced lift. Figure 2.12 shows the results of the water tunnel experiments for the flap effects on the aerodynamic characteristics. Figure 2.13 shows the effect of tip and leading-edge flapping to the location of the vortex breakdown.

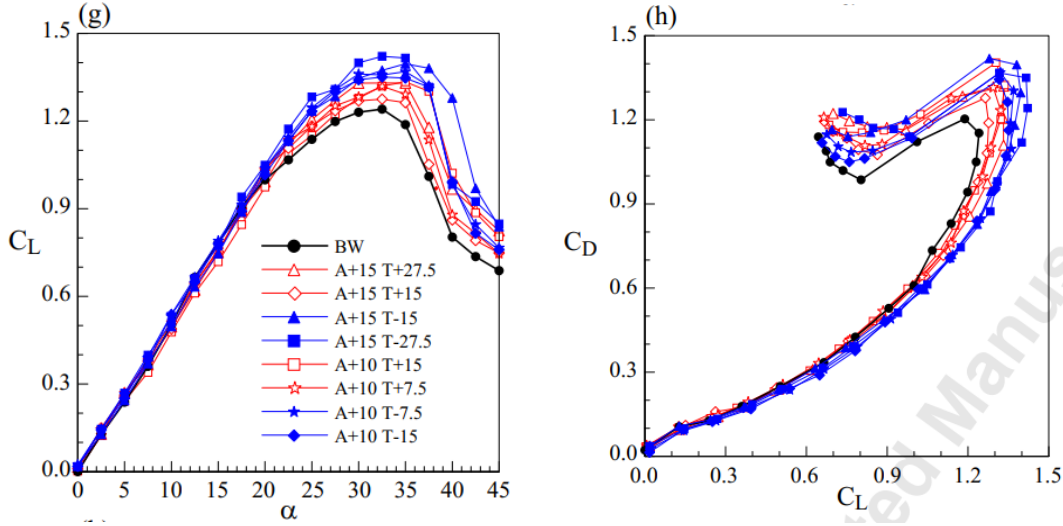


Figure 2.12. Aerodynamic coefficients with varying apex and leading-edge flap angles [4]

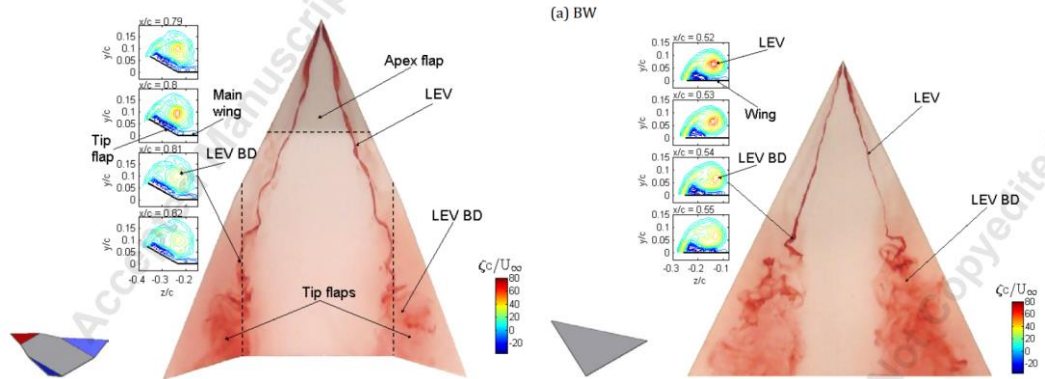


Figure 2.13. Joint PIV measurements and dye flow visualization photos showing the LEV breakdown location at 25 degrees angle of attack [4]

Moreover, Visbal and Gaitonde [32] studied the plasma actuators and shown in the Figure 2.14 that the breakdown was completely avoided and the vortex core line is preserved by the effect of wall originated plasma actuator near wing apex.

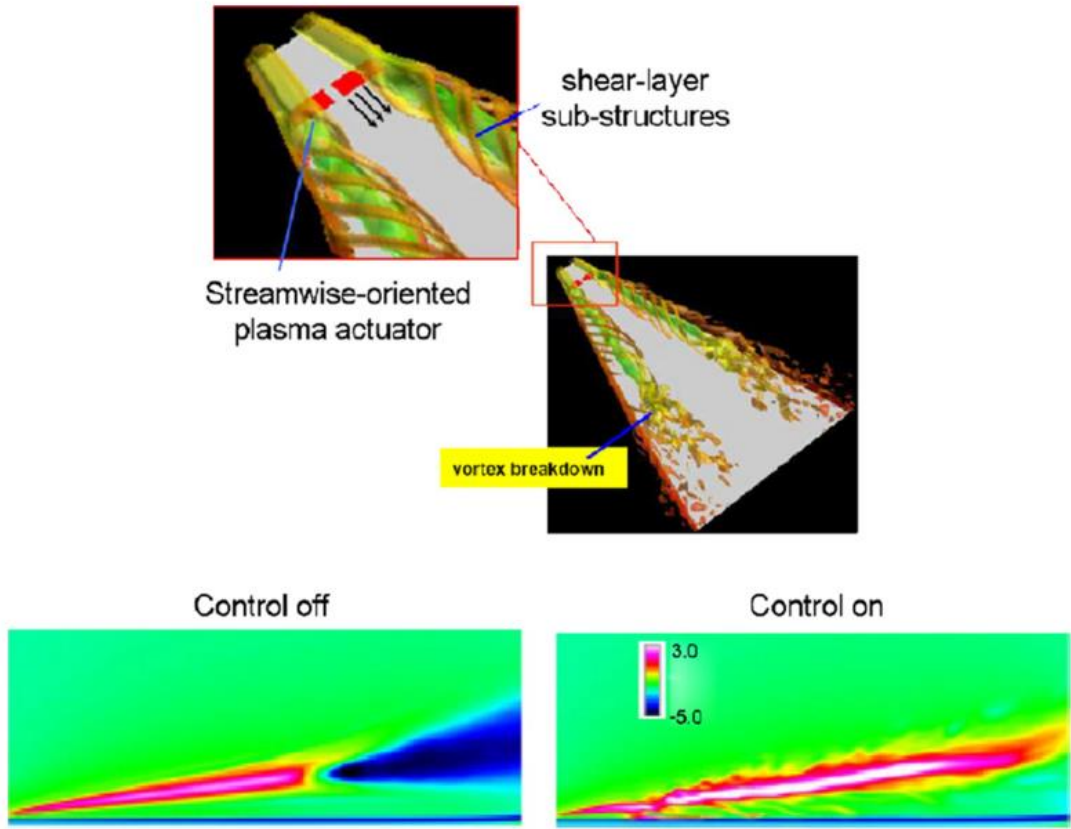


Figure 2.14. Plasma actuator control conducted on a slender delta wing [32]

The pneumatic devices are used in the flow control methods varies on the locations in which they are applied and in manners. Applications involve, span wise blowing, tangential blowing, leading-edge blowing, along the vortex core blowing, trailing edge blowing and at same stations suction are applied. In Figure 2.15 Gursul et al. [33] used the trailing edge blowing technique to overcome the adverse pressure gradient which causes vortex breakdown on the leeward surface when no flow control method was utilized. This application is an example of modifying the pressure field downstream to lower the pressure on the trailing edge so that vortical structures are not affected by the high-pressure fields.

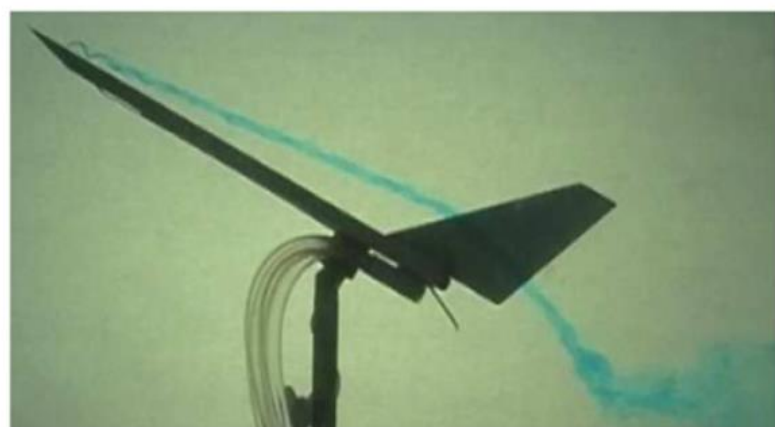


Figure 2.15. Avoiding vortex breakdown by trailing edge blowing [33]

A numerical study conducted by Küçükyılmaz [34] showed in the Figure 2.16 that the vortex breakdown is delayed at a closer station to the trailing edge by along-the-core blowing technique.

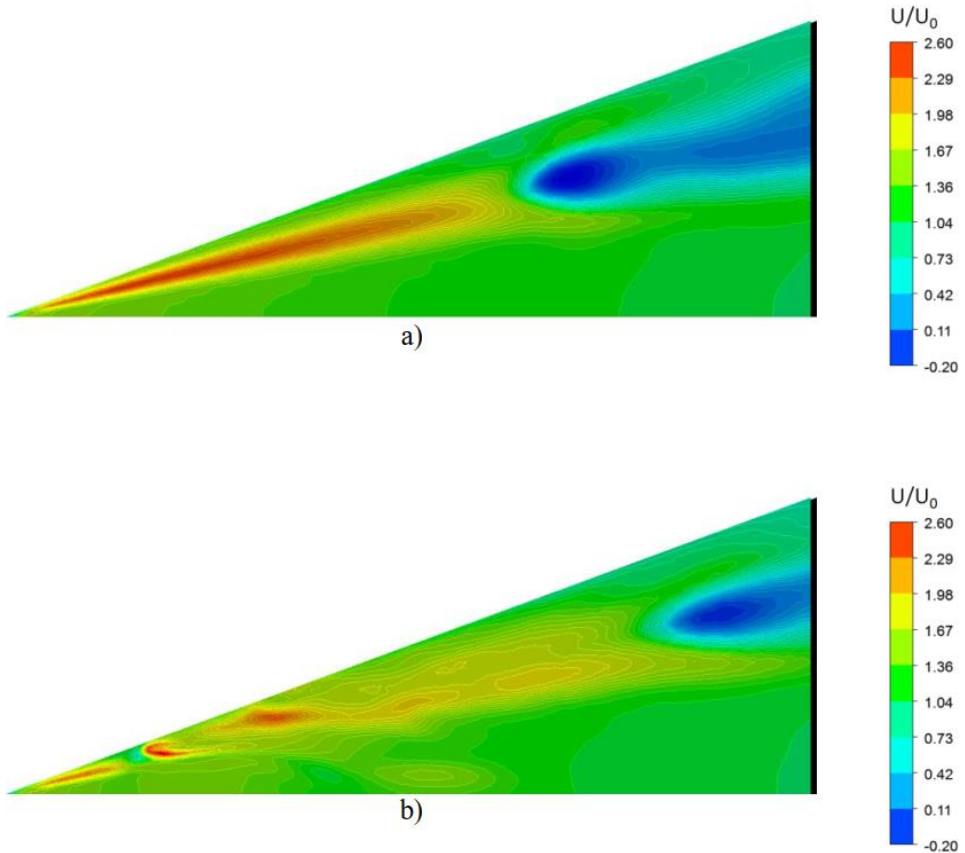


Figure 2.16. Non-dimensional axial velocity contour at a plane passing through the vortex core for a) non-controlled case, and b) controlled case [34]

The usage of pneumatic devices on such applications is to reduce the minimum energy requirements to control the flow field. The energy required to manipulate the flow field into a desired outcome is called the effectiveness of the control method. Although each technique is beneficial in its own application a general effectiveness consideration is made to compare the active control methods. In his work, Gursul et al. [29] made a general assessment for active control methods and ranked their effectiveness with respect to each other.

Another type of flow control mechanism involves an unsteady manipulation method. The unsteady effects can be grouped under low and high frequency excitation. The high frequency methods aim to modify the instabilities caused by the vortical

structures. On the other hand, low frequency methods tend to control the axial pressure gradient to influence the vortex behavior. The occurrence of the vortex breakdown is due to the rapid expansion of the flow structure caused by the unstable disturbances. For that reason, including a well-formed perturbation in the flow field by an unsteady method can influence the flow to put the vortex breakdown forward. A strong control method is to introduce high frequency excitation to successfully achieve the control, then frequency is reduced to match natural frequency of the vortex instabilities [35]. Also, small deflectional oscillations given found to be effective when it is compared with the non-controlled case [29].

2.3. Effects of Thickness-to-Chord Ratio

Throughout the research history for the delta wing flows, thickness effects are examined in different ways. While many scientists considered the thickness effects as the modifications made in the leading edge [36], others strived to observe the change in the flow domain when thickness of the delta wing changed. In his work Delery [37] emphasized the importance of the usage of sharp leading-edges on delta wings and made statements which suggest improvements on the flow topology by increasing the thickness, about Werle [38]'s experiments on thick and round leading-edge delta wing. Peckham [39] found out that increasing the thickness of the delta wing causes the vortex system to move outboard. Witcofski and Marcum Jr. [40] made wind tunnel experiments to observe the effects of wing thickness and sweep angle on the longitudinal aerodynamic characteristics. Delta wings had sweep angles between 45 and 90 degrees and thickness-to-chord ratios of 0 and 0.3. Reynolds numbers vary between 1.4×10^6 to 6.6×10^6 and the angle of attack ranged from 0° to 30° . Figure 2.17 shows the results of the experiments that maximum lift-drag ratios tends to have a linear decrease when thickness-to-chord ratio of the wing is increased. Same study also points out that optimum sweep angle for maximizing the lift-drag ratio decreases from an angle of 80° to 70° for the highest thickness-to-chord ratio as t/c increases.

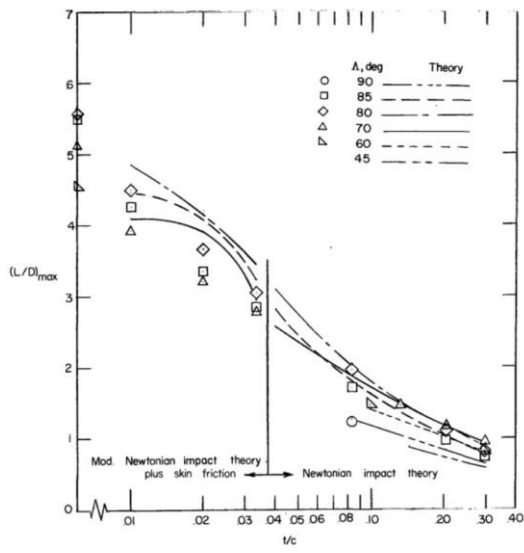


Figure 2.17. Maximum lift-drag ratio as a function of thickness-to-chord ratio [40]

Lawson and Riley [41] examined the location of the vortex breakdown when wings have similar sweep angles. Although many studies stated that results are the same when the leading-edge is kept sharp, he realized that the results for similar model slender delta wing geometries vary. Main reason for that difference was thickness-to-chord ratio. It is found out that decrease in the wing thickness results in moving out the vortex breakdown location to the aft with a variation of angle of attack by 5° to 7° . Wang and Lu [42] contributed by studying both leading-edge bevel angle and thickness-to-chord ratio on delta wing with a sweep angle of 50° . Experiments are made with delta wings with t/c ratios as 2%, 6.7% and 10%. Delta wing having 2% t/c had 30° , 45° and 60° windward and leeward bevel angle while wing with 6.7% and 10% had 15° , 30° , 45° and 60° windward and leeward bevel angles. Results indicated that thinner delta wing showed a superior performance than thicker delta wings considering the value for CL/CD .

Gülsəçan [7] conducted wind tunnel experiments on delta wings with 35° sweep angle, 0.105m chord length, 0.3m wing span, 45° bevel angle on the windward side and having thickness-to-chord ratios of 0.0475, 0.095, 0.1425 and 0.1900. Wings are experimented upon $RE = 10000$ & 35000 with angles of attack from 4° to 10° .

Results revealed that as t/c increases, volume of the separated shear layer increases and flow structure moves to the centerline of the wing. At 6° angle of attack, while thicker wings experiences three-dimensional separation, thinnest wing has dual vortex structure. Also, it is found out that varying t/c under constant angle of attack produced nearly identical pressure distributions on axial station with varying the angle of attack at constant thickness to chord ratio. Moreover, Ghazijahani [43] improved upon the study by adding more t/c ratios of 2, 3.3, 5, 10 and 15% and a force balance system to gather the aerodynamic forces. Experiments were conducted at $RE = 15000, 35000 \& 100000$, angles of attack ranging from 0° to 30° on delta wings with 45° sweep angle, a root chord of 0.150m, wing span of 0.3m. Results indicate that t/c has significant influence on the formation of the leading-edge vorticities and their breakdown location. It is seen that, at low angles of attack, swirling strength of the vortical structures become stronger as t/c increases. However, as angle of attack increases, thicker wings are more prone to experience early vortex breakdown and 3-D flow separation. $-C_p$ distributions in Figure 2.18 shows that while thicker wings prevail at suction peak values at 6° , increased t/c deteriorated the beneficial contributions of the vortical structures at 16° .

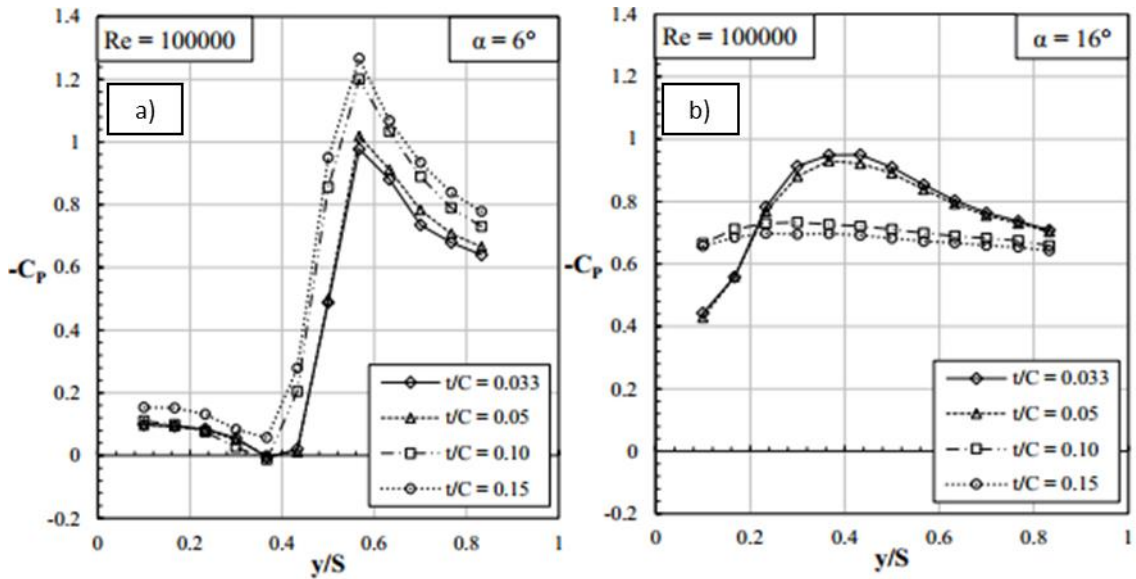


Figure 2.18. Pressure coefficient distribution at axial station at $x/c = 0.5$ [43]

Additionally, parallel to the results in pressure distribution, force measurements revealed that at relatively low angles of attack, lift coefficient, CL values gets higher when thickness-to-chord ratio is increased. However, when angle of attack is increased, it is seen in Figure 2.19 that thicker wings experience stall much earlier than the thin wings and CL values gets higher for low t/c values.

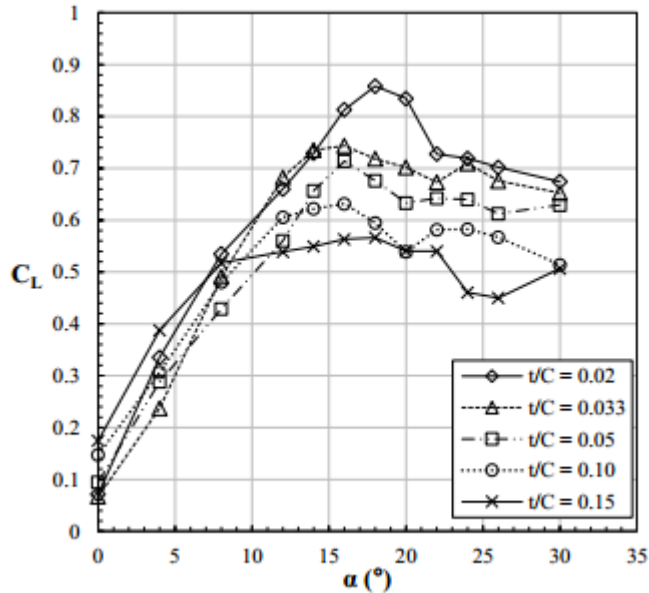


Figure 2.19. Lift coefficient CL with respect to angle of attack for varying t/c at RE = 35000 [43]

Kawazoe et al [44] investigated the effects of thickness-to-chord ratio by conducting experiments on thick and round leading-edge delta wings with the thin and small round one. Wings had 45° sweep angle with a root chord of 0.22m and 0.44m wing span. Thickness of the wings was t/c of 9.1% and 2.7%. Flow Reynolds number was fixed at 2.2×10^5 as the reference length was taken as the root chord. Figure 2.20 shows the aerodynamic coefficients taken with the force balance system for the thick and thin wings as a function of angle of attack.

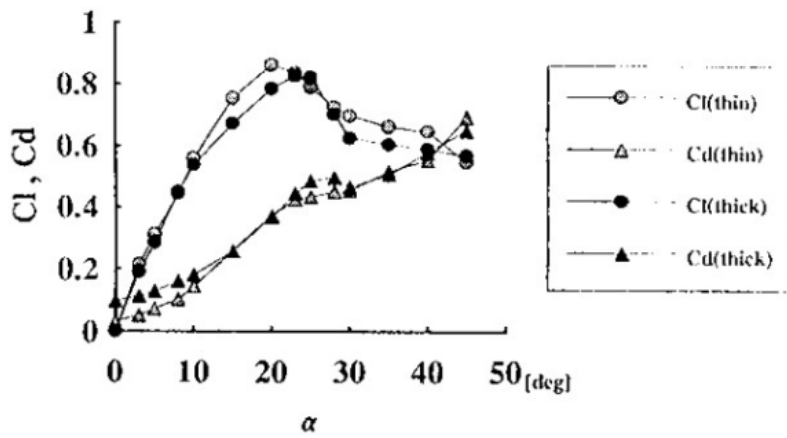


Figure 2.20. Lift and drag coefficients, Cl and Cd [44]

As the thickness increase, drag coefficient of the wing is slightly increased for the thicker wing. When lift coefficients are examined, it is hard to distinguish the difference for low angles of attack. On the other hand, thinner wing shows increased performance by approximately 10%, while the stall angle of attack is better when the thickness-to-chord ratio is increased. Figure 2.21 shows the relation between L/D ratio as the function of angle of attack.

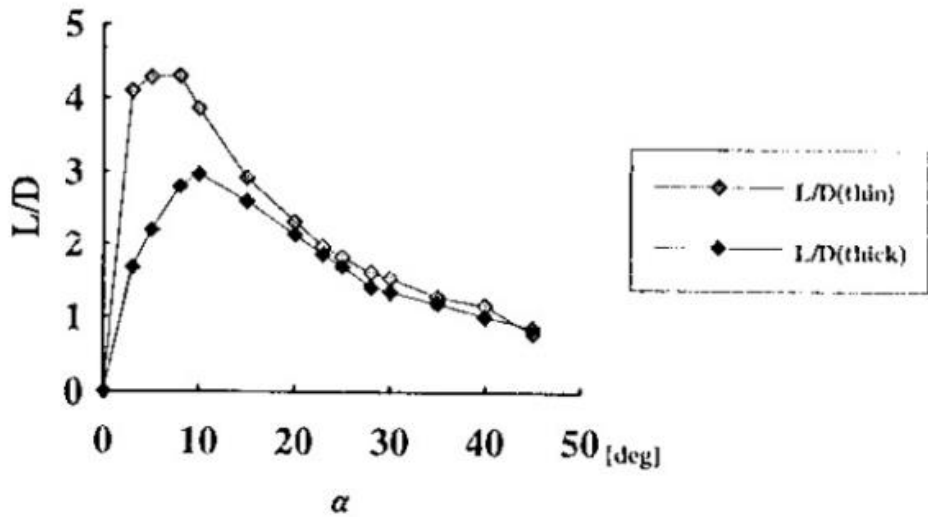


Figure 2.21. Lift-drag ratio with varying angle of attack [44]

As thickness-to-chord ratio increase L/D value tends to deteriorate for the thicker wing. Kawazoe et al. assesses the difference in the performance by the variance in the LEV size. For thin delta wing vortical structure size forms to be wider than the thick one. For that reason, leading-edge vorticities collide much sooner for thin wing. This fact causes the stall angle of attack to be lower for the thin delta wing when it is compared to the thicker one.

Saltzman et al. [45] investigated the thickness effect by comparing two aircraft wings with same sweep angle of 60° . XF-92A had a t/c of 6.5% and YF-102 had 4%. Figure 2.22 depicts the change in the drag coefficient, CD as a function of flight Mach number. Flight test data shows that the drag values for the wing YF-102 configuration is 3% higher and wave drag increment is 33% lower than the value of the wing XF-92A.

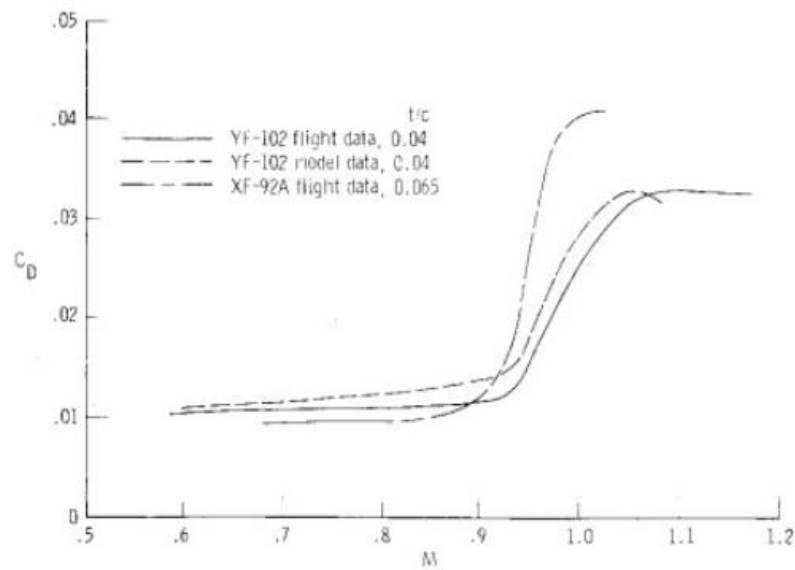


Figure 2.22. Effect of thickness-to-chord ratio on drag coefficient with varying Mach number [45]

2.4. Numerical Studies

Numerical methods such as computational fluid dynamics (CFD) or potential flow theory are powerful tools to estimate the flow domain and aerodynamic characteristics of many wing planforms. Although it is very challenging still to accurately estimate the true nature of vortical structures, studies has shown that a reliable level of confidence has been achieved to use such tools for calculating the flow domain on various problems and several research and effort has been put into use for developing algorithms and modifying the existent models to increase the computational accuracy to get the desired problem solution. For those reasons, delta wing flows lays an essential foundation in endeavor to further increase the accuracy of prediction models and to gain a deeper insight of vortical structures.

Zhang and Deng [16] investigated improvement in the capturing the surface pressure distribution and vortex structure of a 65° swept delta wing utilizing the hybrid scheme against the Roe's standard numerical scheme with detached eddy simulation (DES) for subsonic speed of Reynolds number 6×10^6 with a Mach number of 0.4. Figure 2.23 reveals the results of both experimental data and numerical study at hand. Pressure distribution on two axial stations show that using the hybrid solver scheme made great improvements in capturing the pressure distribution when compared to the Roe's standard scheme.

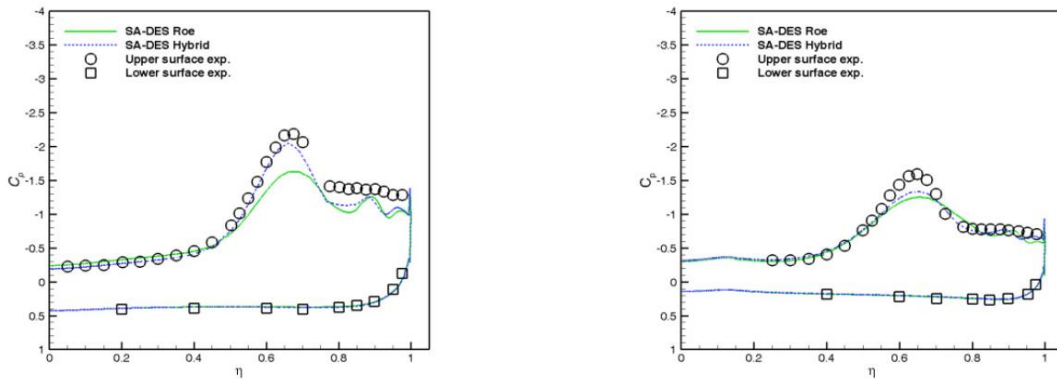


Figure 2.23. Comparison of surface pressures and experimental data (a) $x/c = 0.5$, (b) $x/c = 0.8$ [16]

Another numerical study by Mitchell et al. [46] utilized DES for data verification purpose of a ONERA wind tunnel experiment. A delta wing with 70° sweep angle, 0.95m root chord, 0.69m wing span with a 0.02m thickness is analyzed using CFD at a Reynolds number of 1.56×10^6 . A grid independence study was conducted and densest mesh revealed consistent results with wind tunnel experiment. Figure 2.24 shows a detailed result for isosurface and contour for non-dimensional axial vorticity.

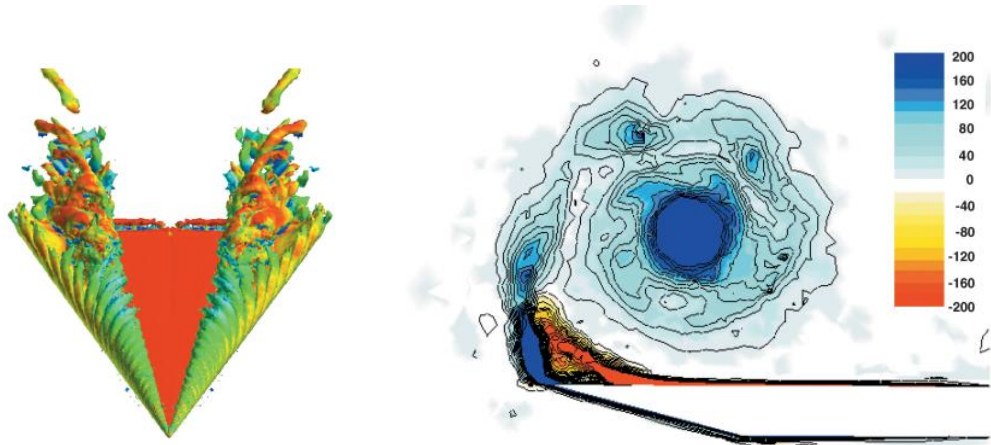


Figure 2.24. Isosurface of non-dimensional axial vorticity & non-dimensional axial vorticity contour at $x/c = 0.53$ [46]

A computational study conducted by Görtz [47] investigated the accuracy of DES (Detached Eddy Simulation) model and presented the results from a previous experimental study. Results yielded that in order to successfully capture the unsteady vortical structure required time step should be 10^{-4} seconds and proved that it is possible to use DES model with a dense structured grid to achieve high levels of accuracy in the simulation model.

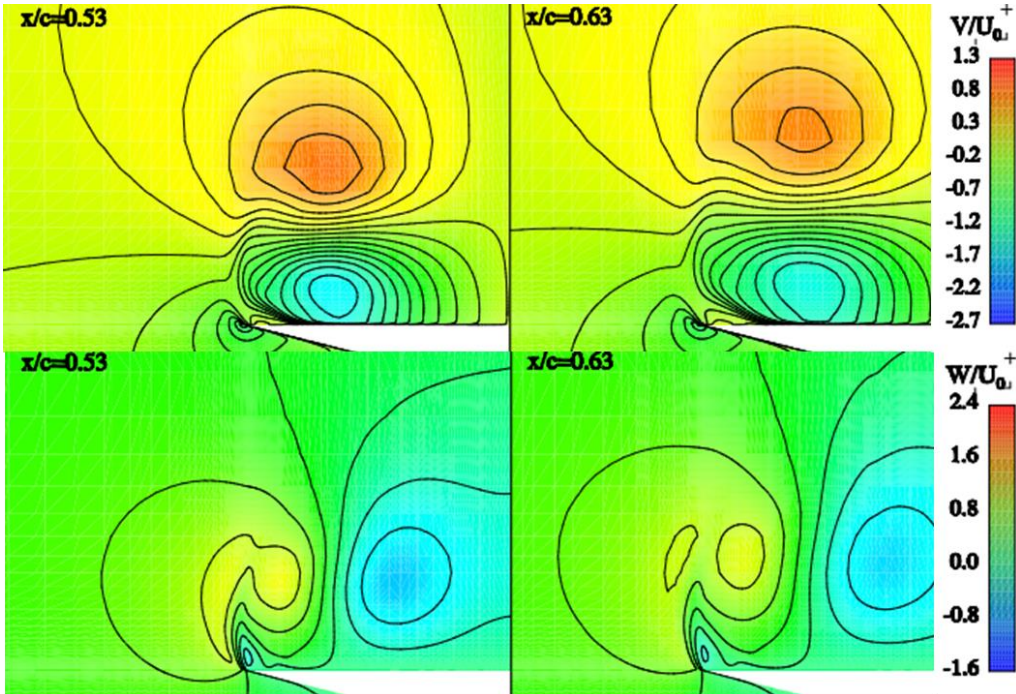


Figure 2.25. Numerical (left) and experimental (right) axial and transversal velocity contours [47]

Roy et al. [48] investigated the accuracy of numerical models on a 70° swept ONERA wing using unsteady model DES with SA in elsA and steady models of SARC and SST at FLU3M software. A structured grid with a refinement region at the vortex dominant zone is created to analyze under a Mach number of 0.2 and angle of attack of 27° . Figure 2.26 shows the pressure coefficient distribution at $x/c = 0.63$ and results indicate that SARC model demonstrated a little more success when it is compared to the SST model. Moreover, since SA model is not well adapted for the cases with transition using it with DES computational failed to yield superior results to the steady computation.

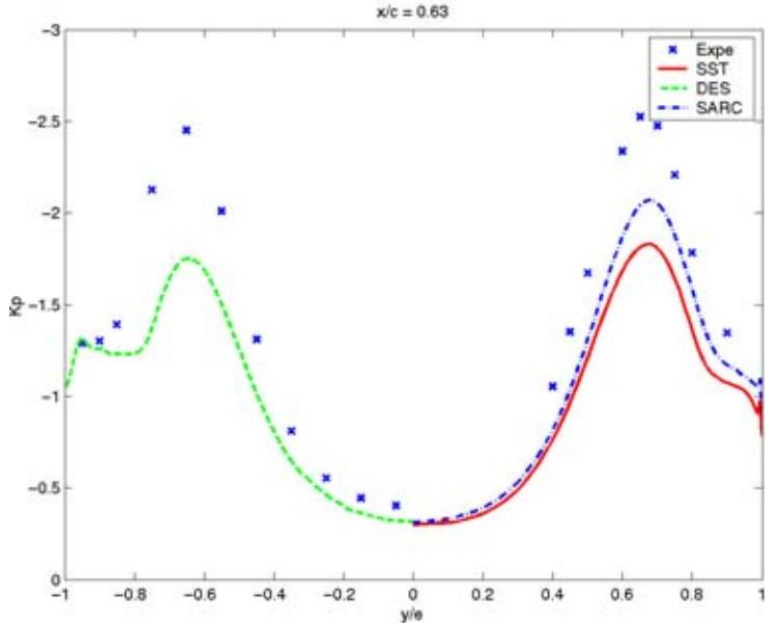


Figure 2.26. Cp distribution extracted from unsteady (DES) and steady (SARC&SST) computations along with experimental data [48]

Jirasek and Peng [49] conducted a verification study on the VFE-2 delta wing at low-speed subsonic Mach number of 0.14 at angle of attack of 23° . Numerical simulations consisted of SA, EARSM as RANS models and HYB0 as RANS-LES hybrid model. Figure 2.27 shows the streamline patterns for the axial cut plane $x/c = 0.4$ and pressure coefficient distributions on the leeward surface. Results are stated such that in predicting the strength of the vortical structures and their positions on the wing surface HYB0 model has superior performance to other models. Moreover, between steady models, EARSM was found to be the least accurate of all.

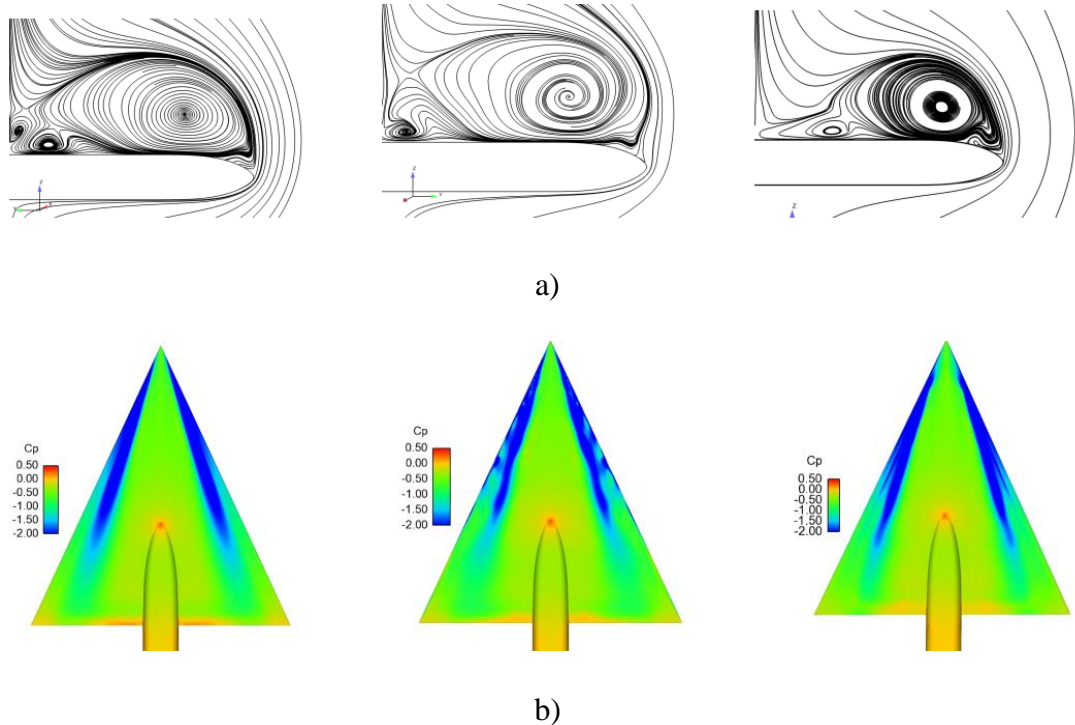


Figure 2.27. Results for numerical models, SA (left), EARSM (middle), HBY0 (right) a) Streamlines at $x/c = 0.4$, b) Surface pressure coefficient distributions [49]

Cai et al. [50] has investigated the effects of the leading-edge vortex flaps utilized on a 50° sweep delta wing at $RE = 200000$ and $\alpha = 30^\circ$. Computations were conducted with a recently developed BXCFD solver, AUSMPW+ scheme were chosen utilizing Reynolds-stress-constrained RANS/LES hybrid method. Results indicate that a 70° of flap angle has been found to delay the vortex breakdown. Figure 2.28 shows the vorticity contours at $x/c = 0.3$ station.

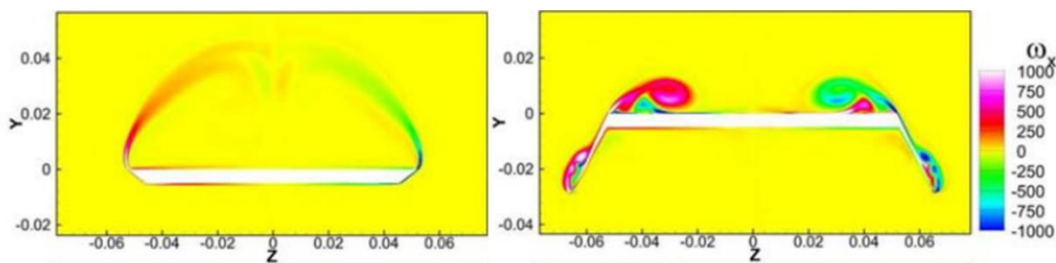


Figure 2.28. Vorticity contours at axial station $x/c = 0.3$ with a flap angle of 70° on the leading edge [50]

Küçükyılmaz [34] studied the flow control by along-the-core-blowing method numerically. Delta wing had exactly the same geometry in the experimental study of Mitchell [51]. Analysis was focused on an angle of attack of 27° and with a Reynolds number of 1.56×10^6 . A mesh independency study is conducted and control method is applied to the base wing. Not only the results show that the method at hand resulted in desired outcome, that is to delay the vortex breakdown, but also turbulence model independency study in the thesis showed that numerically, among steady turbulence models, SST k-w model with Curvature Correction (CC) extension provided the most accurate results regarding the capturature of vortical structures. Table 2.1 shows the axial location of the vortex breakdown captured with different turbulence models.

Table 2.1. Vortex Breakdown Location of Turbulence Models [34]

#	Turbulence Model	Model Extension	LEV Breakdown Location (x/c)
1	k- ω	Low-Re Corrections (LRC) Shear Flow Corrections Curvature Correction (CC)	No detection
2	k- ω SST	-	0.83
3	k- ω SST	LRC	0.79
4	k- ω SST	CC	0.66
5	k- ω SST	LRC CC	0.66
6	Spalart-Allmaras	-	No detection
7	Spalart-Allmaras	CC	0.60

Onkar et al. [52] studied the aeroelastic properties of a cropped delta wing. Both RANS with SST k-w turbulence model and non-linear finite element solvers were

coupled to predict the aeroelastic behavior of the delta wing under a range of dynamic pressures. Yakinthos et al. [53] studied the trailing-edge blowing method on a delta wing in the study of Shih and Ding [54]. CFD analysis is conducted with a pressure based steady solve with SST k-w turbulence model. Results in the Figure 2.29 shows that the trailing-edge jet blowing delayed the vortex breakdown phenomena.

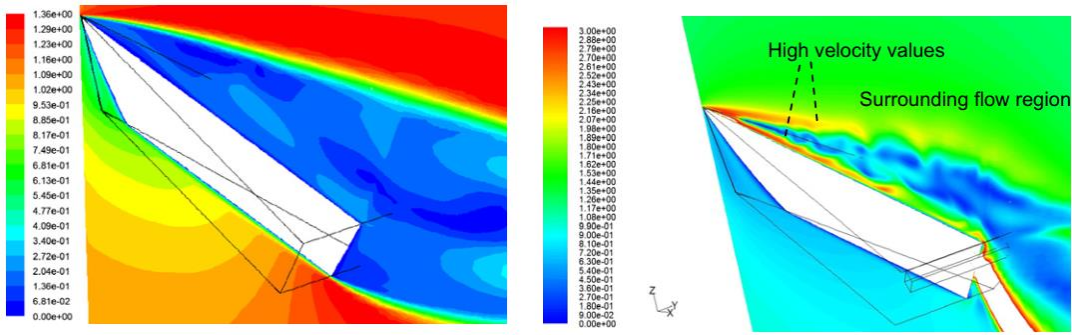


Figure 2.29. Axial velocity contour passing through vortex line with base wing (left) and trailing-edge jet flap (right) [53]

Morton et al. [55] applied periodic suction and blowing from the leading edge. Results indicate that the method delayed the vortex breakdown to a station located 25% of chord length downstream and increased the normal force on the wing by 27%. Sharma et al. [56] investigated a compound delta wing numerically under Mach numbers from 0.3 to 2.0 and results showed that with the change of flight Mach number, flow properties undergo a sudden change and flow near the upper surface of the wing below the leading-edge vorticities can become supersonic and shockwaves are seen while Mach number is 0.85. Allan et al. [57] numerically investigated the wind tunnel wall influences and concluded that dimensions of the wind tunnel may cause sever effects on the performance of pitching delta wings. Sharma et al. [58] investigated outcome of the geometric modifications by analyzing a compound delta wing. Irani et al. [59] conducted both experimental and numerical analysis on the aeroelastic properties and results indicate that both thickness of the wing and store loading has significant importance in the flutter speed.

Delta wings are also used in the supersonic combustion engines technology rather knowns as scramjets as mixing enhancers. Huang et al. [60] conducted computational simulations about the fuel mixing procedures utilizing the vortical flows generated by delta wings. Also, Luedeke [64] conducted a performance comparison between DES97 and DDES (Delayed DES) models using for FA-5 fighter aircraft and found out that DDES model provided a better resolution for unsteady effects. Figure 2.30 shows the normalized velocity components of the experimental and numerical study.

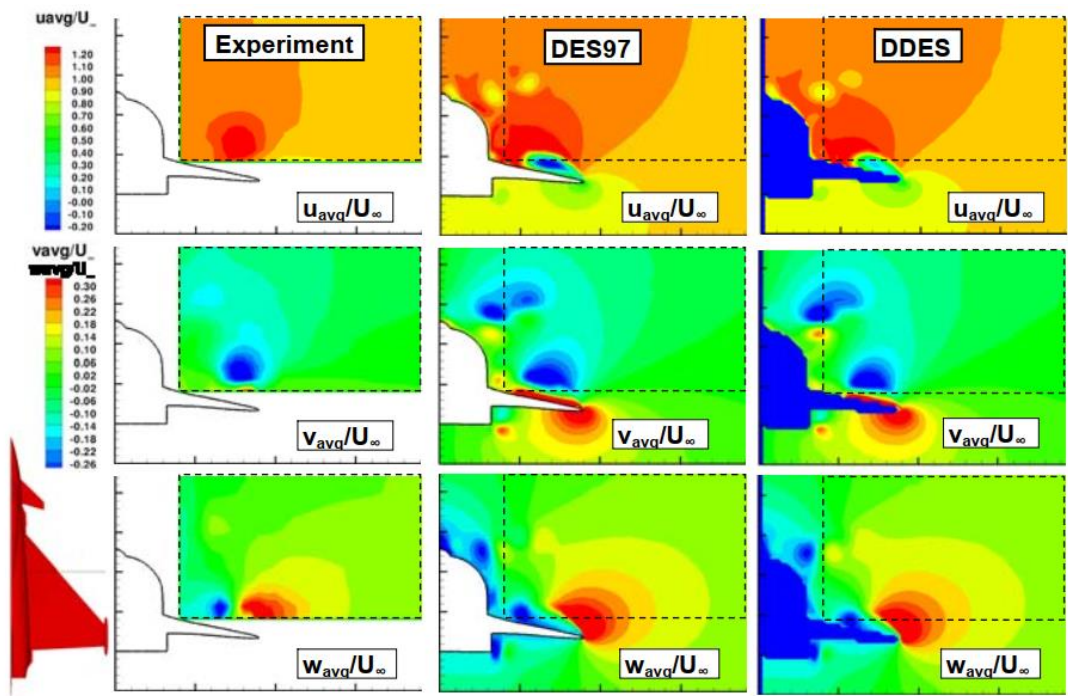


Figure 2.30. Comparison of normalized velocity components at $x/c = 0.4$ [61]

To sum up, although extensive numerical and experimental studies have been done, some aspects of delta wing flows are still a matter of controversy which is derived from the fact that the nature of the vortical flows are determined by many parameters in interaction, such as pressure waves, boundary layer detachment, unsteadiness, shearing instabilities.

CHAPTER 3

SIMULATION MODEL AND VALIDATION STUDY

This chapter includes the detailed information about the modelling strategy. Wing geometry, properties of the flow domain and solution parameters are explained. Simulation domain is created by ANSYS SpaceClaim. The unstructured grid is generated by using ANSYS Mesher and transferred to ANSYS Fluent solver to run the steady state RANS simulations. After achieving mesh independency, computational method is verified by the results of the experimental study [7].

3.1. Flow Domain, Boundary Conditions

The dimensions of the delta wing models are identical to those of the experimental thesis study of Gülsançan [7] and have a sweep angle of 35° , root chord (c) of 0.105m, wing span of 0.3m and $t/c = 0.0475 \& 0.1900$. The thickness-to-chord ratios of the wings modelled in the numerical study are $t/c = 0.019, 0.047, 0.1142, 0.1900$ and wings are beveled on the windward side with a cut angle of 45° to create sharp leading-edges. Sting and horizontal supports used in the experimental study is excluded from the numerical model as shown in the Figure 3.1. The extends of the half spherical flow domain, large enough for downstream to reach free stream properties before far field [62, 63], is given in terms of root chord in the Table 3.1.

Table 3.1. Dimensions of the flow domain in the simulations in terms of root chord

Flow Domain	Dimension (RC)
Up from Wing Apex	41
Down from Wing Apex	41
Upstream from Apex	40
Downstream from Apex	42
Span wise From Wing Centerline	41

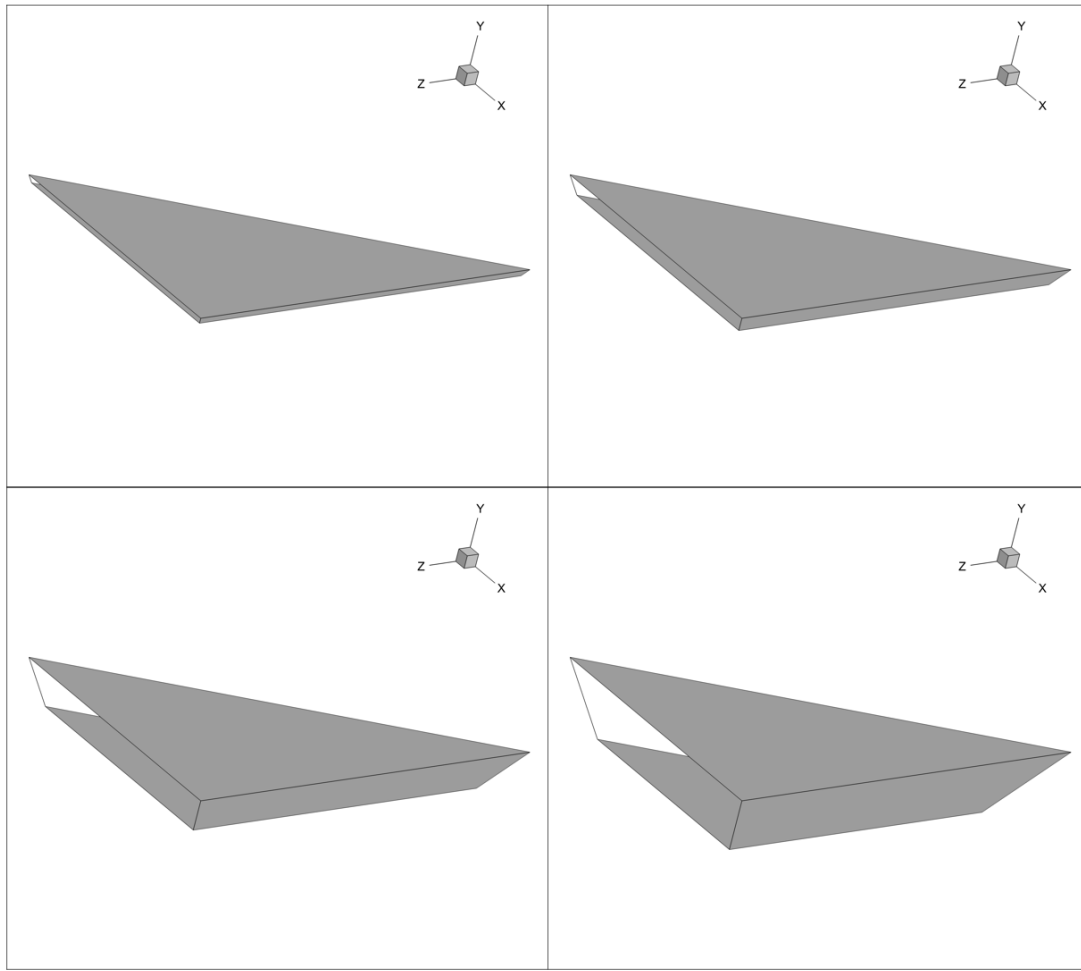


Figure 3.1. Wing models with $t/c = 0.019, 0.047, 0.1142, 0.1900$

Simulations involve various flight conditions between an angle of attack range from 4° to 40° , at two Reynolds numbers of 3.5×10^4 and 3×10^5 for delta wings with four different thickness-to-chord ratios as mentioned earlier. Since the corresponding Mach numbers are 0.014 and 0.125 which are lesser than 0.3, flow is assumed to be incompressible. Far field of the flow domain is applied with a velocity inlet boundary condition having free stream flow properties [64, 65]. Due to the symmetricity in flow field, symmetry boundary condition is applied at the plane passing through both flow domain and delta wing centerline and delta wing walls are defined to have a no slip wall boundary condition. Details of the boundary conditions are represented in the Figure 3.2 and Table 3.2.

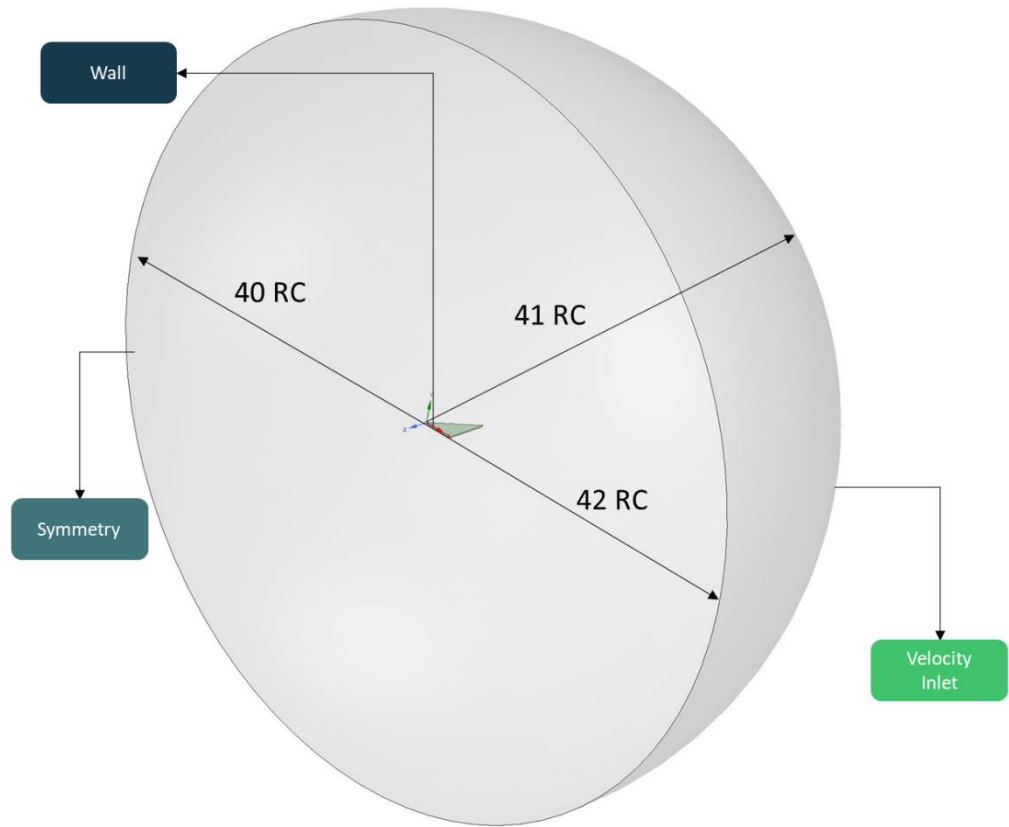


Figure 3.2. Representation of the flow field and boundary conditions

Table 3.2. Details of the boundary conditions

Surface Name	Boundary Type	Parameter	Value
Inlet	Velocity Inlet	Velocity (m/s)	4.97, 42.58
		Turbulent Intensity (%)	0.1
Wall	Wall	No Slip	-
Symmetry Plane	Symmetry	-	-

3.2. Grid Generation

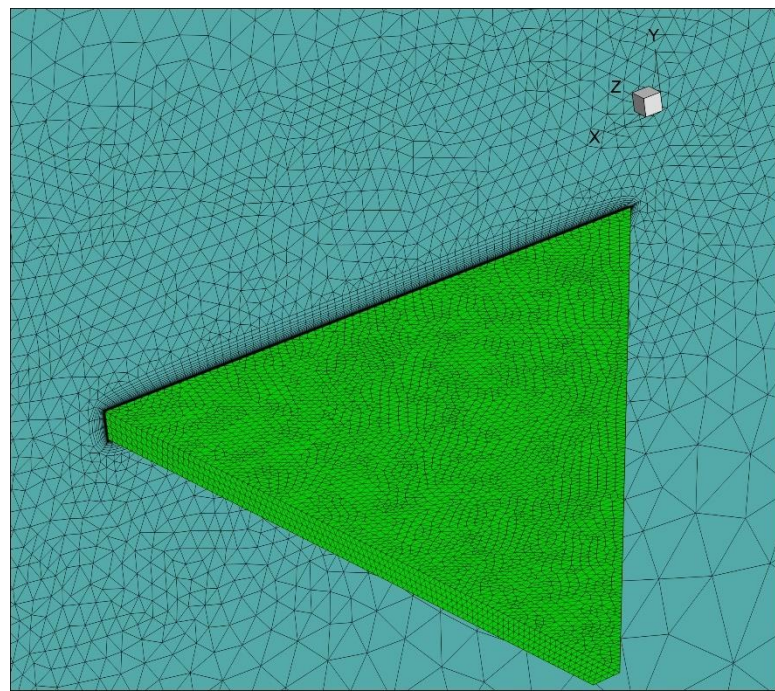
3D unstructured grids, consisting of prism cells at the boundary layer and tetrahedron cells populating the rest of the flow domain, are prepared. The number of the elements in the grids are controlled by the surface element sizing and also near body volume sizing options. Regarding the boundary layer modelling, first layer thickness of the prism cells is calculated to be $3.5 \times 10^{-6} m$ in order to ensure a y^+ value to be kept below 1 for all simulations. Detailed mesh sizing information is given in Table 3.3. Also resultant mesh quality metrics are provided in Table 3.4 Six cases having approximately 1, 3, 6, 11, 16 and 21 million elements are examined in the mesh independence study. A isometric and sectional view of the grids are given in the Figure 3.3 and Figure 3.4 respectively.

Table 3.3. *Mesh information*

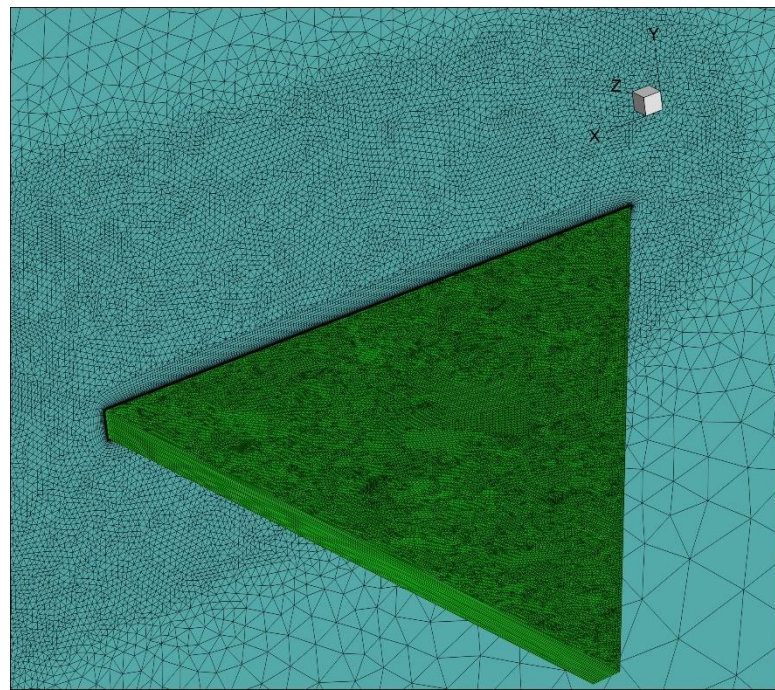
# of the Grid	Mesh 1	Mesh 2	Mesh 3	Mesh 4	Mesh 5	Mesh 6
Element Sizes (m)						
Leading Edge	6.7E-03	3.3E-03	1.7E-03	1.3E-03	1.0E-03	8.3E-04
Trailing Edge	6.7E-03	3.3E-03	1.7E-03	1.2E-03	1.0E-03	8.3E-04
Leeward Surface	1.6E-02	8.0E-03	4.0E-03	2.0E-03	1.0E-03	5.0E-04
Windward Surface	1.6E-02	8.0E-03	4.0E-03	2.0E-03	1.0E-03	5.0E-04
Body of Influence	2.0E-02	1.0E-02	5.0E-03	3.0E-03	1.5E-03	1.0E-03
Overall Domain Mesh Sizes						
Number of Volume Elements	1024132	3096530	6325478	11548632	16386122	21356987

Table 3.4. *Mesh quality metrics*

# of the Grid	Mesh 1	Mesh 2	Mesh 3	Mesh 4	Mesh 5	Mesh 6
Max. Skewness	0.989	0.985	0.982	0.980	0.968	0.952
Average Skewness	0.312	0.283	0.279	0.238	0.218	0.208
Max. Aspect Ratio	2357.99	2042.93	1770.52	1405.90	983.60	861.09
Average Aspect Ratio	133.61	106.93	92.76	40.27	15.92	11.89

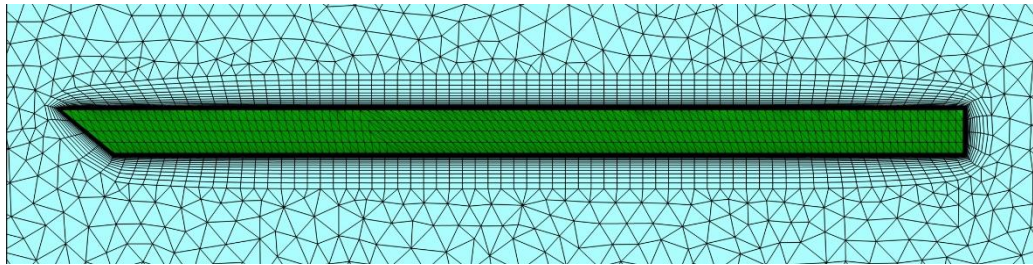


a)

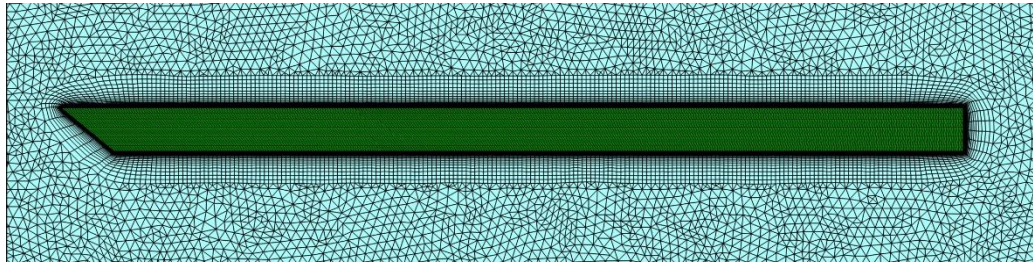


b)

Figure 3.3. Surface and body of influence meshes: a) Mesh 4, b) Mesh 6



a)



b)

Figure 3.4. Near wing symmetry plane meshes: a) Mesh 4, b) Mesh 6

3.3. Solver Parameters

A SIMPLE solver scheme is chosen for the pressure-velocity coupling, Green-Gauss Node Based scheme is chosen for the gradient, A second order scheme is chosen for pressure spatial discretization. A second order upwind scheme is chosen for accuracy of momentum, turbulent kinetic energy and specific dissipation rates. The under-relaxation factors for the solver scheme is given in the Table 3.5.

Table 3.5. *Under-Relaxation factors*

Under-Relaxation Factors	Value
Pressure	0.3
Density	0.8
Body Forces	0.8
Momentum	0.7
Turbulent Kinetic Energy	0.8
Specific Dissipation Rate	0.8
Turbulent Viscosity	0.8

Regarding the choice of turbulence model, there are several turbulence models to choose from and each of them has a tradeoff concerning accuracy, depending on the case at hand, and computational resource. Numerical delta wing studies of Küçükylmaz [34], Onkar et al [52], Yakinthos et al. [53], Ding et al. [54], Sayılır [66] has proved that simulation of two-equation eddy viscosity model SST k- ω , with Curvature Correction (CC) extension is very successful in terms of the accuracy in capturing the vortical structures. As a result, SST k- ω turbulence model with mention extension is chosen for modelling the vortical flow for all cases. The theory behind the RANS based turbulence modelling with the mathematical definitions are explain in the following sections.

3.3.1. Reynolds Averaging and Boussinesq Approximation

Reynolds averaging of the equation set consisting mass and momentum equations are the baseline for all the algorithms capable of performing computational fluid dynamics analysis. This averaging involves the solution parameters in the Navier-Stokes equations to be pulled apart in mean (time-averaged) and fluctuating components.

According to RANS averaging, velocity components are decomposed as,

$$u_i = \bar{u}_i + u'_i \quad (3.1)$$

Where \bar{u}_i and u'_i are the mean and the fluctuating components respectively.

Similarly, pressure, energy or species concentration are expressed in same fashion:

$$\varphi = \bar{\varphi} + \varphi' \quad (3.2)$$

To obtained the Reynolds Averaged Navier-Stokes (RANS) equations, relations 3.1 and 3.2 are substituted in the differential form of conservation of mass and momentum equations. Taking the time average of the modified relation becomes the RANS equation in the tensor form:

$$\frac{\partial \rho}{\partial t} + \frac{\partial(\rho \bar{u}_i)}{\partial x_i} \quad (3.3)$$

$$\begin{aligned} \frac{\partial(\rho\bar{u}_i)}{\partial t} + \frac{\partial(\rho\bar{u}_i\bar{u}_j)}{\partial x_j} = & -\frac{\partial\bar{p}}{\partial x_i} + \frac{\partial}{\partial x_j} \left[\mu \left(\frac{\partial\bar{u}_i}{\partial x_j} + \frac{\partial\bar{u}_j}{\partial x_i} - \frac{2}{3} \delta_{ij} \frac{\partial\bar{u}_k}{\partial x_k} \right) \right] \\ & + \frac{\partial(-\rho\bar{u}'_i\bar{u}'_j)}{\partial x_j} \end{aligned} \quad (3.4)$$

Where \bar{p} is time-averaged pressure, t is time and ρ is density, μ is dynamic viscosity and δ_{ij} is Kronecker delta. The last term at the numerator in the momentum equation represents the effects of the turbulence. It is called the Reynolds stress tensor. To model this term Boussinesq hypothesis is used to relate the stresses to the rate of strain of averaged velocity. The relation is defined as:

$$-\rho\bar{u}'_i\bar{u}'_j = \mu_t \left(\frac{\partial\bar{u}_i}{\partial x_j} + \frac{\partial\bar{u}_j}{\partial x_i} \right) - \frac{2}{3} \delta_{ij} \left(\rho k + \frac{\partial\bar{u}_k}{\partial x_k} \right) \quad (3.5)$$

The term k is the turbulent kinetic energy and μ_t is the turbulent viscosity, also named eddy viscosity. In SST $k-\omega$ model two additional transport equation is solved. One equation for turbulent kinetic energy, k and the other one for the specific dissipation rate, ω .

3.3.2. Shear-Stress Transport (SST) $k-\omega$ Turbulence Model

Developed by Menter [67] in 1994, SST $k-\omega$ model successfully combined the two-equation eddy viscosity models, $k-\omega$ and $k-\varepsilon$, using the Boussinesq approximation. Mentioned two models has their strong sides, as such $k-\omega$ model is beneficial in the near wall region and $k-\varepsilon$ model is used for the rest of the flow domain. Hence, $k-\varepsilon$ model is modified to become a composite turbulence model using the strong near wall modelling quality of $k-\omega$.

In order to utilize both of the models in SST $k-\omega$, a blending function is multiplied with both of the component models and added together. In the near wall region, the blending function takes the value of one which puts into use of $k-\omega$ model. On the other hand, when computation takes place away from any wall boundary, blending

function then becomes 0, which activates the k- ϵ model. Moreover, the modification of the turbulent viscosity to account for the transport of the turbulent shear stress. Also, SST k- ω model harbors a damped cross-diffusion derivative term in the calculation of ω , whose modelling constants are different from the standard k- ω model. Briefly, it can be said that all the mention specifications of the SST k- ω makes it much more reliable and accurate than standard k- ω model for challenging cases such as treating the boundary layer, capturature of shocks, adverse pressure gradients, even conjugated heat transfer problems.

Mathematical definitions of SST k- ω model are given as:

$$\frac{\partial(\rho k)}{\partial t} + \frac{\partial(\rho k u_i)}{\partial x_i} = \frac{\partial}{\partial x_j} \left(\Gamma_k \frac{\partial k}{\partial x_j} \right) + \widetilde{G}_k - Y_k + S_k \quad (3.6)$$

$$\frac{\partial(\rho \omega)}{\partial t} + \frac{\partial(\rho \omega u_j)}{\partial x_j} = \frac{\partial}{\partial x_j} \left(\Gamma_\omega \frac{\partial \omega}{\partial x_j} \right) + G_\omega - Y_\omega + S_\omega + D_\omega \quad (3.7)$$

Where,

\widetilde{G}_k : Production of turbulent kinetic energy due to mean velocity gradients

G_ω : Production of ω

Y_k, Y_ω : Dissipation of k and ω due to turbulence

Γ_k, Γ_ω : Effective Diffusivity of k and ω

S : User defined source terms

D_ω : Cross diffusion term

The effective diffusivities are given as:

$$\Gamma_k = \mu + \frac{\mu_t}{\sigma_k} \quad (3.8)$$

$$\Gamma_\omega = \mu + \frac{\mu_t}{\sigma_\omega} \quad (3.9)$$

σ_k and σ_ω signifies the Prandtl numbers for k and ω in those equations. The turbulent viscosity relation is given as:

$$\mu_t = \frac{\rho k}{\omega} \frac{1}{\max\left[\frac{1}{\alpha^*}, \frac{SF_2}{a_1 \omega}\right]} \quad (3.10)$$

$$\sigma_k = \frac{1}{\frac{F_1}{\sigma_{k,1}} + \frac{1-F_1}{\sigma_{k,2}}} \quad (3.11)$$

$$\sigma_\omega = \frac{1}{\frac{F_1}{\sigma_{\omega,1}} + \frac{1-F_1}{\sigma_{\omega,2}}} \quad (3.12)$$

In the turbulent viscosity relation (Eqn. 3.10), S indicates the magnitude of the strain rate. Other terms in the equation set, $a_1, \sigma_{k,1}, \sigma_{k,2}, \sigma_{\omega,1}, \sigma_{\omega,2}$ are model constants given as 0.31, 1.176, 1.0, 2.0 and 1.168 respectively. α^* is the turbulent viscosity damping coefficient constituting a low-Reynolds correction given as:

$$\alpha^* = \alpha_\infty^* \left(\frac{\alpha_0^* + \frac{Re_t}{R_k}}{1 + \frac{Re_t}{R_k}} \right) \quad (3.13)$$

$$Re_t = \frac{\rho k}{\mu \omega} \quad (3.14)$$

Where $R_k = 6, \alpha_0^* = 0.024$ and $\alpha_\infty^* = 1$, same constant values as in the standard $k-\omega$ model. In the case of high-Reynolds number constants become $\alpha^* = \alpha_\infty^* = 1$. The blending functions F_1 and F_2 are defined as:

$$F_1 = \tanh(\phi_1^4) \quad (3.15)$$

$$\phi_1 = \min \left[\max \left(\frac{k^{0.5}}{0.09 \omega y}, \frac{500 \mu}{\rho y^2 \omega} \right), \frac{4 \rho k}{\sigma_{\omega,2} D_\omega^+ y^2} \right] \quad (3.16)$$

$$D_\omega^+ = \max \left[2 \rho \frac{1}{\sigma_{\omega,2}} \frac{1}{\omega} \frac{\partial k}{\partial x_j} \frac{\partial \omega}{\partial x_j}, 10^{-10} \right] \quad (3.17)$$

$$F_2 = \tanh(\phi_2^2) \quad (3.18)$$

$$\phi_2 = \max \left[2 \frac{k^{0.5}}{0.09\omega y}, \frac{500\mu}{\rho y^2 \omega} \right] \quad (3.16)$$

Where, D_ω^+ is the positive side of the cross-diffusion term and y corresponds to the distance to the surface. Having briefly explained the two-equation eddy-viscosity model SST $k-\omega$, it should be noted that the model at hand is insensitive to the effects of streamline curvature and flow rotation which becomes significant when solving a system with turbulent flows are involved. For that reason, Smirnov and Menter [68] came up with a modification for the SST $k-\omega$ model. Using the developed correction improves the performance of the model when vortical flow systems, such as in delta wing flows.

3.4. Grid Independence

Achieving mesh independency requires to resolve the flow field, especially vortical structures accurately in delta wing flows. To display the convergence of the results through computational grids, velocity magnitudes are tracked at eleven points near the surface. Pressure coefficient distributions at axial stations $x/c = 0.4$ & 0.6 are extracted from the surface and contours of negative C_p are gathered for comparison. Moreover, change in the aerodynamic coefficients, CL and CD are monitored.

As mentioned in the solver parameters section, a steady RANS based model along with SST $k-\omega$ with the curvature correction extension is used in ANSYS Fluent software. The model at hand demonstrated superior performance in solving the adverse pressure gradients and separated flows, and curvature correction is activated to resolve the effects of the streamline curvature as it was suggested by the literature [34, 66] as mentioned above.

A number of calculations has been made with different relaxations values and initializations and concluded with a set of relaxations and full multi grid (FMG) initialization to start the iterations with suitable initial values in the flow domain to

achieve the convergence. The convergence of the calculations was assessed with the distribution of the residual values throughout the iterations and average velocity magnitude values tracked by the points assigned at different locations on the flow field near delta wing. The scaled residual distributions for Mesh 5 are given in the Figure 3.5 and also the locations of eleven property tracking points randomly distributed near the walls of the delta wing are given in the Figure 3.6. Also, the Table 3.6 gives the exact locations of the tracking points above the leading-edge and leeward surfaces of the wing. It should be noted that the delta wing apex in the flow domain is located at the reference frame.

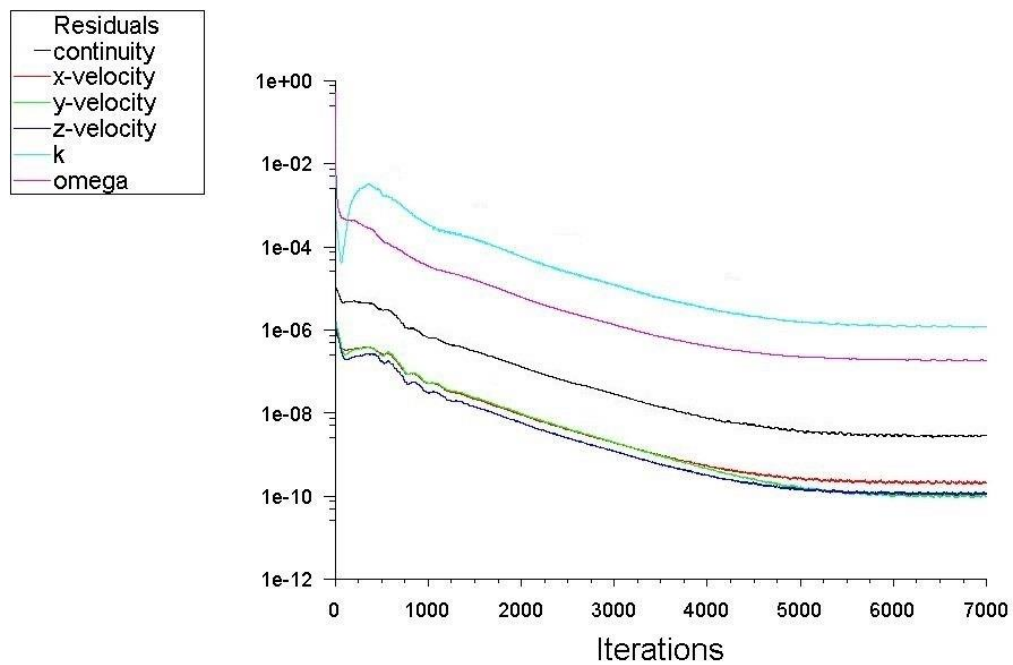


Figure 3.5. Scaled residual history of Mesh 5

Table 3.6. *Coordinates of the tracking points*

# of Points	X-Coordinate [m]	Y-Coordinate [m]	Z-Coordinate [m]
1	0.0250203	0.0010	-0.01283642
2	0.0471175	0.0010	-0.02491126
3	0.0606478	0.0010	-0.03666280
4	0.0818249	0.0010	-0.04322001
5	0.0944317	0.0010	-0.04766222
6	0.0373848	0.0010	-0.04825297
7	0.0662414	0.0010	-0.08505999
8	0.0904151	0.0010	-0.12003303
9	0.0119167	-0.0025	-0.01366439
10	0.0473770	-0.0025	-0.06432196
11	0.0872699	-0.0025	-0.12131173

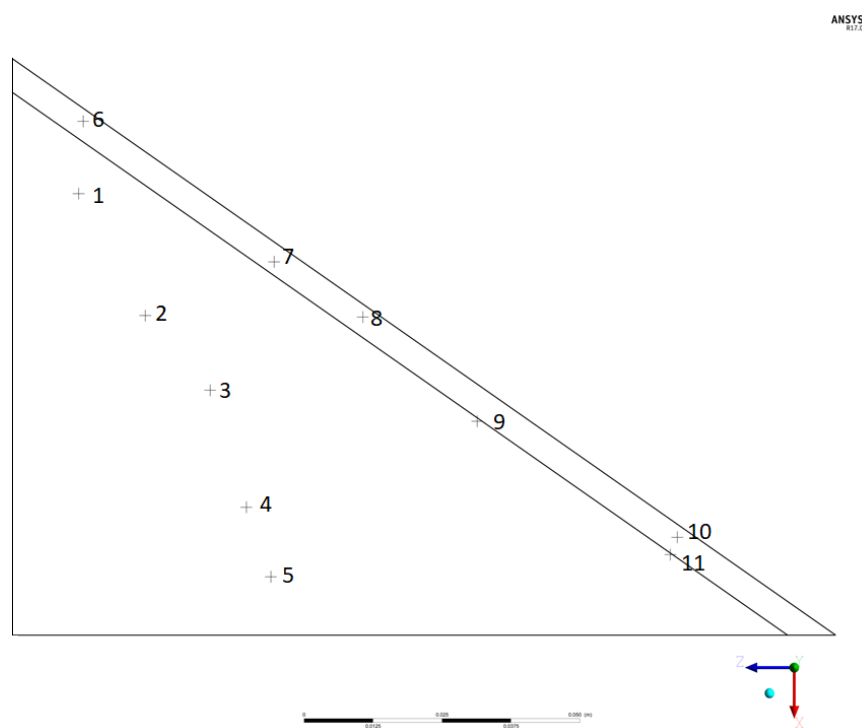
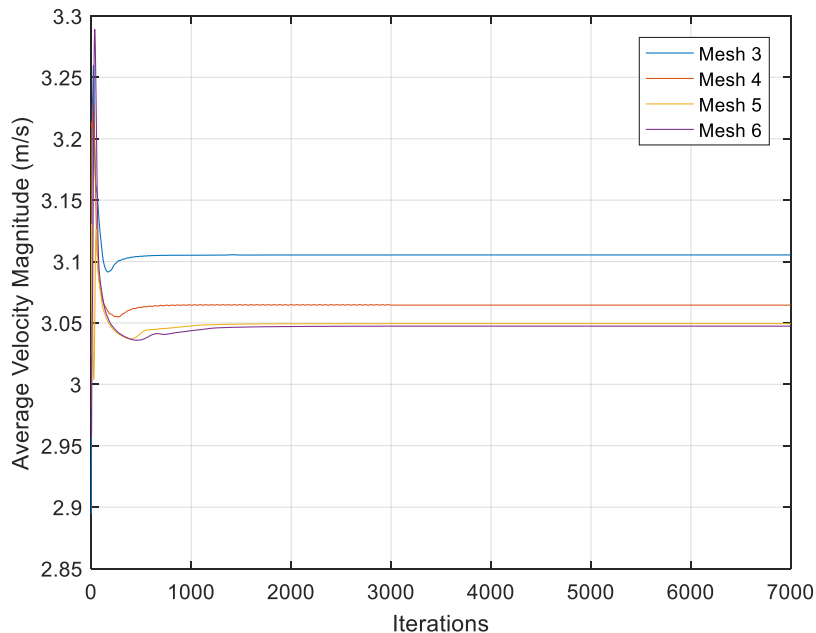


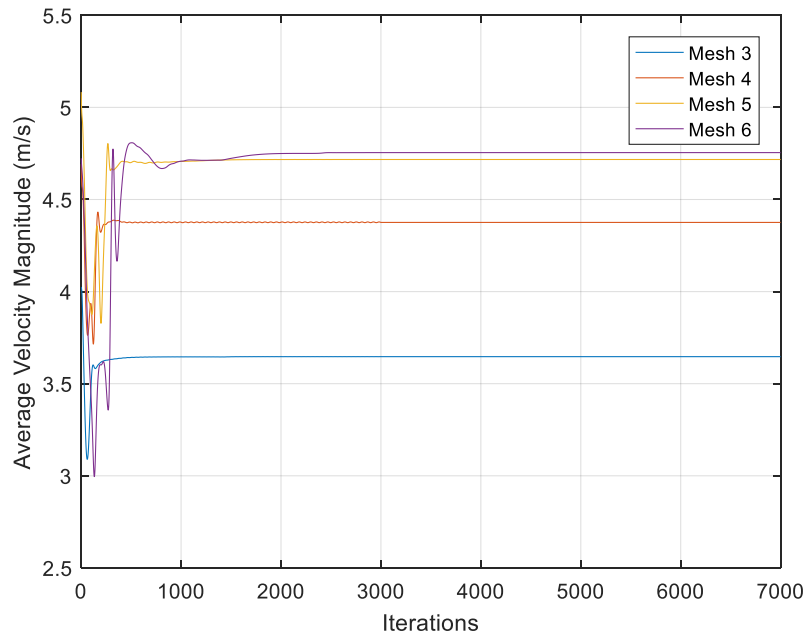
Figure 3.6. Monitor points distribution on leeward and leading-edge surfaces

In Figure 3.7, the history of the average velocity magnitude is given for the Point 2, Point 7 and Point 11. As it can be seen from the distributions that the difference between Mesh 5 and Mesh 6 are minimal. Also, the convergence with respect to the number of iterations are achieved.

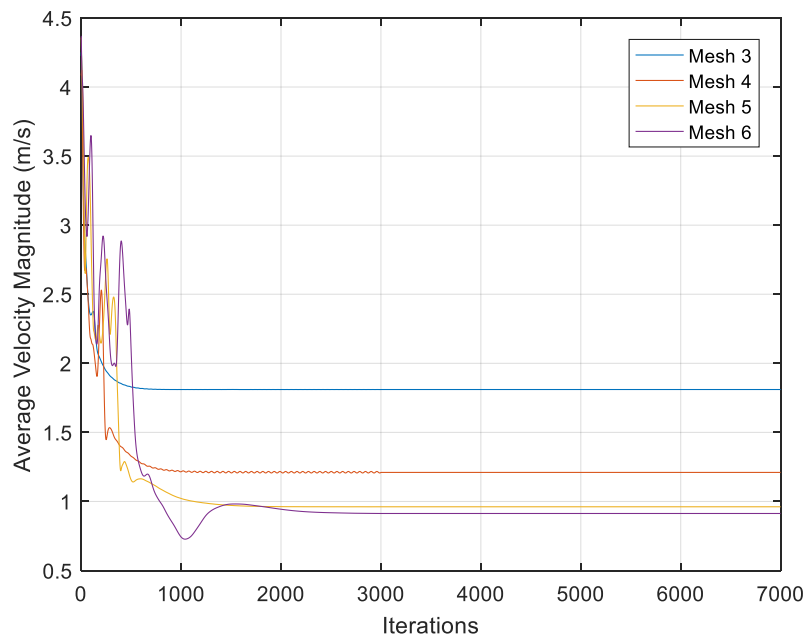
Moreover, as mentioned above SST k- ω turbulence model is chosen for the CFD analysis which requires the non-dimensional wall height, y^+ to be less than the value of 1. Figure 3.8 shows the y^+ distribution on the leeward surface of the wing for Mesh 5. As flow shearing increases y^+ values throughout the run becomes larger. Since most shearing occurs on the leeward surface, only the y^+ distribution of the top surface is given. However, during CFD analysis y^+ tracking is conducted for all wall surfaces and ensured that maximum value of y^+ for all surfaces is less than 1.



a)



b)



c)

Figure 3.7. Velocity magnitude though iterations a) Point 2 b) Point 7 c) Point 11

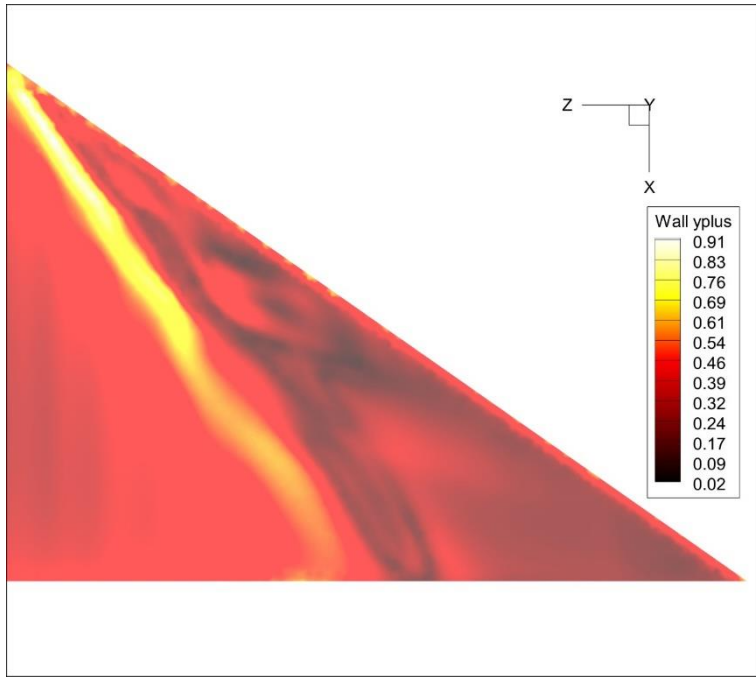


Figure 3.8. $y+$ contour of Mesh 5

The number of volume elements, especially in the body of influence region, is increased to get the optimum sizing parameters for the CFD analysis. Another important result presented to achieve the mesh independency is the variation of the pressure coefficient (C_p) at chordwise stations of $x/c = 0.4$ and 0.6 . Figure 3.9 shows the chordwise stations in which the pressure coefficient values are extracted and compared.

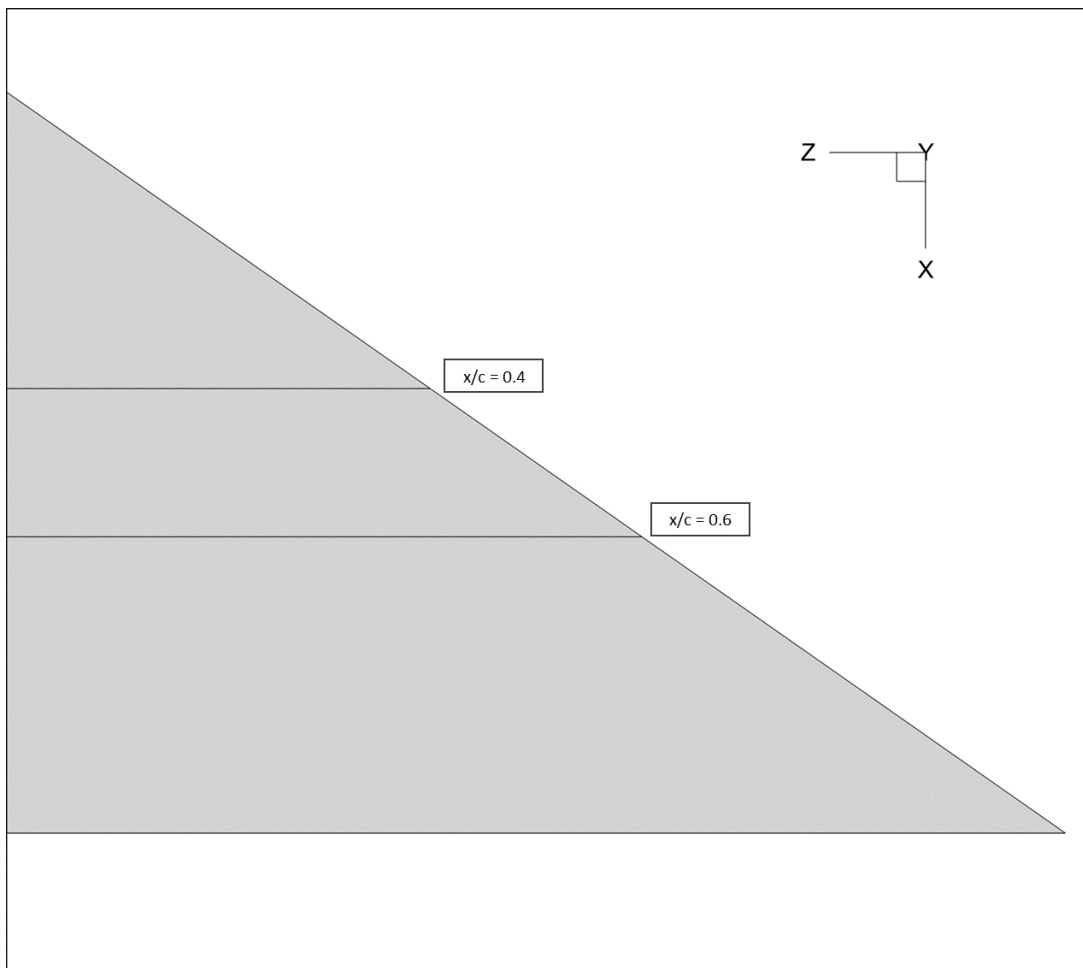
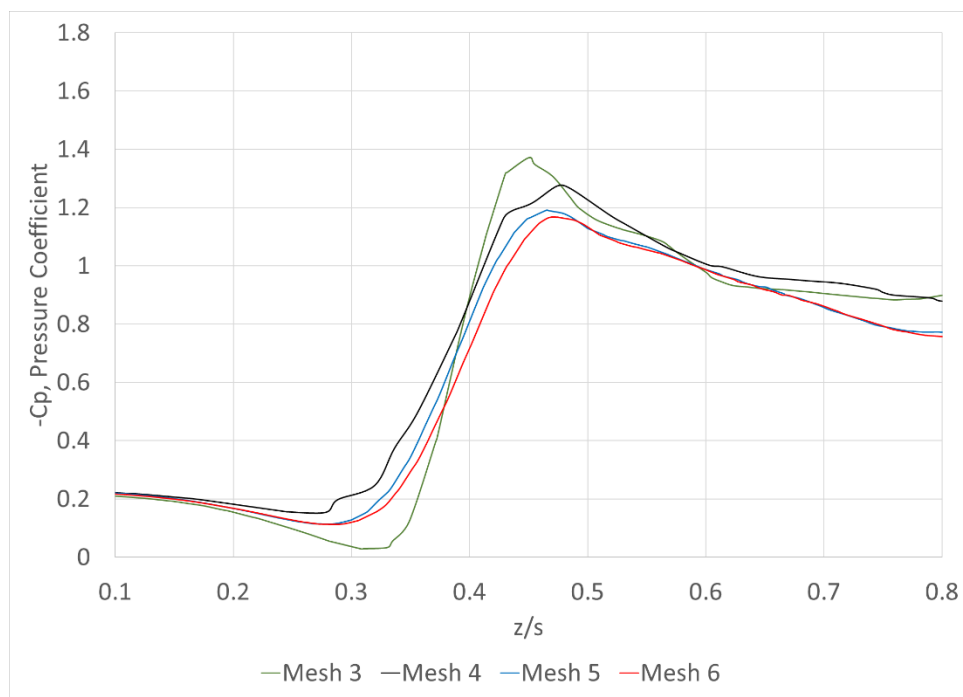
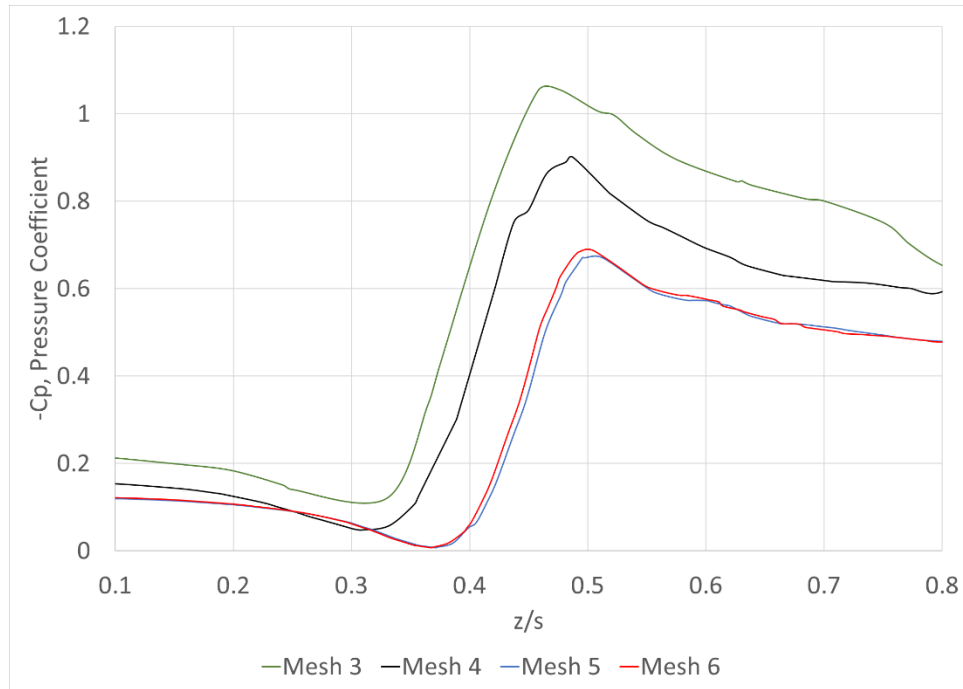


Figure 3.9. Chordwise stations of pressure coefficient, Cp data extract

The Cp distribution are drawn and presented in Figure 3.10 for four meshes at each chordwise stations mentioned above. It is clear that Mesh 5 results are sufficiently close to the outcome of the densest grid, Mesh 6. Especially, in the chordwise station $x/c = 0.40$, suction peak values and the rest of the distribution are nearly identical when they are compared to results produced by other meshes.



a)



b)

Figure 3.10. Pressure coefficient, $-C_p$ profiles of chordwise stations a) $x/c = 0.4$, b) $x/c = 0.6$

The pressure coefficient contours given in the Figure 3.11 reveals how well the primary vortical structure is resolved in different mesh densities. Drawn with the same min and max values of C_p , the contours become indistinguishable after Mesh 4.

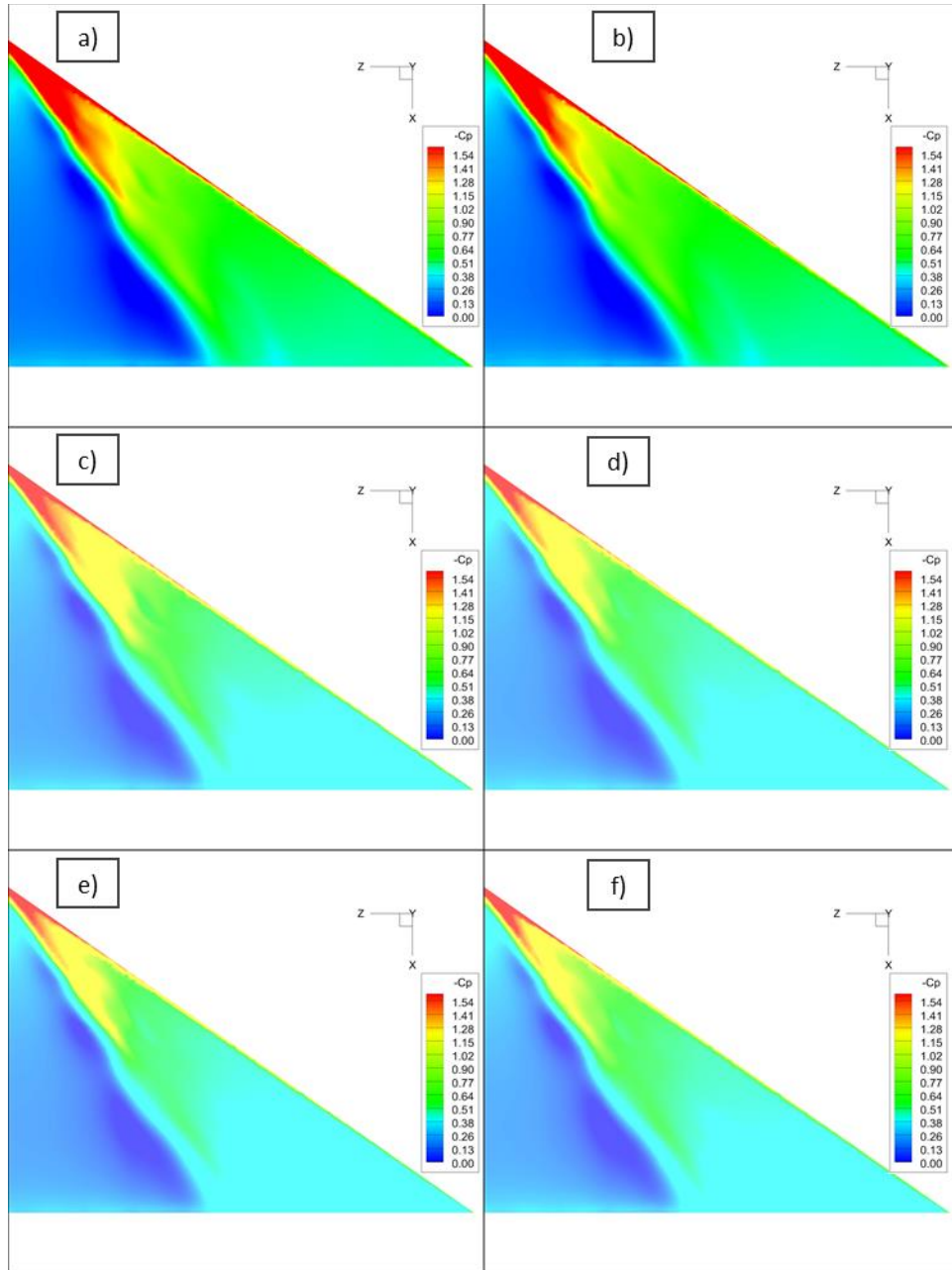
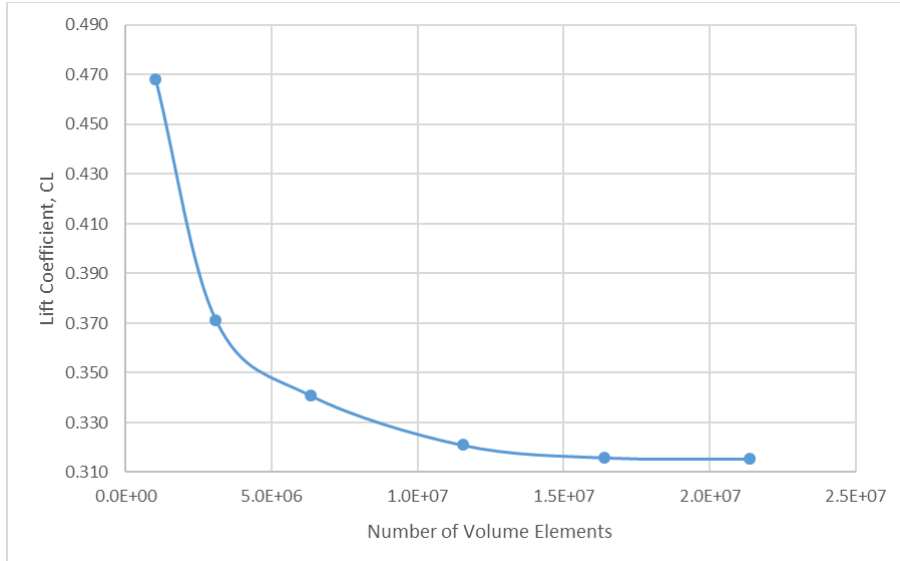
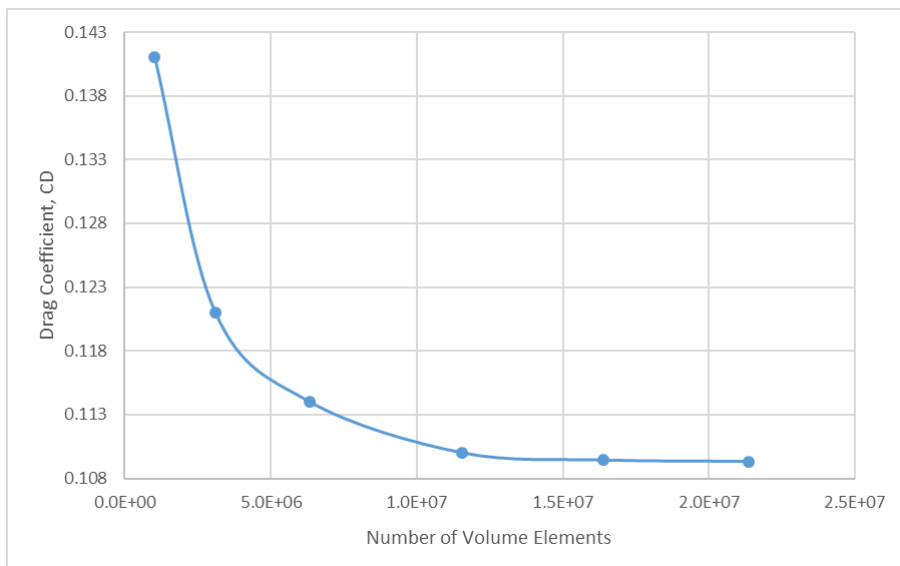


Figure 3.11. Pressure coefficient, $-C_p$ Contours a) Mesh 1 b) Mesh 2 c) Mesh 3 d) Mesh 4, e) Mesh 5, f) Mesh 6

As final considerations for the mesh independency, the aerodynamic coefficients of the delta wing with four different meshes are examined. The lift (CL) and drag (CD) coefficients are presented in the Figure 3.12 with respect to the number of elements of all meshes.



a)



b)

Figure 3.12. Aerodynamic coefficients of four meshes, a) CL, b) CD

It is seen that starting from Mesh 4, the aerodynamic coefficients of the delta wing at hand changes insignificantly. Mesh 6 is the densest mesh that can be put into use in terms of aerodynamic analysis. However, it requires a heavy computational power which is not very suitable with the time scale and resource of this study. It is also derived from the results that the max error is around 1% in aerodynamic coefficients between 4th and 6th meshes. With the guidance of the results presented in the grid independency study, Mesh 5, which produced much more successful results compared to its predecessors and exhibiting very close quality to Mesh 6 as assessed above, is chosen as the final grid to be proceeded to the validation study as it balances the relation between the solution accuracy and the computational load.

3.5. The Validation Study

After obtaining the final grid in the mesh independency, the complete accuracy of the Mesh 5 and the computational model has been put to the test with the results of the experimental wind tunnel study of Gülsuçan [7]. In the wind tunnel tests, delta wings with identical geometric features, except their thickness-to-chord ratios, are subjected to a freestream velocity of 4.97 m/s which corresponds to the Reynolds number of 3.5×10^4 and also angles of attack was chosen as 4°, 6°, 8° and 10°. Experimental results which are used for the purpose of validating the numerical outcome were the pressure coefficient distributions on the leeward surface of the delta wing gathered with the pressure taps located at the axial station $x/c = 0.44$ for all the angles of attack mentioned and for the wings with thickness-over-chord ratio, $t/c = 0.0475$ and 0.1900. Figure 3.13 and Figure 3.14 shows the negative pressure coefficient values on the axial station for the thinnest and thickest delta wing respectively.

When Figure 3.13, containing the pressure coefficient distribution of the delta wing with $t/c = 0.0475$, for all angles of attack at Reynolds number 3.5×10^4 , the difference between max and min pressure coefficient values are high which signifies

the existence of a strong and stable vortical structure. In other words, as angle of attack increases, vortex breakdown phenomenon is not happening at the $x/c = 0.44$ station.

Experimental data provides enough pressure coefficient values to infer the location of the suction peak. At $\alpha = 4^\circ$, the suction peak on the leeward side of the delta wing occurs at the axial station located between $z/s = 0.45$ and 0.50 . Numerical results for the same case exhibit the same behavior and gives a suction peak value of $-C_p = 0.8061$ at an exact location of $z/s = 0.4989$. The suction peak pressure coefficient values for the wing with $t/c = 0.0475$ is increased for $\alpha = 6^\circ$ and 8° begins to decrease at $\alpha = 10^\circ$ which is consistent with the experimental study.

Numerical results also provide an accurate approximation of the behavior of the location of the suction peak which signifies where the leading-edge vortex core line lies. As in the experimental study, with the increase of the angle of attack, vortex core line begins to move inboard (to the delta wing centerline). Same behavior is successfully captured in the numerical results. The location and the C_p values of the suction peaks with respect to angle of attack is given in the Table 3.7.

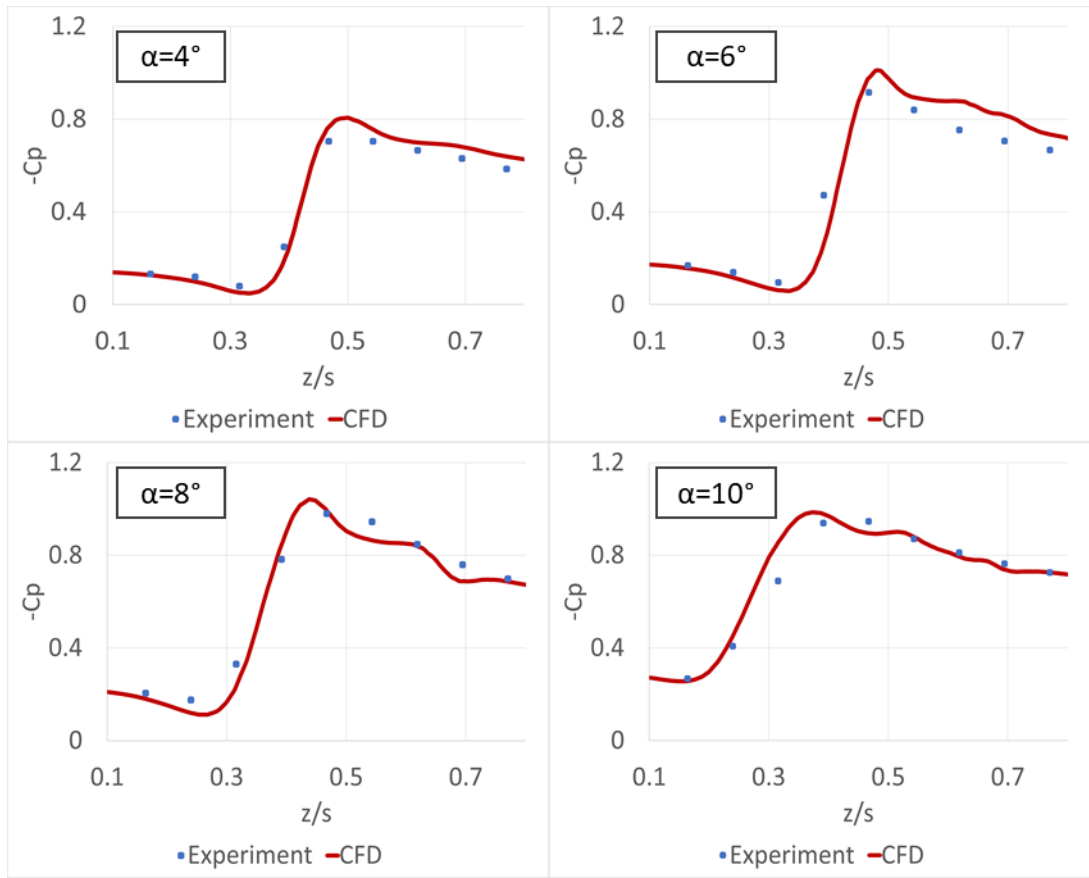


Figure 3.13. The comparison of the dimensionless pressure coefficient distribution, $-C_p$ of $t/c = 0.0475$ along spanwise direction at $x/c = 0.44$ at $RE = 35000$

Table 3.7. The location and C_p value of the suction peak with $t/c = 0.0475$ at varying angles of attack

Delta Wing with $t/c = 0.0475$		
Angle of Attack	Suction Peak Location (z/s)	Pressure Coefficient $-C_p$
4°	0.4989	0.8061
6°	0.4847	1.0095
8°	0.4377	1.0417
10°	0.3739	0.9851

As Figure 3.14 reveals, for the angles of attack $\alpha = 4^\circ$, 6° and 8° , a stable leading-edge vortex is still present at the axial station $x/c = 0.44$ for the delta wing with $t/c =$

0.1900 at Reynolds number 3.5×10^4 . However, at $\alpha = 10^\circ$, it is seen C_p distribution became flat. This situation indicates the presence of a vortex breakdown. Also, C_p variation of the other angles of attack become more and more flattened, that is the difference between the maximum and minimum pressure coefficient value is decreasing, with the increase of angle of attack. This behavior points out that the swirling strength of the leading-edge vorticity is decreasing and vortex breakdown is imminent. As it is suggested in the experimental study, increasing thickness-to-chord ratio has a similar effect as the increase in the angle of attack. Same behavior is successfully captured in the CFD analysis.

With the increase in angle of attack, the suction peak pressure coefficient value begins to fall down immediately. Although the initial value of the C_p is higher when compared to the results of the thin wing, the susceptibility of the pressure value is seen to be affected dominantly by the increase in the wing thickness.

The suction peak location is also moving inboard to the centerline of the delta wing, as similar shift is also seen with the wing with $t/c = 0.0475$. Therefore, the shifting behavior of the vortex core line is not affected by the difference in the thickness but rather related by the change in the angle of attack. In Table 3.8, the suction peak pressure coefficient location and values are given with respect to varying angle of attack.

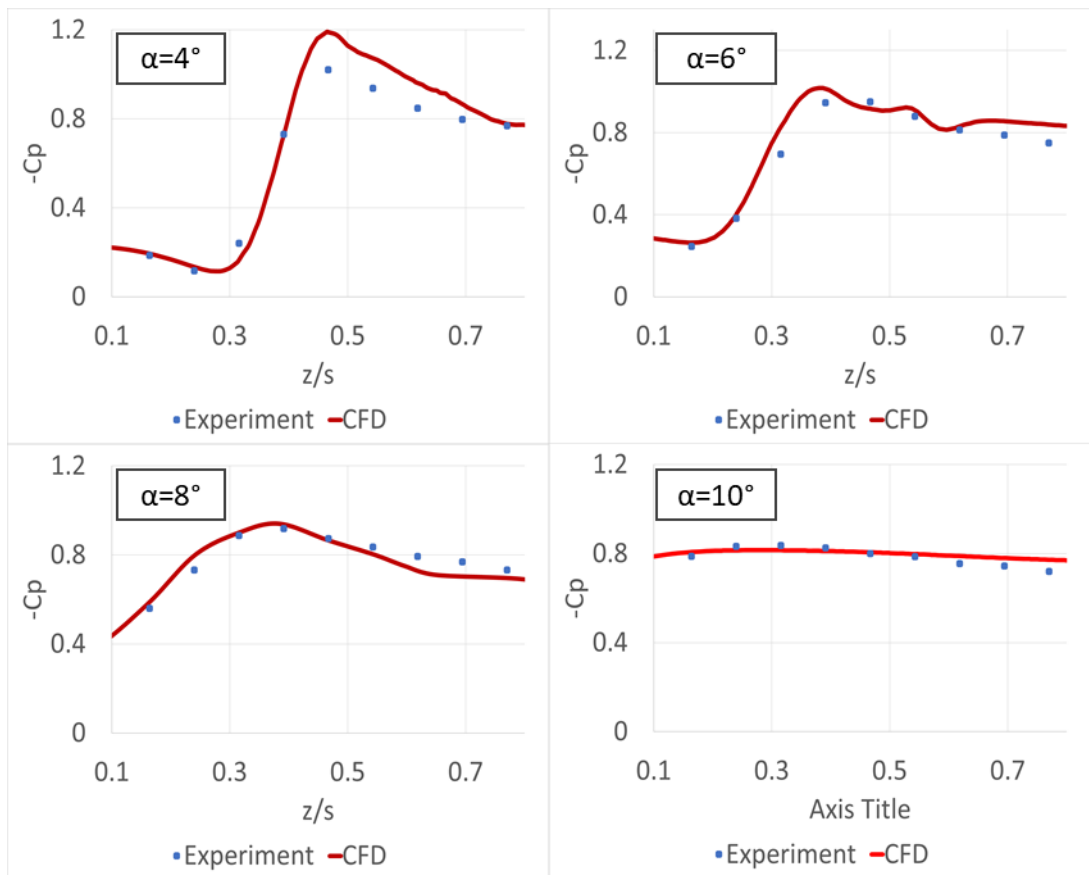


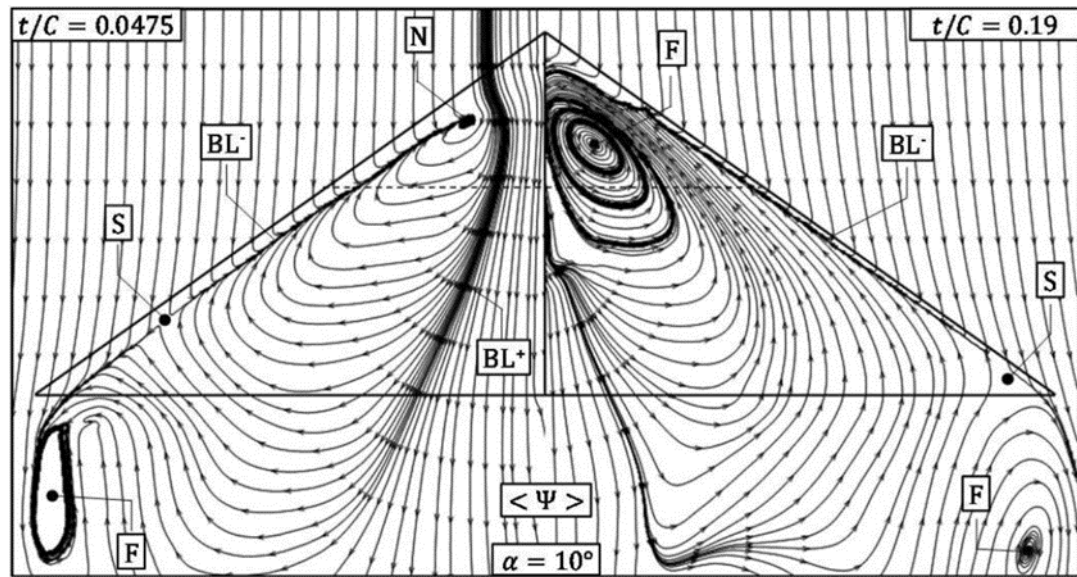
Figure 3.14. The comparison of the dimensionless pressure coefficient distribution, - C_p of $t/c = 0.1900$ along spanwise direction at $x/c = 0.44$ at $RE = 35000$

Table 3.8. The location and C_p value of the suction peak with $t/c = 0.1900$ at varying angles of attack

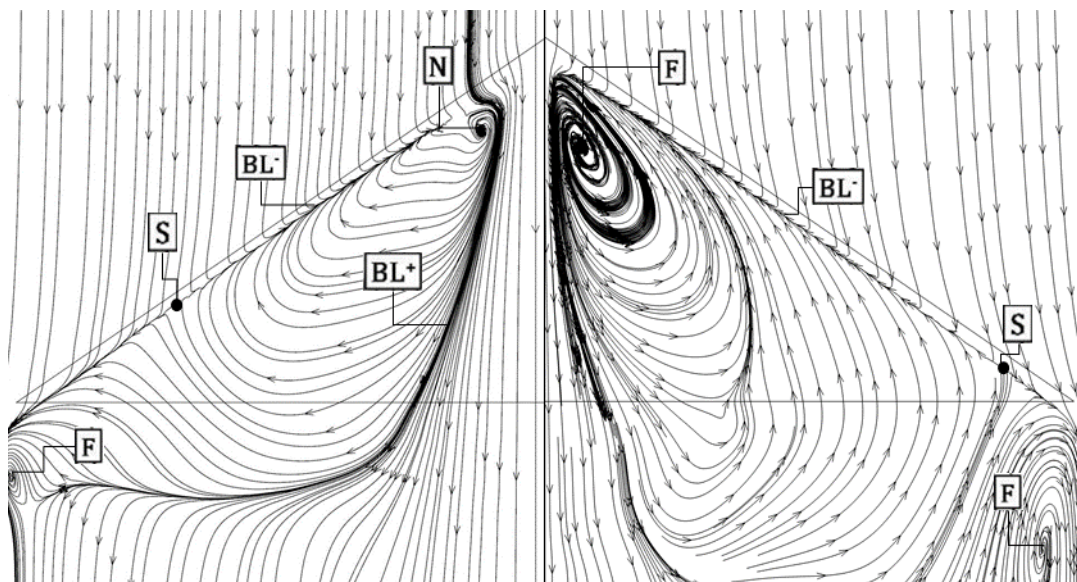
Delta Wing with $t/c = 0.1900$		
Angle of Attack	Suction Peak Location (z/s)	Pressure Coefficient - C_p
4°	0.4651	1.1907
6°	0.3870	1.0173
8°	0.3836	0.9414
10°	0.2810	0.8153

Another part of the validation study is the comparison of the near surface streamlines, given in Figure 3.15, at $\alpha = 10^\circ$, for the delta wings with $t/c = 0.0475$ and 0.1900 . When the numerical and experimental results of both wings are examined, it can be seen that the streamlines tend to diverge from the positive bifurcation line BL^+ . Similar to the vortex core line behavior, when thickness-to-chord ratio is increased, bifurcation line tends to move to the centerline of the delta wing. The negative bifurcation lines BL^- are both present near the leading-edges signifying the line of separation from both wing leeward surfaces. In $t/c = 0.0475$, BL^- terminates at the nodal point, N where the streamlines tend to converge, whereas, in $t/c = 0.1900$ the negative bifurcation line tends to bind the streamline in a swirling motion around the focal point F , near the apex of the delta wing. Moreover, the saddle point, the point where streamlines changes direction, is moving to the trailing edge of the wing with the increase in the thickness-to-chord ratio.

In brief, the results of the validation suggest that the numerical model at hand with Mesh 5 and SST $k-\omega$ turbulence model with curvature correction along with remaining solver parameters has been successful to simulate the flow and surface properties intrinsic to delta wings in the experimental wind tunnel study [7].



a)



b)

Figure 3.15. The comparisons of the near surface velocity streamlines of delta wings, a) Experiment with $t/c = 0.0475$ (left) & 0.1900 (right), b) CFD with $t/c = 0.0475$ (left) & 0.1900 (right), at $\alpha = 10^\circ$

CHAPTER 4

EFFECTS OF THICKNESS-TO-CHORD RATIO

In this chapter, effects of thickness-to-chord ratio and higher Reynolds number on the flow field and the aerodynamics performance of the delta wings will be investigated in detail.

As the flow regime and delta wing geometry changes, flow field properties and aerodynamics characteristics of the delta wings are also changing. By the works of Traub et al. [69], Ghazijahani [43], it is shown that thickness-to-chord ratio of a delta wing can substantially change the flow field around the delta wing and aerodynamic characteristics.

Establishing a capable computational grid and numerical model in the previous chapter, delta wings with different thickness-to-chord ratios are subjected to much higher angles of attack under different Reynolds numbers to see the effects of both varying flow conditions and geometric properties of the delta wings on the flow field and aerodynamic performance.

The effects of the varying Reynolds number are studied extensively in the literature. An increase in the Reynolds number in general, is seen to be pushing the vortex breakdown location up to the apex which leads to the increase in the pressure on the leeward surface. Having a vortex breakdown at earlier stations lessen the contribution of the vortex lift to the total lift of the delta wing. On the other hand, wing planforms generate higher values of lift and drag coefficients when the Reynolds number is increased due to the increase in the flow momentum which is caused by the momentum difference between upper and lower surfaces of the wings.

Moreover, increasing the thickness-to-chord ratio increases the suction peak pressure coefficient values at low values of angle of attack as validated in the previous chapter. The main interest at hand is derived as follows. While higher thickness-to-chord ratio increases the suction, pressure values for an interval of angle of attack, and possibly increasing the vortex lift for a certain region, it can also cause a premature existence of a vortex breakdown which induces high pressures on the leeward surface therefore decreasing the total lift of the delta wing. Moreover, increasing the thickness-to-chord ratio significantly affects the angle of attack range where three-dimensional separation occurs. To investigate this situation, a CFD matrix is constructed with varying Reynolds numbers, angles of attack and thickness-to-chord ratios. The CFD matrix follow in the numerical analysis is given in the Table 4.1.

Table 4.1. *The CFD matrix used in the numerical analysis*

Wing Thickness (mm)	Thickness-to-Chord Ratios (t/c)	Reynolds Numbers	Corresponding Velocity (m/s)	Angles of Attack
5	0.0475	3.5×10^4 3.0×10^5	4.97 42.58	0° to 40°
20	0.1900	3.5×10^4 3.0×10^5	4.97 42.58	0° to 40°
2	0.0190	3.5×10^4 3.0×10^5	4.97 42.58	5°, 9° 13°, 17°
12	0.1143	3.5×10^4 3.0×10^5	4.97 42.58	5°, 9° 13°, 17°

The CFD analysis set for the delta wings with the thickness-to-chord ratios of 0.475 and 0.1900 has a broader angle of attack range primarily to investigate the flow field and the aerodynamic characteristics which was not available in the experimental study [6]. Later on, Reynolds Number, which could not be increased in the wind tunnel due to the limitations, is increased to see whether the thickness effects are irrespective of the free stream velocity. While the delta wings with thickness-to-chord ratios of 0.0190, which was too thin to be tested in the wind tunnel, and

0.1143 are added to serve as an extension to validate the aerodynamic performance results obtained by the first analysis set.

4.1. Flow Visualization

This includes the detailed investigation of the flow field regarding the changes in the thickness-to-chord ratio and Reynolds number. Geometric changes and varying flow regime can significantly affect the flow properties near the surfaces of the delta wings. As it can be inferred from the CFD matrix, the number of the resultant cases are quite extensive. For this reason, flow visualization for all cases become quite cumbersome. In order to remedy this drawback and still have meaningful postprocessing, a number of selected cases which reveals the relation between the flow topology and parameters which are given in the CFD matrix is used in the flow visualization. The classification of the cases to be used in the postprocessing is selected to identify the important flow phenomena such as, the creation and the movement of the focal and nodal points, bifurcation lines, movement of the vortex core lines with respect to changing thickness and angle of attack. A cut plane is created at the axial station of $x/c = 0.44$, and axial velocity component of the flow field embedded with the projection of the velocity vector plots are gathered. From the observations a preliminary overview of the solution data suggest that thickness-to-chord ratio has a strong influence in the flow field just as the difference in the Reynolds number and angle of attack.

To understand effects of the mentioned parameters such as, changes in the pressure fields and streamlines on the leeward surface, swirling strengths of the vortical structures and movements of the vortex core lines, visualizations of the axial velocities are examined for the delta wings with thickness-to-chord ratios 0.0475 and 0.1900 at Reynolds numbers, 3.5×10^4 and 3.0×10^5 for a variety of angle of attacks.

4.1.1. Near Surface Patterns

In near surface visualizations, presence of a leading-edge vortex manifest itself as the primary reattachment line where streamlines diverge. Through the primary reattachment line, vortex core has high axial velocity which lowers the pressures on the leeward surface significantly. This property is captured by looking at the negative Cp distributions on the top surface. Leading-edge vorticities create a sudden jump in the pressure coefficient distribution at axial stations and acts as a suction agent. Highest value observed in the -Cp distribution at an axial station is called the suction peak.

As angle of attack increases, flow reattachment becomes harder and also primary reattachment line (vortex core line) moves inboard. At sufficiently high angle of attack, leading-edge vortex cannot fully reattach itself at an axial station near the trailing edge, loses its core velocity and bursts. This phenomenon is also known as vortex breakdown. When vortex is broken down, pressure starts rising up and increased pressure starts to reverse the oncoming flow. Moreover, vortex bursts manifest itself as the flattening behavior seen at the pressure distributions at axial stations. Flow reversal becomes much severe with increasing angle of attack and at some point, it leads to the creation of the focal points in the near surface.

Creation of the focal points signifies the flow trying to separate from the leeward surface. As angle of attack increases further, focal point moves to the trailing edge of the wing. At a certain point, flow is completely separated from the wing and three-dimensional flow separation occurs. At that stage, near surface streamlines show a reversed flow from the trailing edge to the leading edge, Cp contours show high but nearly uniform distribution on leeward surface.

Changes in the angle of attack affects the formation of the leading-edge vorticities which are the dominant flow property in delta wing flows. Figure 4.1 contains the near surface velocity streamline and negative pressure coefficient contours for the

wing with $t/c = 0.0475$, at angles of attack, $\alpha = 3^\circ, 5^\circ, 7^\circ \& 9^\circ$ for $RE = 3.5 \times 10^4$. It can be observed that the primary reattachment line moves inboard (to the delta wing center line) with the increase in the α values. Moreover, $-C_p$ contours reveal that with the increase in angle of attack, vortex system elongates to the trailing edge, lowering the pressures on the leeward surface edge up to $\alpha = 7^\circ$ and then pressures rise at the trailing edge and flow reversal begins.

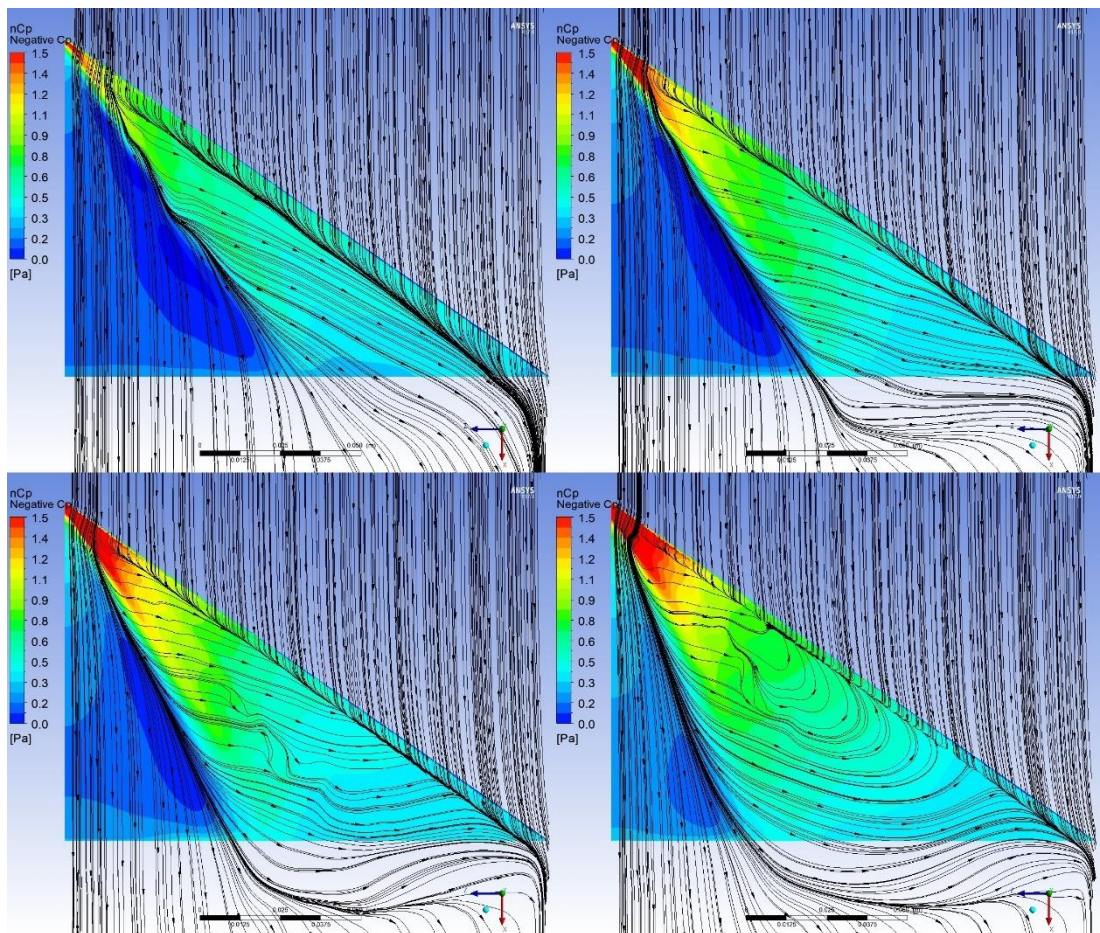


Figure 4.1. Near surface streamlines and surface C_p distributions of delta wing with $t/c = 0.0475$ at $RE = 35000$ and $\alpha = 3^\circ, 5^\circ$ (top), $7^\circ, 9^\circ$ (bottom)

Figure 4.2 contains the near surface velocity streamline and negative pressure coefficient contours for the wing with $t/c = 0.1900$, at angles of attack, $\alpha = 3^\circ, 5^\circ, 7^\circ \& 9^\circ$ for $RE = 3.5 \times 10^4$. It is seen that in terms of the location shift of the primary reattachment line, increasing the thickness-to-chord ratio has the same effect,

pushing the vortex core line inboard, as in the increasing angle of attack. On the other hand, for the wing with $t/c = 0.1900$, increase in the angle of attack directly shortens the length of the vortex system, increasing the pressures on the top surface after $\alpha = 3^\circ$, starting the flow reversal phenomenon earlier. Moreover, increasing the t/c also caused the creation of the focal points on the near leeward surface indicating that flow starts to separate from the wing top surface.

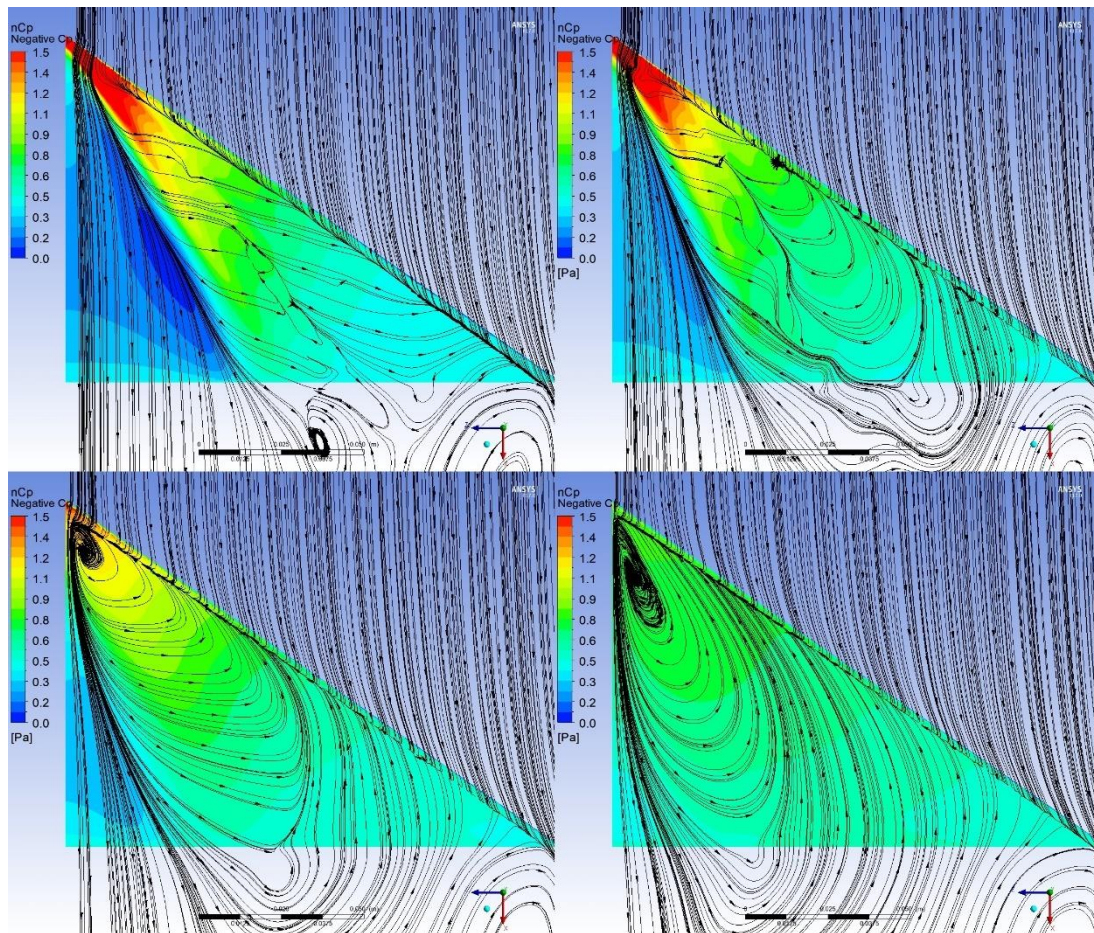


Figure 4.2. Near surface streamlines and surface Cp distributions of delta wing with $t/c = 0.1900$ at $RE = 35000$ and $\alpha = 3^\circ, 5^\circ$ (top), $7^\circ, 9^\circ$ (bottom)

To ascertain whether the effects seen with the change in thickness-to-chord ratio are also present, results for higher Reynolds Number are presented. Figure 4.3 contains the near surface velocity streamline and negative pressure coefficient contours for the wing with $t/c = 0.0475$, at angles of attack, $\alpha = 3^\circ, 5^\circ, 7^\circ$ & 9° for $RE = 3.0 \times 10^5$.

As seen in the cases with low Reynolds Number, an increase in the angle of attack moved the primary reattachment line to the wing centerline. Moreover, -Cp contours reveal that with the increase in angle of attack, vortex system elongates to the trailing edge, lowering the pressures on the leeward surface edge up to $\alpha = 5^\circ$ then boundaries of the low-pressure region get smaller through the wing apex.

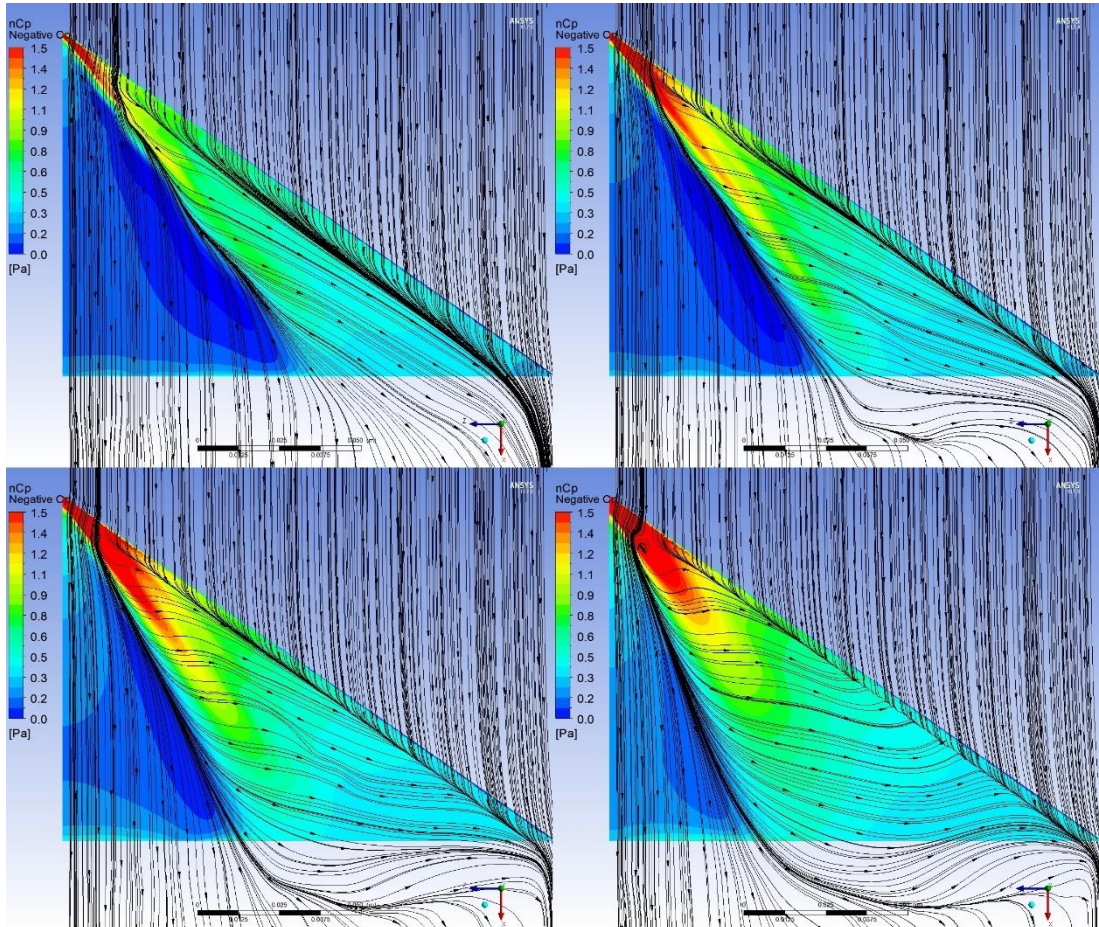


Figure 4.3. Near surface streamlines and surface Cp distributions of delta wing with $t/c = 0.0475$ at $RE = 300000$ and $\alpha = 3^\circ, 5^\circ$ (top), $7^\circ, 9^\circ$ (bottom)

To understand the effects of thickness-to-chord ratio, results of the thickest wing under $RE = 3.0 \times 10^5$, at same angles of attack is given in the Figure 4.4 which shows that the location of the vortex core line is pushed further to the centerline of the delta wing. On the other hand, for the wing with $t/c = 0.1900$, increase in the angle of attack has again shortened the length of the vortex system, increasing the

pressures on the top surface after $\alpha = 3^\circ$, starting the flow reversal phenomenon earlier. Moreover, increasing the t/c also caused the creation of the focal points on the near leeward surface indicating that flow starts to separate from the wing top surface.

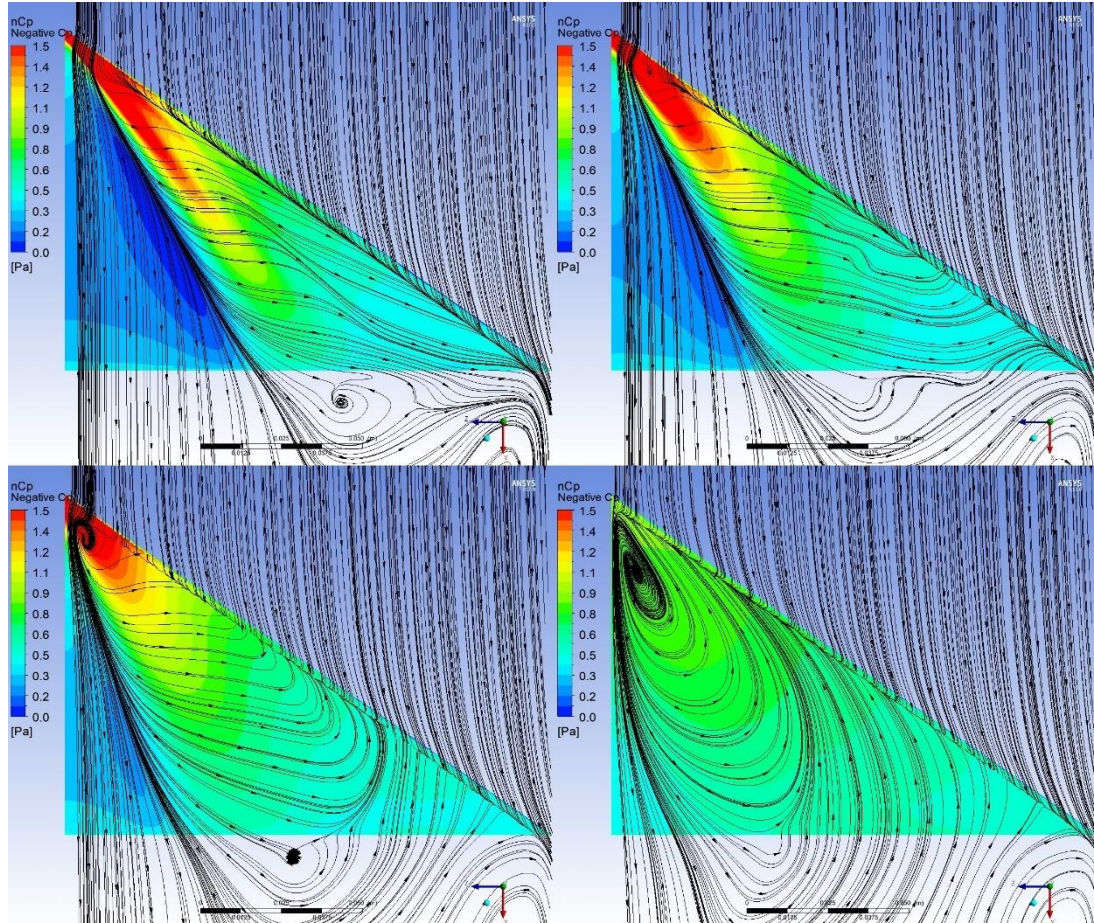


Figure 4.4. Near surface streamlines and surface Cp distributions of delta wing with $t/c = 0.1900$ at $RE = 300000$ and $\alpha = 3^\circ, 5^\circ$ (top), $7^\circ, 9^\circ$ (bottom)

It is observed that regardless of the Reynolds Number, thickness-to-chord ratio has a deteriorating effect on the structure of leading-edge vorticities and pressure distributions on the top surface. Moreover, t/c also promotes the creation of the focal points after which the three-dimensional flow separation from the leeward surface follows. The focal points and the swirling streamline structures on the leeward side of the delta wings are created by the flow trying to separate from the top surface.

Similar structures start to show themselves when angle of attack is increased. However, thickness-to-chord ratio is seen to be heavily influencing the location of those structures as well. Figure 4.5 contains the near surface velocity streamline and negative pressure coefficient contours for the wing with $t/c = 0.0475$, at angles of attack, $\alpha = 12^\circ, 14^\circ, 16^\circ \& 18^\circ$ for $RE = 3.5 \times 10^4$. It is observed that flow reversal process has already begun and focal points of the leeward surface is moving towards to the trailing edge of the delta wing with increasing angles of attack. Low pressure region seen near the apex at $\alpha = 12^\circ$, is diminished and pressures rose up, also becoming more and more uniform with the increase in the angle of attack.

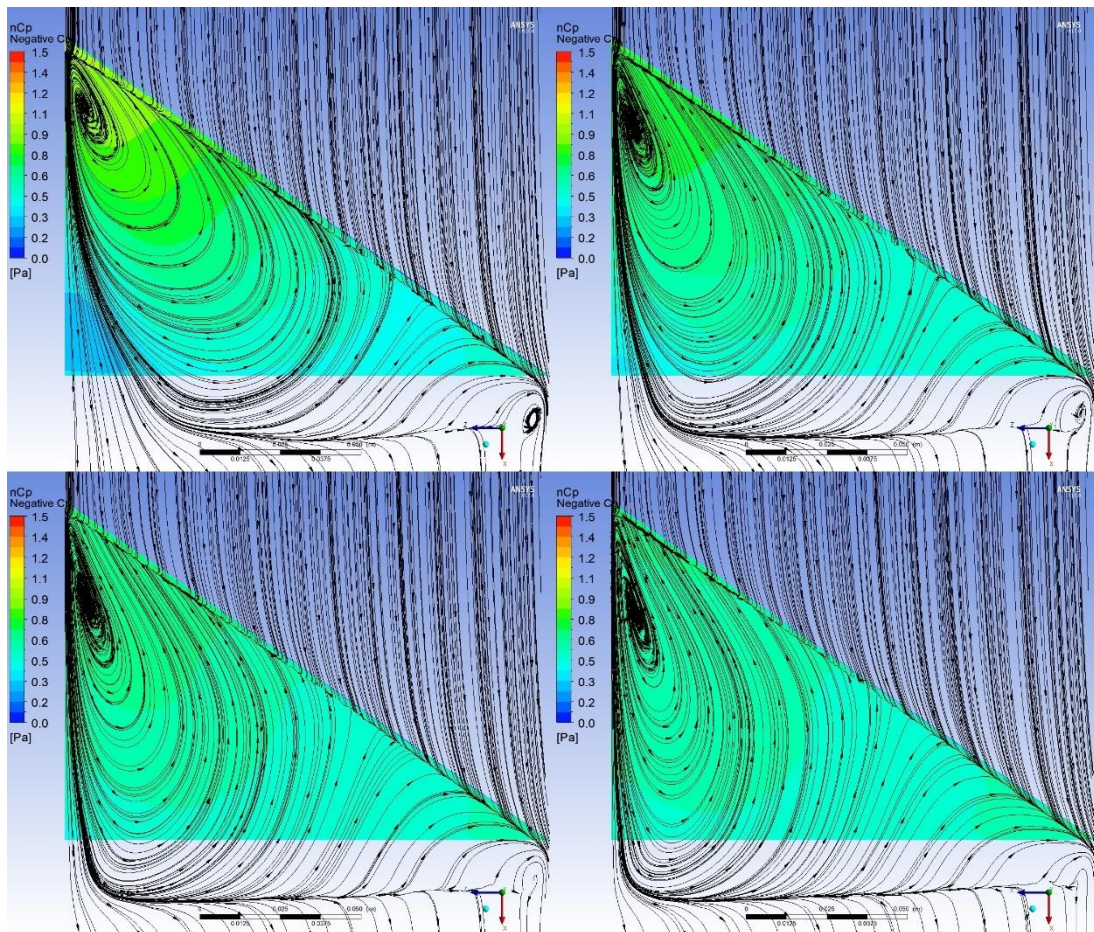


Figure 4.5. Near surface streamlines and surface Cp distributions of delta wing with $t/c = 0.0475$ at $RE = 35000$ and $\alpha = 12^\circ, 14^\circ, 16^\circ, 18^\circ$ (top, bottom)

Increasing the thickness-to-chord ratio, as seen in the Figure 4.6, has also pushed the focal points on the leeward surface further to the trailing edge of the delta wing and increased the pressures on the top surface, thus promoting the three-dimensional separation process.

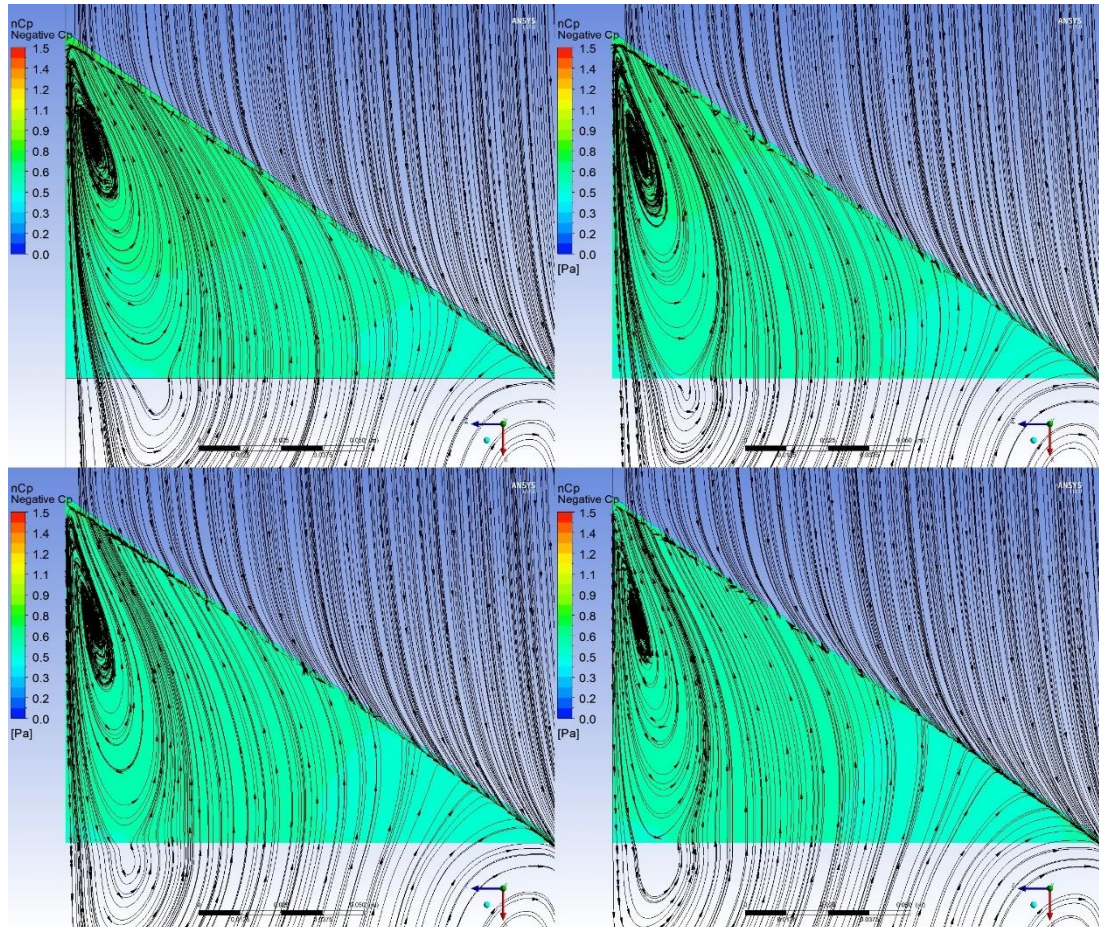


Figure 4.6. Near surface streamlines and surface Cp distributions of delta wing with $t/c = 0.1900$ at $RE = 35000$ and $\alpha = 12^\circ, 14^\circ$ (top), $16^\circ, 18^\circ$ (bottom)

To complement the fact that effects of the thickness-to-chord ratio is consistent at other flow regimes, results for the $RE = 3.0 \times 10^5$ are also presented at the same angles of attack. As it is seen from the Figure 4.7 increasing the angle of attack has

again pushed the focal points to the trailing edge of the wing. Low pressure region near the apex has become smaller and pressures rose up, becoming more uniform.

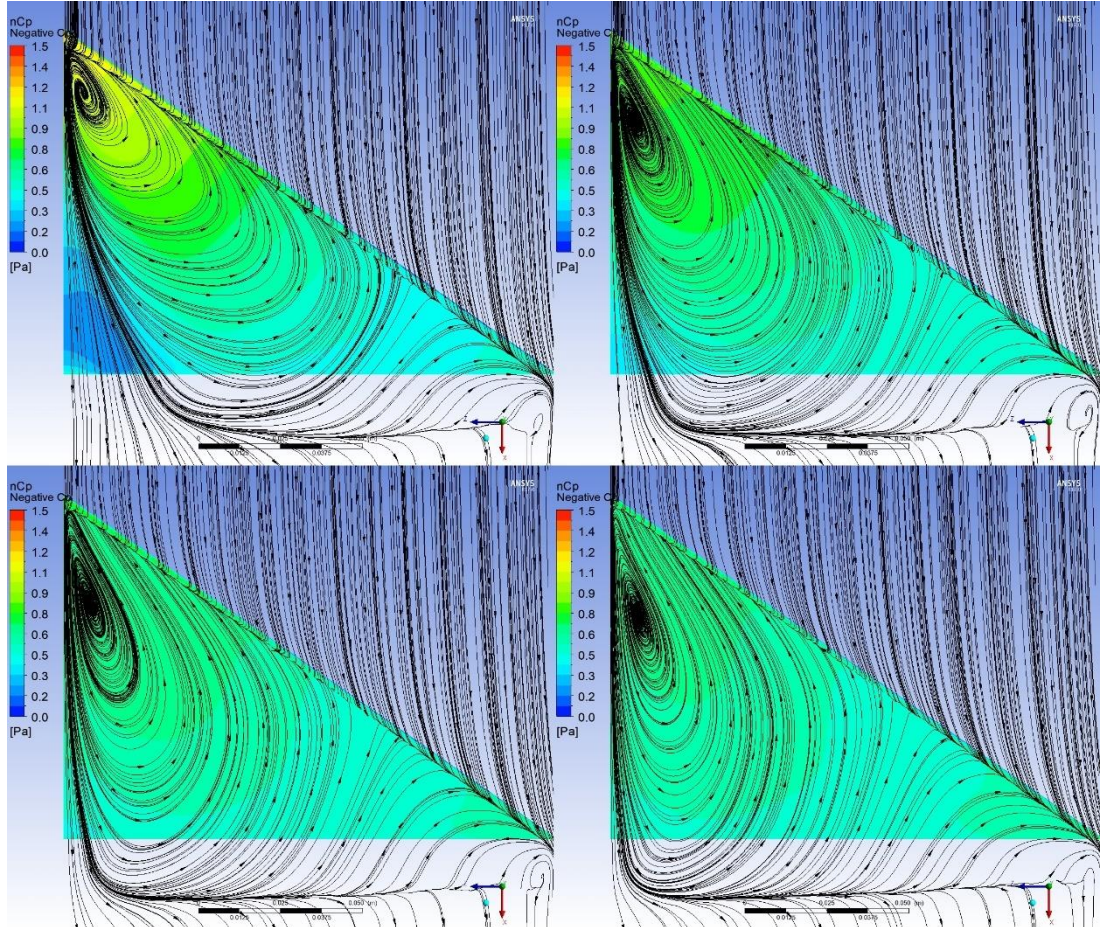


Figure 4.7. Near surface streamlines and surface Cp distributions of delta wing with $t/c = 0.0475$ at $RE = 300000$ and $\alpha = 12^\circ, 14^\circ$ (top), $16^\circ, 18^\circ$ (bottom)

Increasing the thickness-to-chord ratio had similar effects, pushing down the focal points to the trailing edge of the wing on the leeward surface, forcing the flow to separate itself from the surface as seen in the Figure 4.8. Results indicate that increasing the thickness-to-chord ratio is an amplifying factor for the three-dimensional flow separation and as effective as the increasing angles of attack in that

manner. Same aspect can be seen in the pressure distribution as well, increasing t/c also increased the pressures on the leeward surface.

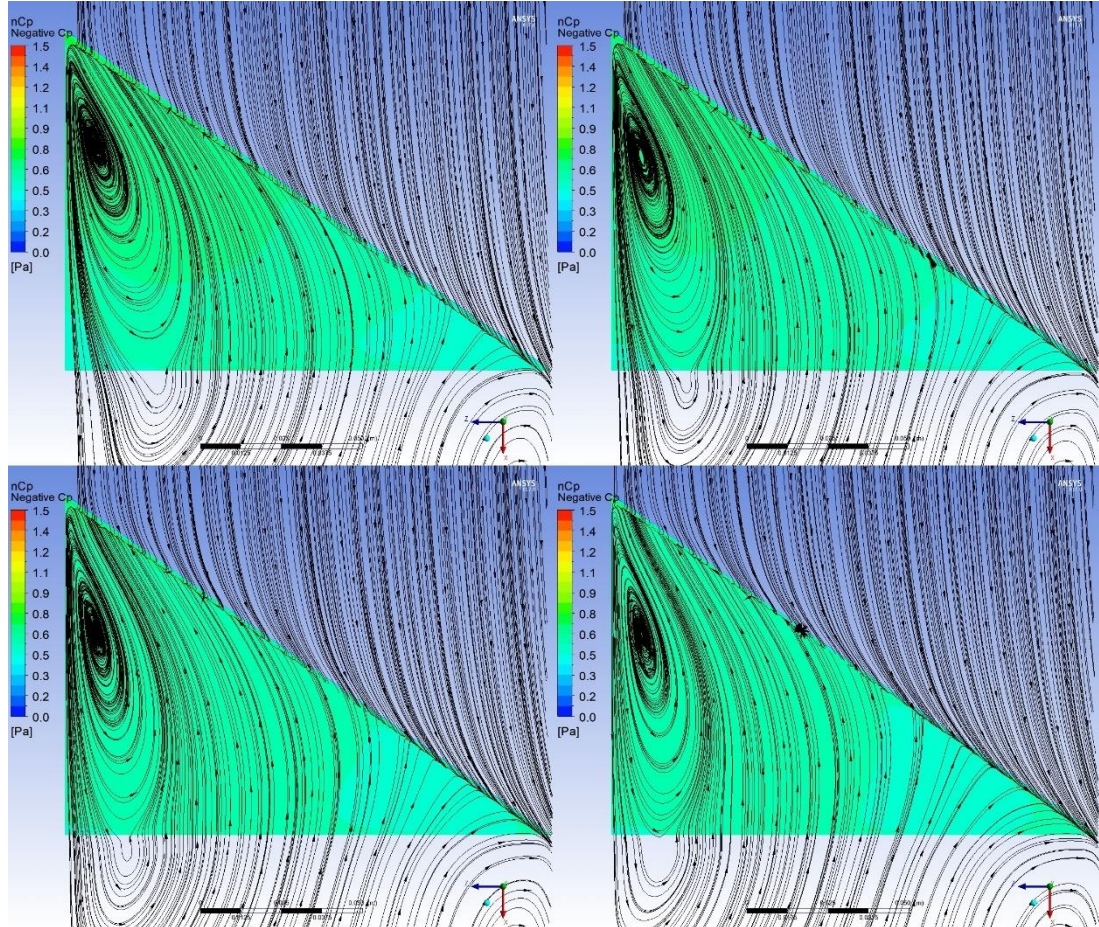


Figure 4.8. Near surface streamlines and surface Cp distributions of delta wing with $t/c = 0.1900$ at $RE = 300000$ and $\alpha = 12^\circ, 14^\circ$ (top), $16^\circ, 18^\circ$ (bottom)

Also, above an angle of attack value of 25° , flow is completely separated from the leeward surface and flow reversal is dominant. The effects of flow separation as the creation of the focal points and the swirling structures cannot be seen at the near surface streamlines as the increase in the angle of attack further pushes the broken down vortical structures to a location higher in the flow domain.

As discussed in above, thickness-to-chord ratio effects along with the increase in the angle of attack, forces the leading-edge vortices and remaining structures to be located at much higher planes from the leeward surface. This leads to the decrease in the visibility of the focal points and swirling streamline structures on near surface. Also, three-dimensional flow separation causes pressures on the leeward surface to increase and become more homogenous. At Figure 4.9, the effects of the three-dimensional flow separation leading to flow reversal and pressure rise can be observed.

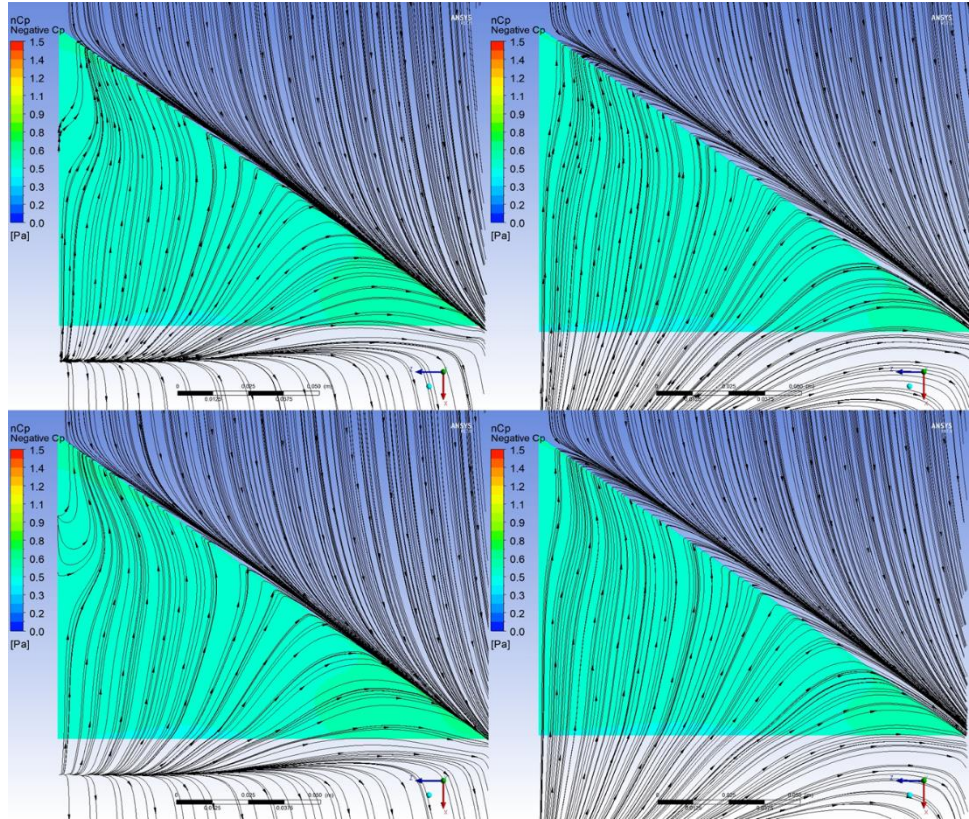


Figure 4.9. Near surface streamlines and surface Cp distributions of delta wing with $t/c = 0.0475$ (left), 0.1900 (right) at $RE = 35000$ (top), 300000 (bottom) at $\alpha = 30^\circ$

4.1.2. Cross-Flow Patterns

As LEVs pass over the leeward surface, some properties of vorticities change as it is affected by not only the wall of the delta wing but also the flight conditions such as free stream velocity and angle of attack. To monitor what changes LEV structures goes through, it is quite useful to take cross planes and compare the azimuthal vorticity and turbulent kinetic energy contours.

From the formation of the LEVs to their breakdown, turbulent kinetic energy levels in the vortex core remains low but slowly increasing. At the same interval, azimuthal vorticity contours show high levels because the strength of the vortical structure is intact. The instant vortex is burst, turbulent kinetic energy of the vortex core is at maximum and vorticity levels drops. After this instance, vorticities are displaced and diminishing as they travel. When three-dimensional flow separation from the surface happens, vortex system is completely detached, and fluctuation of both properties remain minimal at the near surface.

Figure 4.10 and Figure 4.11 located at axial station of $x/c = 0.44$ contain the contours of non-dimensional azimuthal vorticity and turbulent kinetic energy for the wing with $t/c = 0.0475$, at angles of attack, $\alpha = 3^\circ, 9^\circ, 14^\circ \& 20^\circ$ for $RE = 3.5 \times 10^4$ respectively. Results indicate that an increase in the angle of attack causes the vortex system to become detached and move in the normal direction of the leeward surface. Looking at both figures, at $\alpha = 3^\circ$, the vortex system is not yet broken down. Near $\alpha = 14^\circ$, the steep increase in the turbulent kinetic energy levels indicates that vortex system is no longer present and flow detachment is occurring. At higher angles of attack, vortex system is pushed upwards, losing both turbulent kinetic energy and vorticity levels as it disperses.

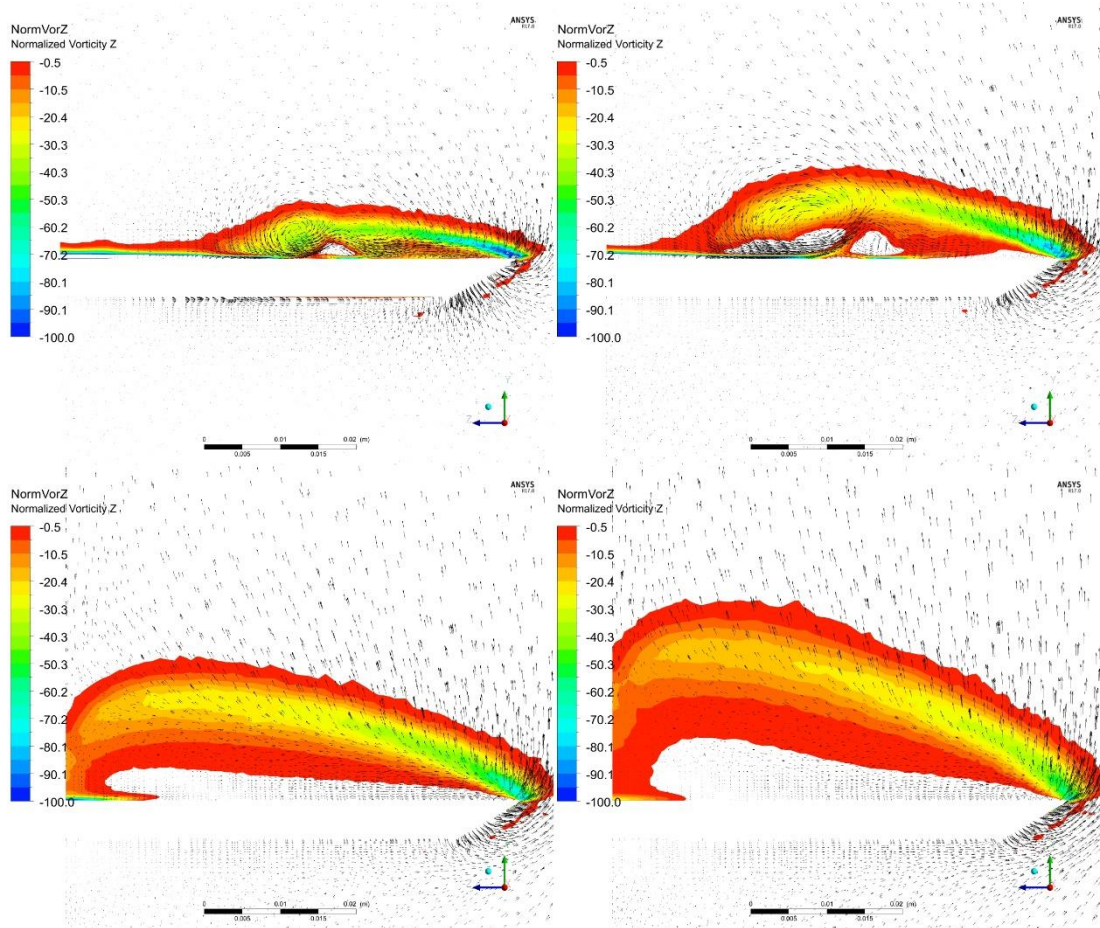


Figure 4.10. The comparisons of azimuthal vorticity contours of delta wing with $t/c = 0.0475$ at $RE = 35000$ and $\alpha = 3^\circ, 9^\circ, 14^\circ, 20^\circ$ (top),
 $14^\circ, 20^\circ$ (bottom) located at $x/c = 0.44$

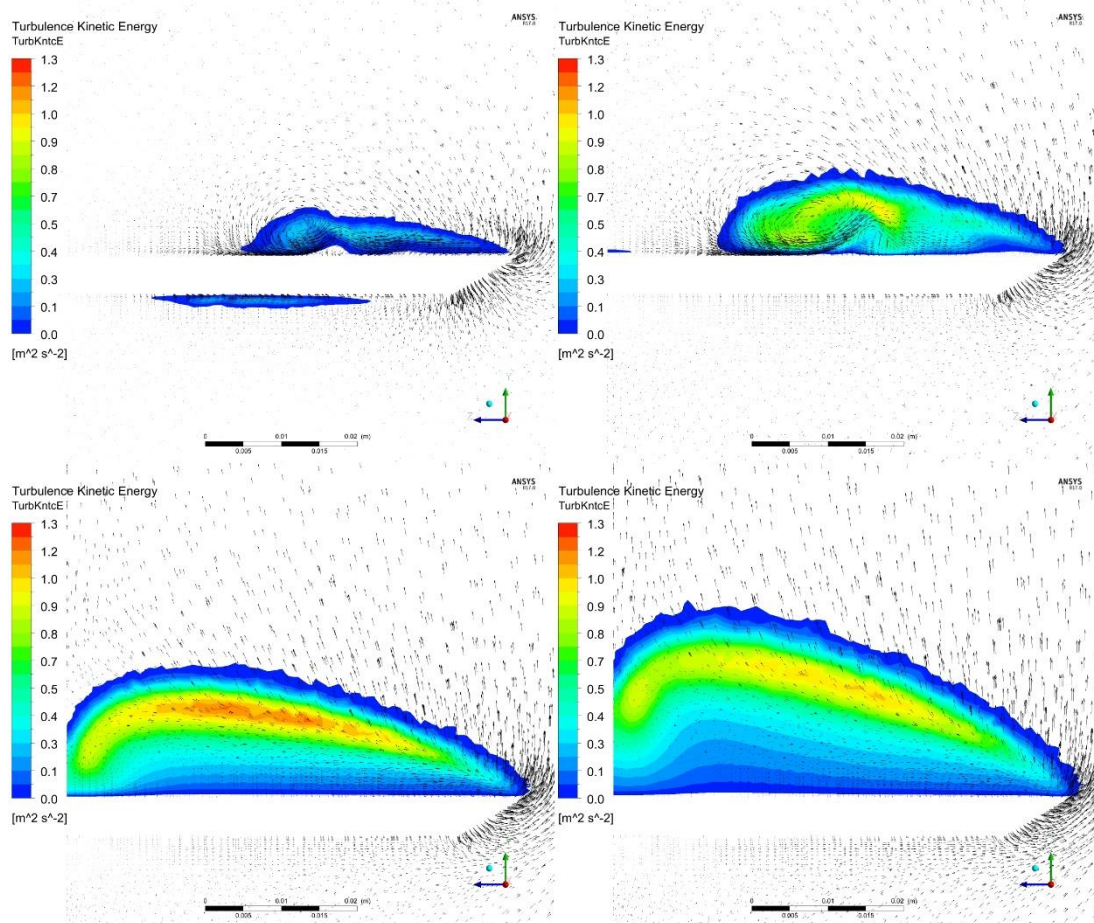


Figure 4.11. The comparisons of turbulent kinetic energy contours of delta wing with $t/c = 0.0475$ at $RE = 35000$ and $\alpha = 3^\circ, 9^\circ$ (top), $14^\circ, 20^\circ$ (bottom) located at $x/c = 0.44$

Figure 4.12 and Figure 4.13 contain the contours of non-dimensional azimuthal vorticity and turbulent kinetic energy for the wing with $t/c = 0.1900$, at angles of attack, $\alpha = 3^\circ, 9^\circ, 14^\circ$ & 20° for $RE = 3.5 \times 10^4$ respectively, revealing that increase in the thickness to chord ratio has promoted process mentioned above. For the same angles of attack, vortical structures are pushed further upstream in the normal direction of the leeward surface of the wing and the region where the vortical structures are influencing has grown for all angles of attack. This growth is due to the fact that increasing the thickness to chord ratio, in general, fastens the vortex breakdown and three-dimensional flow separation process as well as exhibiting the same effects as angle of attack regarding vortex strength and turbulence.

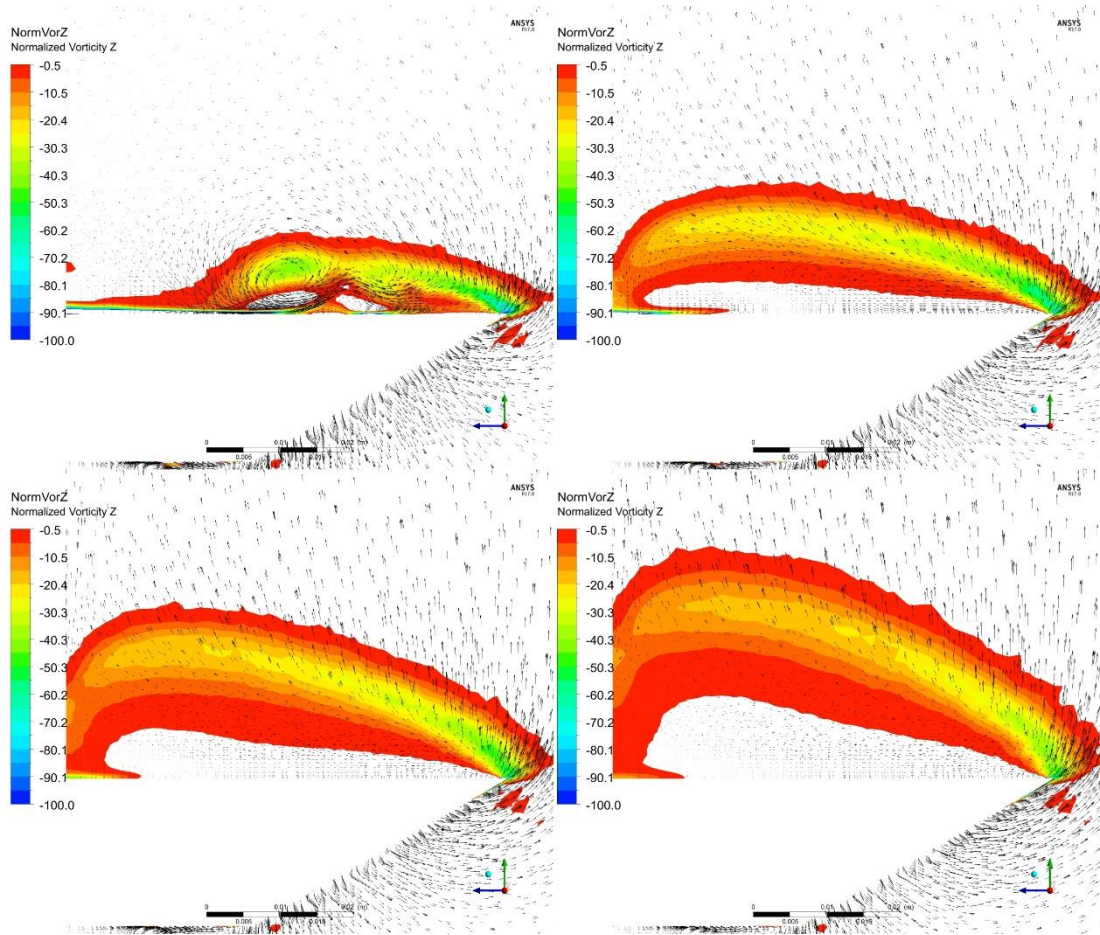


Figure 4.12. The comparisons of azimuthal vorticity contours of delta wing with $t/c = 0.1900$ at $RE = 35000$ and $\alpha = 3^\circ, 9^\circ, 14^\circ, 20^\circ$ (top), $14^\circ, 20^\circ$ (bottom) located at $x/c = 0.44$

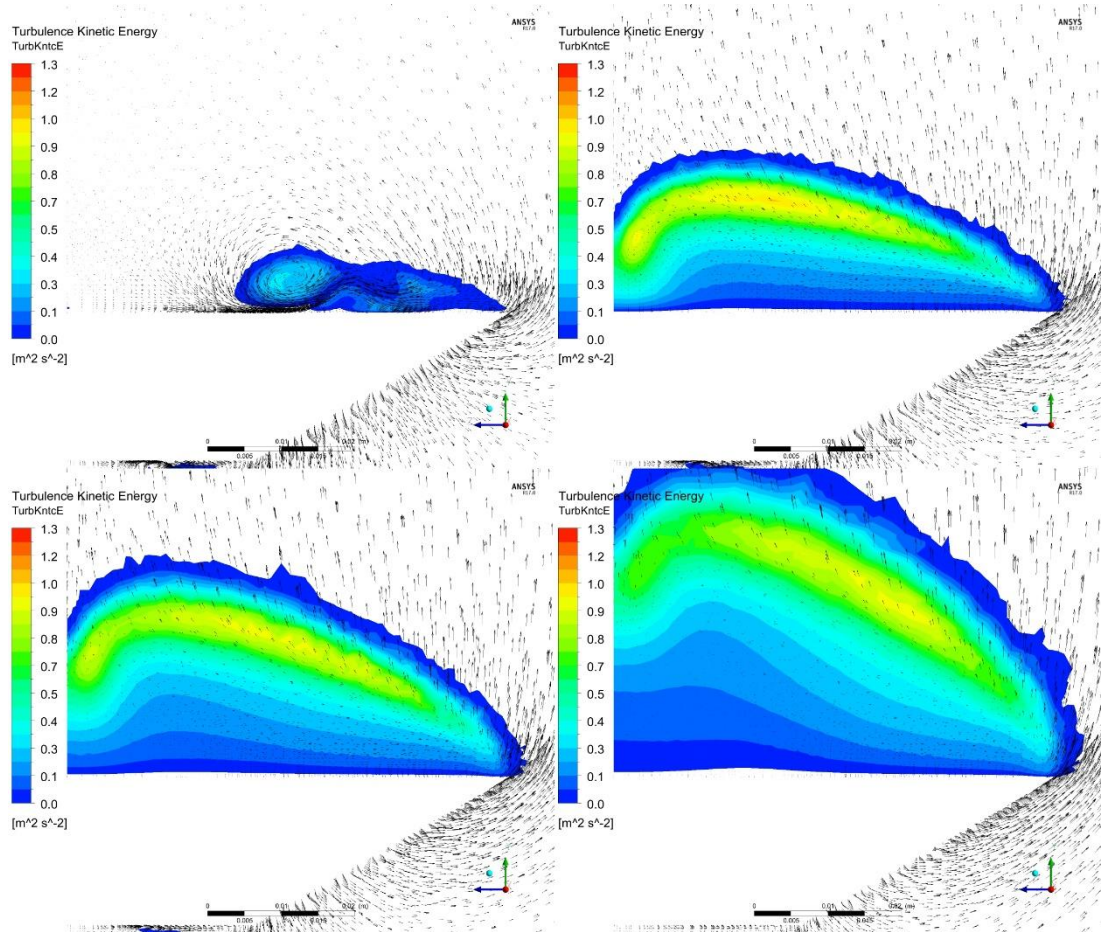


Figure 4.13. The comparisons of turbulent kinetic energy contours of delta wing with $t/c = 0.1900$ at $RE = 35000$ and $\alpha = 3^\circ, 9^\circ$ (top), $14^\circ, 20^\circ$ (bottom) located at $x/c = 0.44$

To observe whether thickness-to-chord ratio has a similar influence at a different flight condition, Reynolds Number of the flow is 300000 for the same angles of attack. It can be seen in the Figure 4.14 and Figure 4.15 that increasing the angle of attack pushes the vortical structures in the normal direction of the leeward surface of the wing as expected and thickness-to-chord ratio is also reducing the magnitude of turbulent kinetic energy and vorticity except for $\alpha=3^\circ$.

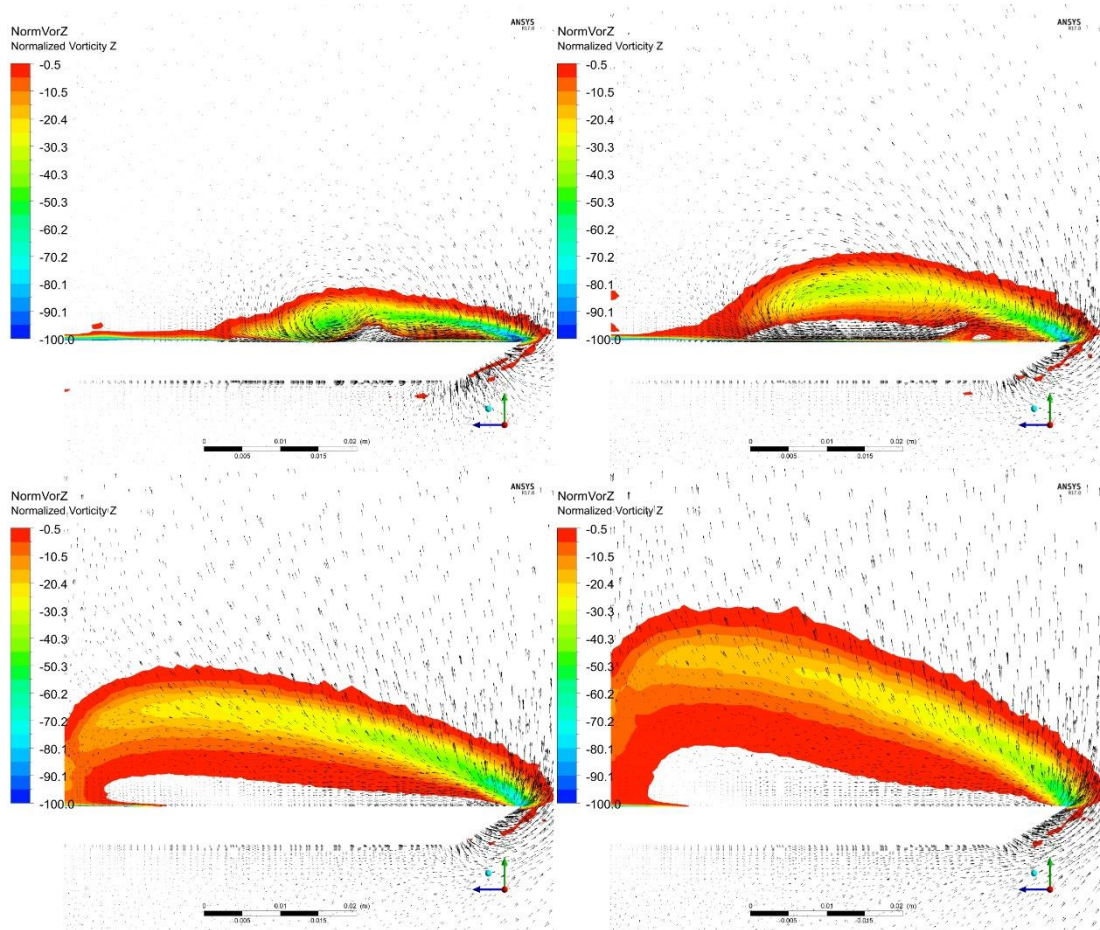


Figure 4.14. The comparisons of azimuthal vorticity contours of delta wing with $t/c = 0.0475$ at $RE = 300000$ and $\alpha = 3^\circ, 9^\circ, 14^\circ, 20^\circ$ (top) located at $x/c = 0.44$

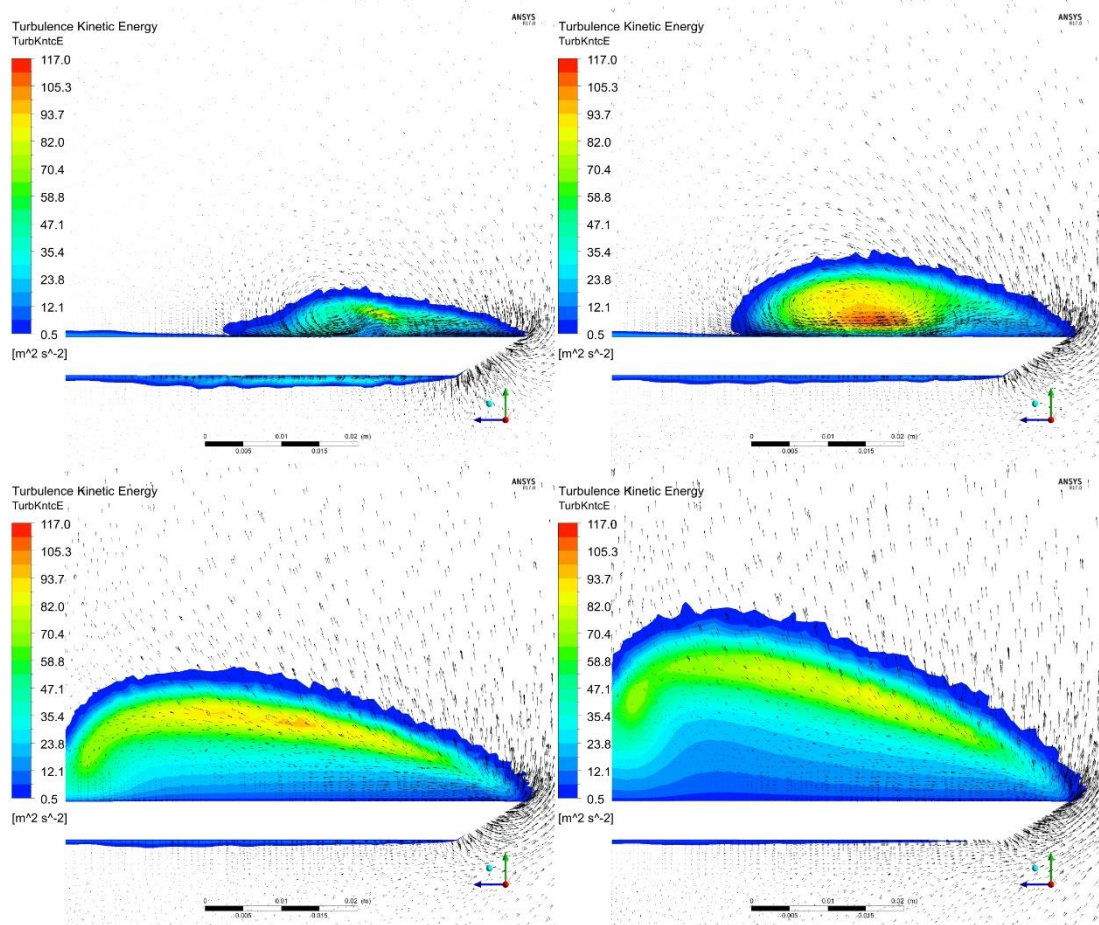


Figure 4.15. The comparisons of turbulent kinetic energy contours of delta wing with $t/c = 0.0475$ at $RE = 300000$ and $\alpha = 3^\circ, 9^\circ, 14^\circ, 20^\circ$ (top), $14^\circ, 20^\circ$ (bottom) located at $x/c = 0.44$

In Figure 4.16 and Figure 4.17, increasing thickness-to-chord ratio is seen to push the vortical structures even further in the normal direction for all angles of attack, reducing the magnitude of vorticity and turbulent kinetic energy but enlarging the area where the three-dimensional flow separation and flow reversal occur.

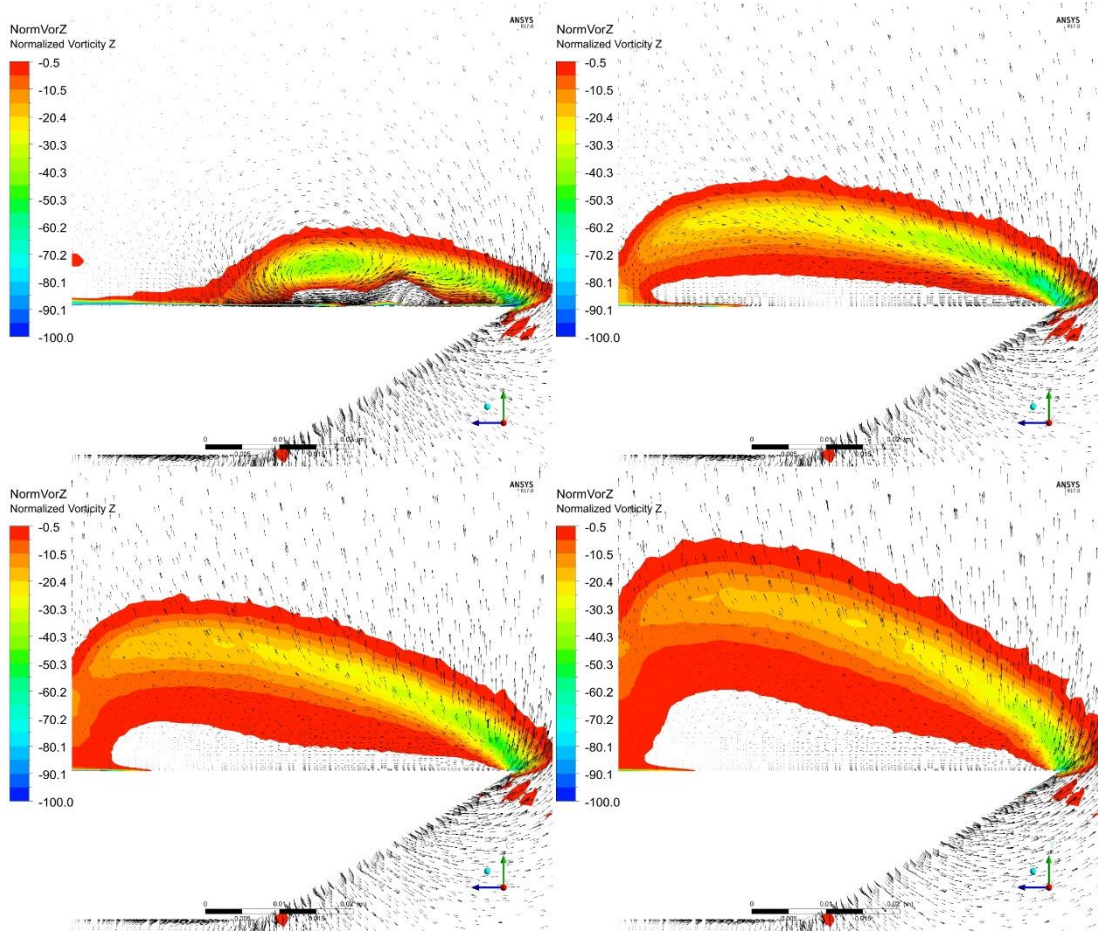


Figure 4.16. The comparisons of azimuthal vorticity contours of delta wing with $t/c = 0.1900$ at $RE = 300000$ and $\alpha = 3^\circ, 9^\circ$ (top), $14^\circ, 20^\circ$ (bottom) located at $x/c = 0.44$

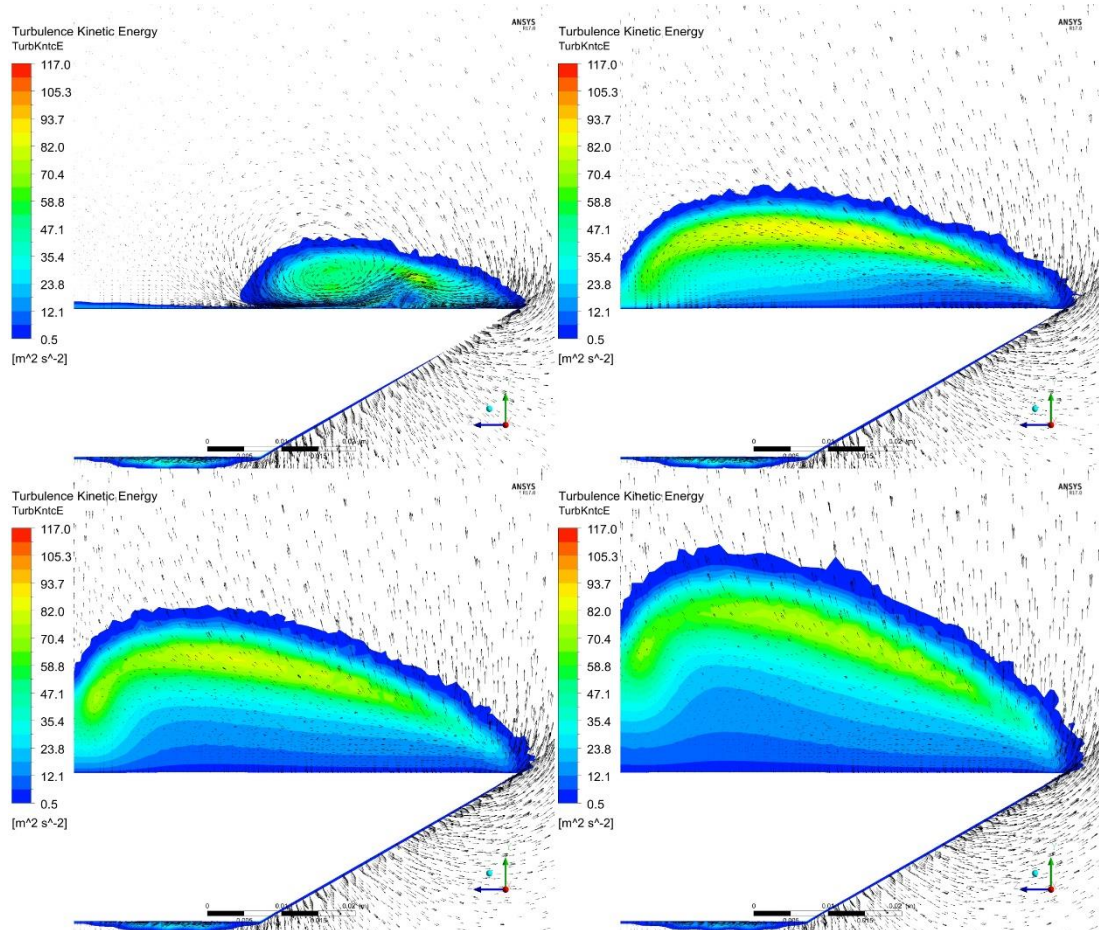


Figure 4.17. The comparisons of turbulent kinetic energy contours of delta wing with $t/c = 0.1900$ at $RE = 300000$ and $\alpha = 3^\circ, 9^\circ, 14^\circ, 20^\circ$ (top), $14^\circ, 20^\circ$ (bottom) located at $x/c = 0.44$

The results indicate that thickness-to-chord ratio has significant effects on the flow structure of the delta wing in terms of promoting the three-dimensional flow separation process which can lead to the loss of lift and control.

4.2. Aerodynamic Performance

As well as the flow field properties, aerodynamic performance of the delta wings are heavily affected by the change in the thickness-to-chord ratios. This part of the study will include detailed information about the variance in the aerodynamic coefficients with respect to the parameters which are defined in the CFD matrix.

Figure 4.18 shows the lift coefficient, CL values of the delta wings with varying thickness-to-chord ratio and Reynolds number as a function of angle of attack. It is seen from the results that increasing the thickness-to-chord ratio significantly decreases the CL value for a given Reynolds number in a broad range of angle of attack. Although it is seen that increasing the thickness produced higher values of CL for low angles of attack, it also caused the delta wings to get stall in a lower value of angle of attack. On the other hand, increasing the Reynolds number, even it makes the vortex breakdown earlier, increased the lift capacity of the wings at all conditions and pushed the stall angle of attack further.

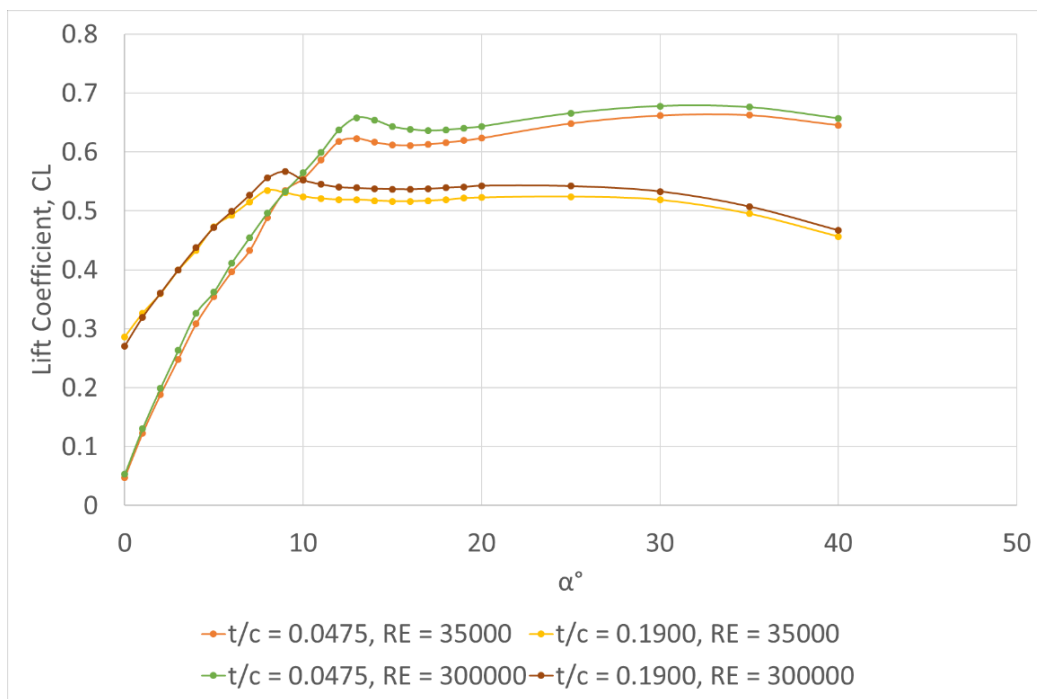


Figure 4.18. Comparison of the lift coefficient, CL at RE = 35000 & 300000 for $t/c = 0.0475, 0.1900$

Figure 4.19 shows that the drag coefficient of the delta wings has both increased with the increase in the thickness-to-chord ratio and Reynolds number. The increase in drag with the increase in the Reynolds number is expected and another contributing factor in play is the frontal area increase by higher thickness-to-chord ratio. In other words, the area which is subjected to the high-pressure field in the windward surface of the delta wing, is larger. Therefore, increased drag by the increased thickness of the wing is also expected.

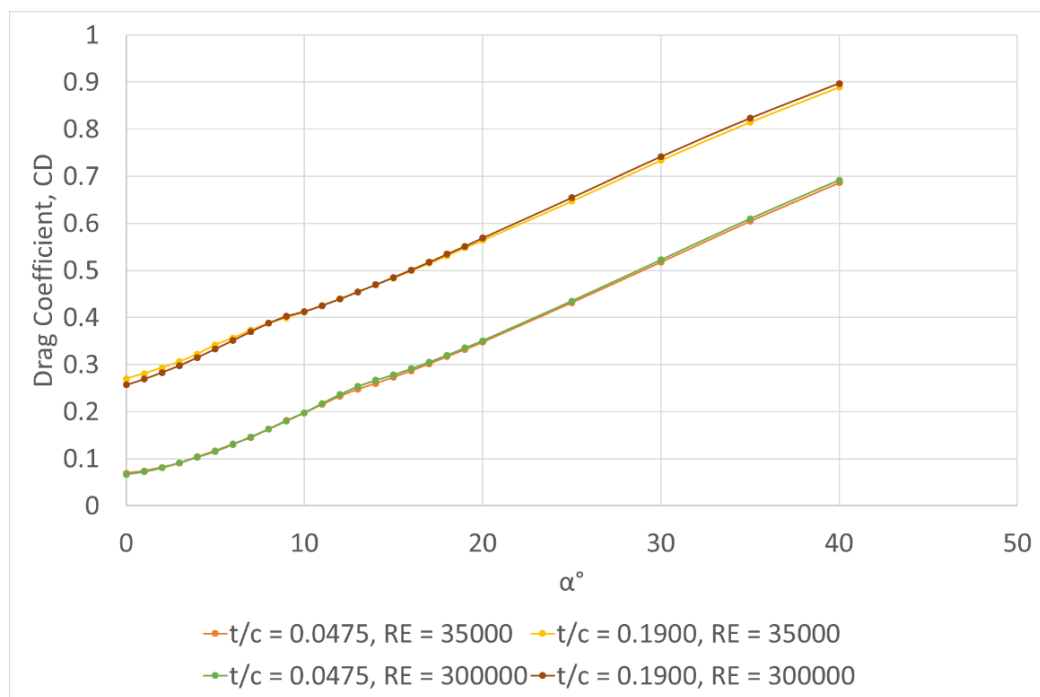


Figure 4.19. Comparison of the drag coefficient, CD at RE = 35000 & 300000 for $t/c = 0.0475$, 0.1900

To assess the wing effectiveness, CL/CD ratios are given in the Figure 4.20. Lift to drag ratios increased with the increase in the Reynolds number. However, judging by the results, increasing the thickness-to-chord ratio has deteriorated the wing effectiveness in a severe manner.

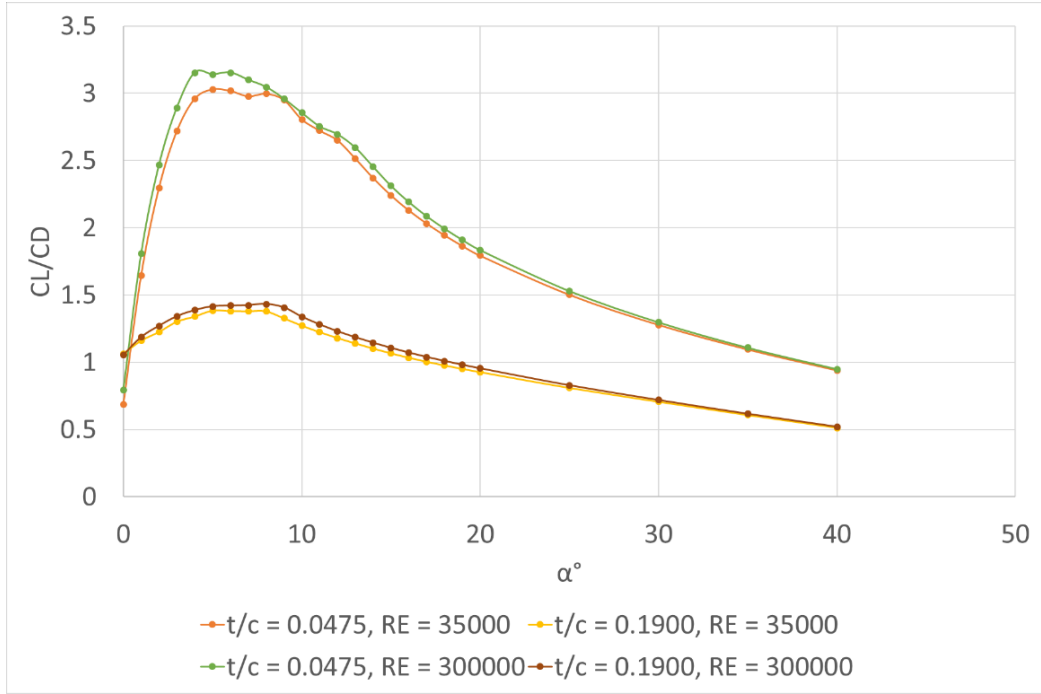


Figure 4.20. Comparison of the CL/CD at RE = 35000 & 300000 for $t/c = 0.0475, 0.1900$

The pitching moment coefficient C_m , is an important marker identifying the maneuvering capability of the delta wing. To calculate this coefficient, a center of gravity (c.g.) is assumed to be located at the delta wing's geometric center. Figure 4.21 shows the variance in the C_m values of the wing with different t/c under different Reynolds number as a function of angle of attack. At low angles of attack, increasing the thickness-to-chord ratio has increased the value of the pitching moment coefficients. At high angles of attack, the C_m value of the thicker wing is significantly lower than the values exhibited by the thin wing. Moreover, it is seen that for the wing with $t/c = 0.0475$, between angles of attack of 20° and 35° , pitching moment coefficient is again increasing at $RE = 35000$ but same phenomenon is not present when thickness-to-chord ratio is increased.

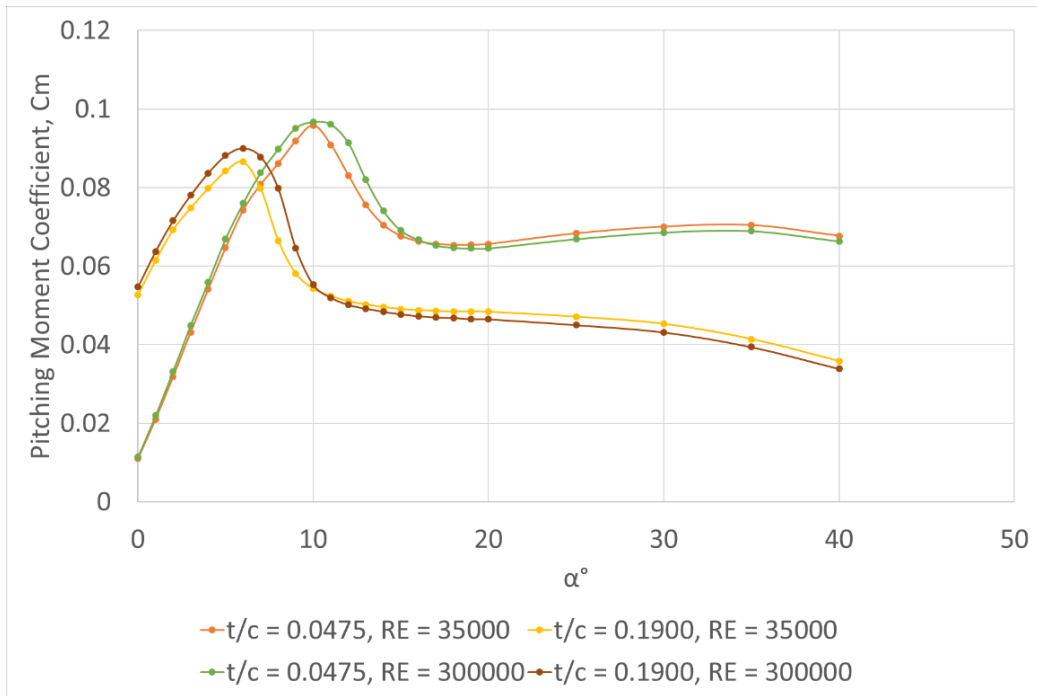


Figure 4.21. Comparison of the pitching moment coefficient, C_m at $RE = 35000$ & 300000 for $t/c = 0.0475, 0.1900$

For an airframe to be statically stable, C_m values are required to be negative for positive angle of attacks at trim conditions [70]. It is seen in the Figure 4.21 that at all conditions the pitching moment of the wings are above zero for all angles of attack leading to the condition where a small increase in the angle of attack increases the C_m values which in turn cause a further increase in the α values. For that reason, wings are statically unstable. In all cases, this situation can arise when the location of the center of pressure is in front of the center of gravity. To verify the instability of the wings, the location of the center of pressure ($X_{c.p.}$) is given in the Figure 4.22 with respect to varying angles of attack at all Reynolds numbers for wings with $t/c = 0.0475$ & 0.1900 . The location of the c.g. at x-axis is $x = 0.071$ m. From the calculations, it is seen that with the increase in the thickness-to-chord ratio, $X_{c.p.}$ moves closer to the center of gravity. However, at all flight conditions, center of pressure always lies in front of the center of gravity.

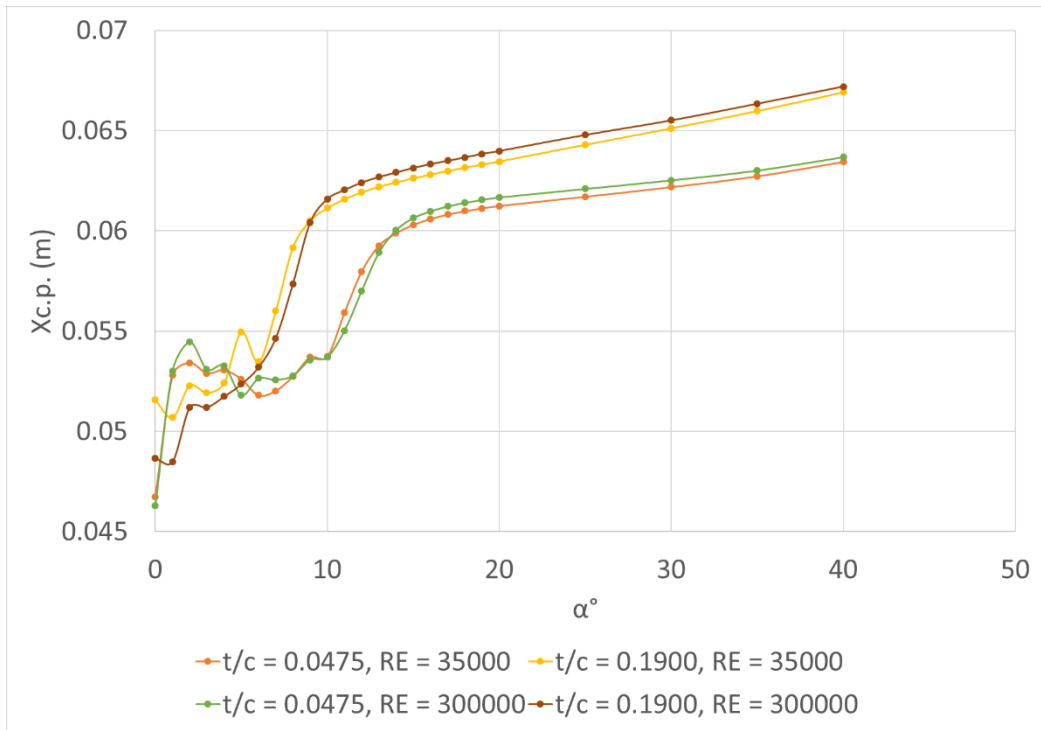


Figure 4.22. Comparison of the location of the center of pressure (Xc.p.) at x-axis with respect to angle of attack, at RE = 35000 & 300000 for $t/c = 0.0475, 0.1900$

The second set of the CFD matrix is analyzed to have a complementary aerodynamic data set to assess two more thickness-to-chord ratios under same flow regime. Same calculations have been conducted for the wing with $t/c = 0.019, 0.1143$ at sample angles of attack, $\alpha = 5^\circ, 9^\circ, 13^\circ$ and 17° . Figure 4.23 and Figure 4.24 indicate that the effects of thickness-to-chord ratio and Reynolds number stands the same as in the previous analysis set. The lift coefficient value is highest at the thinnest wing and lowest with thickest wing, except for the low angles of attack. Also, lowest drag coefficient value is seen with the case of the thinnest wing whereas the highest value is produced with the thickest delta wing. Figure 4.25 reveals that the initial assessment of the performances of the delta wings is also valid as well. Thinnest wing achieved the highest CL/CD value while increasing the t/c degenerated the performance of the wing planform for all Reynolds numbers.

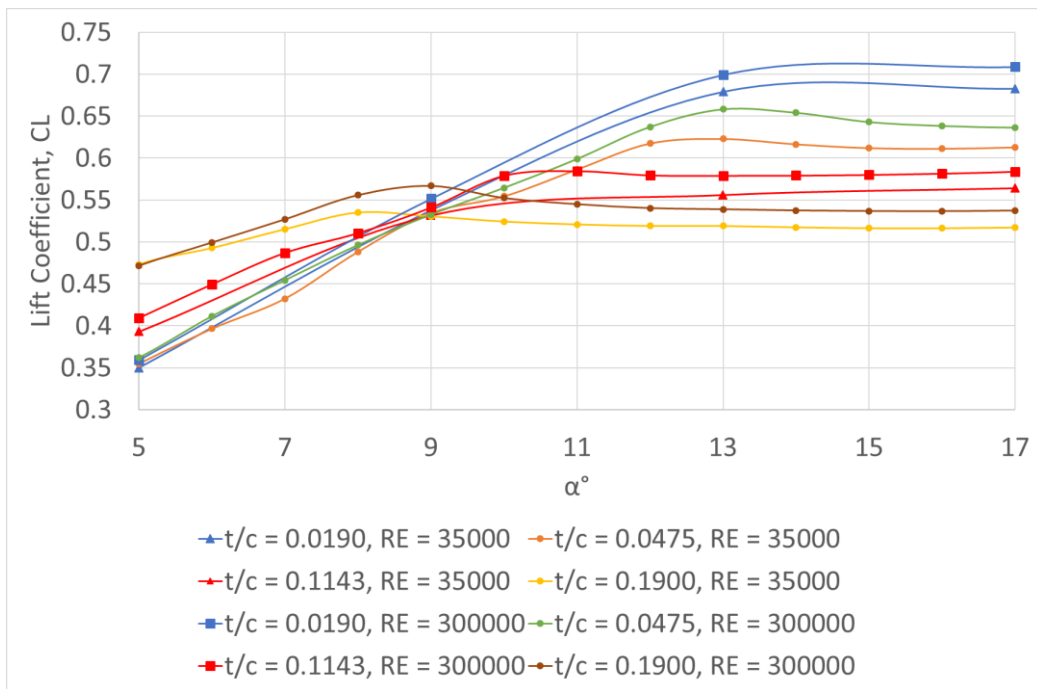


Figure 4.23. Comparison of the lift coefficient, CL at RE = 35000 & 300000 for $t/c = 0.0190, 0.0475, 0.1143, 0.1900$

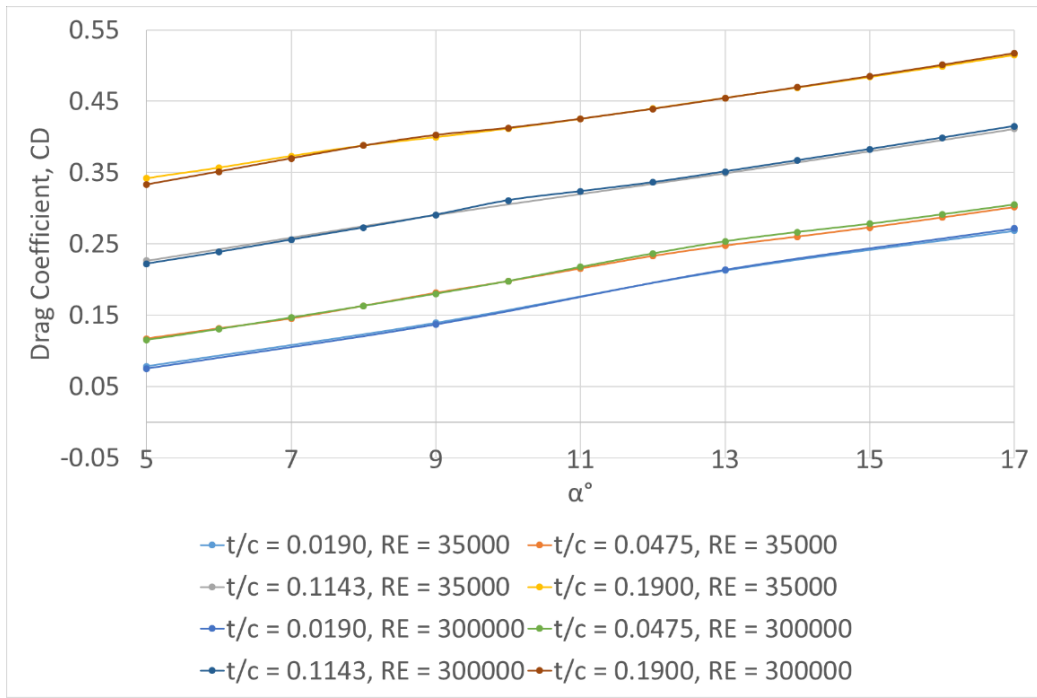


Figure 4.24. Comparison of the drag coefficient, CD at RE = 35000 & 300000 for $t/c = 0.0190, 0.0475, 0.1143, 0.1900$

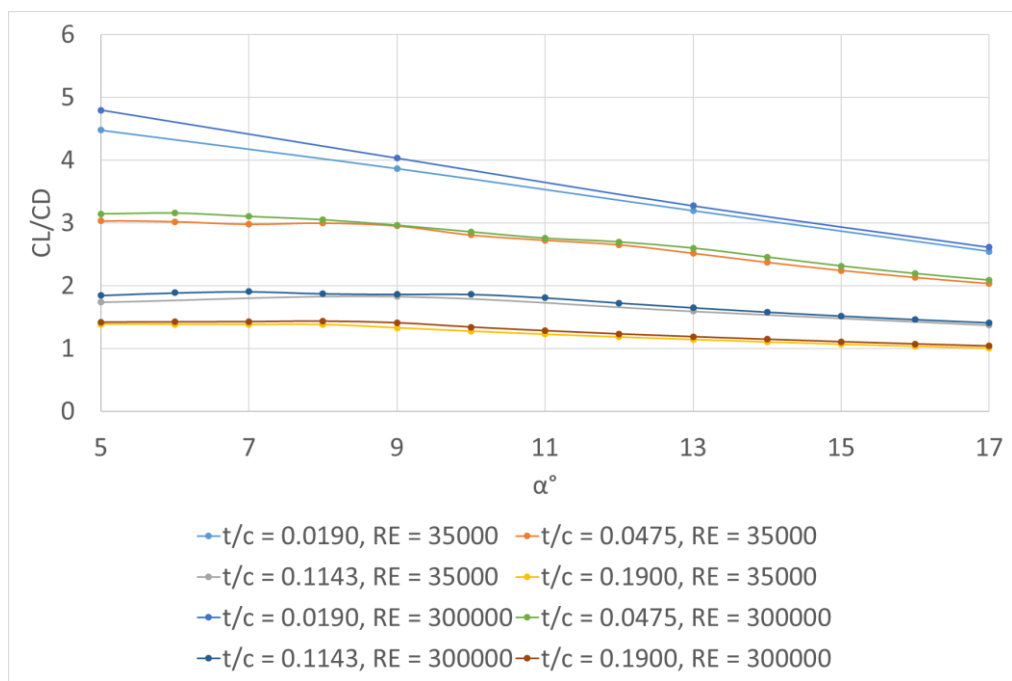


Figure 4.25. Comparison of the CL/CD values at RE = 35000 & 300000 for $t/c = 0.0190, 0.0475, 0.1143, 0.1900$

CHAPTER 5

CONCLUSIONS

5.1. Summary and Conclusions

A delta wing with sweep angle of 35° is modelled under the same conditions which is captured from the experimental study of Gülsançan [7] in order to validate the numerical results obtained after conducting the mesh independency study. As the numerical model, incompressible SIMPLE solver algorithm along with the turbulence model SST k- ω with curvature correction extension is selected for its success at capturing the vortical flow field properties.

After the results from the numerical scheme and grid is validated by the experimental results, an investigation for the thickness-to-chord ratio effects on the flow field and the aerodynamic performance has been conducted at a broader range of angle of attack and an additional Reynolds number.

Results derived from the flow visualization show that increasing the thickness-to-chord ratio of a delta wing shift the location of the vortex core line to the centerline of the wing. Moreover, same increase has manifested itself on the focal points and the swirling structure on the leeward surface of the wing to move to the trailing edge of the wing. Additionally, increasing the thickness-to-chord ratio also promoted the 3D flow separation from the leeward surface of the wing, and enlarged the region where the flow reversal phenomenon is seen.

Thickness-to-chord ratio also significantly alters the aerodynamic performance of the delta wings. Increasing t/c for all flow regimes has affected to performance to degrade for all angles of attack except a small region where α is low. Even then maximum lift coefficients of the delta wings had a decreasing trend while thickness-to-chord ratio is increasing. For all cases, drag coefficient is increased by the

increase in the wing thickness as expected. Considering the effectiveness of the delta wings, CL/CD ratios tend to be higher when the wing thickness is decreased for all angles of attack. To have a complimentary result two additional wing thickness were analyzed under sample angles of attack and found out that the initial behavior stemmed from the thickness-to-chord ratio stands. Moreover, as it is derived from the aerodynamic database based on the CFD matrix, flow regime has a very little role concerning the stability of the wings. On the other hand, increasing the thickness-to-chord ratio is the major contributing factor for the angle of attack cap where delta wings start to stabilize

5.2. Recommendations for Future Work

This thesis study is conducted to identify the effects of the thickness-to-chord ratio on the flow field and the aerodynamic performance of the delta wings. As concluded, increasing the thickness-to-chord ratio caused detrimental effects to the beneficial qualities that come with the strong and stable leading-edge vorticities. To remedy the current drawbacks, a flow control method can be utilized to increase the longevity of the leading-edge vorticities and to modify the flow field in a benevolent manner.

Moreover, viewing from a design perspective and considering solely the aerodynamic performance, a parametric delta wing design study could be conducted for a multi-objective optimization study, utilizing the commercial optimization tools to achieve a desired aerodynamic performance and stability metrics from a delta wing under various conditions in which the effects of multiple parameters such as, the thickness-to-chord ratio, leading-edge bevel angle, wing sweep angle, the variations on the root chord and wing span and leading-edge radius can be examined altogether.

REFERENCES

- [1] M. Allan, “A CFD Investigation of Wind Tunnel Interference on Delta Wing Aerodynamics” Ph.D. Thesis, Department of Aerospace Engineering, University of Glasgow, 2002.
- [2] A. Raza, H. Rahman, K. Ahmad, S. Khushnood, “Experimental and Computational Investigation of Delta Wing Aerodynamics”, *International Bhurban Conference on Applied Sciences & Technology (IBCAST)*, 2013.
- [3] S. Z. Pirzadeh, “Vortical Flow Prediction Using an Adaptive Unstructured Grid Method”, *RTO AVT Symposium on Advanced Flow Management, Part A – Vortex Flows and High Angle of Attack for Military Vehicles*, 2001.
- [4] L. S. Ko, T. Lee, “Aerodynamics and Vortex Flowfield of a Slender Delta Wing with Apex Flap and Tip Flap”, *Journal of Fluids Engineering*, 2016.
- [5] S. Görtz, “Realistic Simulations of Delta Wing Aerodynamics Using Novel CFD Methods”, Ph.D. Thesis, Department of Aeronautical and Vehicle Engineering, Royal Institute of Technology (KTH), 2005.
- [6] G. S. Taylor, I. Gursul, “Buffeting Flows over a Low-Sweep Delta Wing”, *AIAA Journal*, vol. 42, no. 9, pp. 1737-1745, 2004.
- [7] B. Gülsuçan, “Effect of Thickness-to-Chord Ratio on Flow Structure of a Low Swept Delta Wing”, M.S. Thesis, Dept. Mech. Eng. Dept., METU., Ankara, Turkey, Sept 2017.
- [8] A. Pelletier, R. C. Nelson, “The Unsteady Aerodynamics of Slender Wings and Aircraft Undergoing Large Amplitude Maneuvers”, *Progress in Aerospace Science*, vol.39, pp. 185-248, 2003.
- [9] M. R. Visbal, “Computational and Physical Aspects of Vortex Breakdown on Delta Wings”, *33rd Aerospace Science Meeting & Exhibit*, Jan 1995.

- [10] D. Hummel, “Effects of Boundary Layer Formation on the Vortical Flow above Slender Delta Wings”, *RTO AVT Specialists’ Meeting on Enhancement of NATO Military Flight Vehicle Performance by Management of Interacting Boundary Layer Transition and Separation*, 2004.
- [11] H. Werle’, “Quelques résultats expérimentaux sur les ailes en flèche, aux faibles vitesses, obtenus en tunnel hydrodynamique” *La Recherche Aéronautique*, no. 41, pp. 15-21, 1954
- [12] D. W. Bryer, N. C. Lambourne, “The Bursting of Leading-Edge Vortices Some Observations and Discussion of the Phenomenon”, *Aeronautical Research Council Reports and Memoranda*, Ministry of Aviation, no. 3282, 1962.
- [13] F. M. Payne, T. Terry, R. C. Nelson, “Visualization of Leading-Edge Vortices on a Series of Flat Plate Delta Wings”, *NASA Contractor Report 4320, University of Notre Dame*, 1991.
- [14] N. C. Lambourne, D. W. Bryer, “The Bursting of Leading-Edge Vortices - Some Observations and Discussion of the Phenomenon”, *Aeronautical Research Council Reports and Memoranda, Ministry of Aviation*, no. 3282, 1962.
- [15] I. Gursul, “Review of Unsteady Vortex Flows Over Slender Delta Wings”, *Journal of Aircraft*, vol. 42, no. 2, pp. 299-319, Mar.-Apr., 2005.
- [16] L. Zhang, X. Deng, “Detached-eddy Simulation of Subsonic Flow Past a Delta Wing”, *Procedia Engineering Article*, Dec 2015.
- [17] M. Zharfa, I. Ozturk, M. M. Yavuz, “Flow Structure on Nonslender Delta Wing: Reynolds Number Dependence and Flow Control”, *AIAA Journal*, vol.54, no.3, pp. 880-897, Jan. 2016.
- [18] M. Elsayed, N.G. Verhaagen, “Leading-Edge Radius Effects on 50° Delta Wing Flow”, *47th AIAA Aerospace Sciences Meeting*, 2009.

- [19] I. Gursul, W. Xie, “Origin of Vortex Wandering over Delta Wings”, *Journal of Aircraft*, vol. 37, no. 2, pp. 348-350, 2000.
- [20] M. Menke, I. Gursul, “Unsteady Nature of Leading-Edge Vortices”, *Physics of Fluids*, vol. 9, no. 10, pp. 1-7, 1997.
- [21] S. Kommallein, D. Hummel, “LDA Investigations of the Separated Flow Over Slender Wings”, *Physics of Separated Flows Numerical and Experimental and Theoretical Aspects*, pp. 275–282, 1993.
- [22] K. C. Cornelius, “Analysis of Vortex Bursting Utilizing Three-Dimensional Laser Measurements”, *Journal of Aircraft*, vol. 32, no. 2, pp. 297–306, 1995.
- [23] D. Degani, G. G. Zilliac, “Experimental Study of Non steady Asymmetric Flow Around an Ogive-Cylinder at Incidence”, *AIAA Journal*, vol. 28, no. 4, pp. 642–649, 1990.
- [24] Baker, G. R., Barker, S. J., Bofah, K. K., and Saffman, P. G., “Laser Anemometer Measurements of Trailing Vortices in Water”, *Journal of Fluid Mechanics*, vol. 65, Pt. 2, 1974, pp. 325–336.
- [25] P. B. Earnshaw, “An Experimental Investigation of the Structure of a Leading-Edge Vortex”, *R.A.E. Tech. Note*, no. Aero 2740, 1961.
- [26] M. Ozgoren, B. Sahin, and D. Rockwell, “Vortex Structure on a Delta Wing at High Angle of Attack”, *AIAA Journal*, vol. 40, no. 2, pp. 285–292, 2002.
- [27] A. J. Riley, M. V. Lawson, “Development of a Three-Dimensional Free Shear Layer”, *Journal of Fluid Mechanics*, vol. 369, pp. 49–89, 1998.
- [28] R. E. Gordnier, M. R. Visbal, “Compact Difference Scheme Applied to Simulation of Low-Sweep Delta Wing Flow”, *AIAA Journal*, vol. 43, no. 8, pp. 1744–1752, 2005.

- [29] I. Gursul, Z. Wang, E. Vardaki, “Review of Flow Control Mechanisms of Leading-Edge Vortices”, *Progress in Aerospace Sciences*, vol. 43, no. 7–8, pp. 246–270, 2007.
- [30] A. Kölzsch, C. Breitsamter, “Vortex-Flow Manipulation on a Generic Delta Wing Configuration”, *Journal of Aircraft*, vol. 51, no. 5, pp. 1380–1390, 2014.
- [31] Çelik, Çetin, Yavuz, “Effect of Passive Bleeding on Flow Structure over a Nonslender Delta Wing”, *AIAA Journal*, vol. 55, no. 8, August 2017.
- [32] M. R. Visbal, D. V. Gaitonde, “Control of Vortical Flows Using Simulated Plasma Actuators”, *44th AIAA Aerospace Sciences Meeting and Exhibit*, January 2006.
- [33] S. Phillips, C. Lambert, I. Gursul, “Effect of a Trailing-Edge Jet on Fin Buffeting Introduction”, *Journal of Aircraft*, vol. 40, no. 3, pp. 590–599, 2003.
- [34] İ. C. Küçükyılmaz, “Control of Flow Structure on 70° Swept Delta Wing with Along-the-core Blowing Using Numerical Modelling”, M.S. Thesis, Dept. Mech. Eng. Dept., METU., Ankara, Turkey, Jan 2016.
- [35] A. M. Mitchell, J. Delery, “Research into Vortex Breakdown Control”, *Progress in Aerospace Sciences*, vol. 37, no. 4, pp. 385-418, May 2001.
- [36] L. E. Ericsson, M. View, “Effect of Leading-Edge Cross-Sectional Shape on Nonslender Wing Rock”, *Journal of Aircraft*, vol. 40, no. 2, pp. 407–410, 2003.
- [37] J. M. Délery, “Robert Legendre and Henri Werlé: Toward the Elucidation of Three-Dimensional Separation”, *Annual Rev. Fluid Mechanics*, vol. 33, no. 1, pp. 129–154, 2001.

- [38] H. Werle, “Bursting of Conical Vortex Sheet above Delta Wing Surface at Low Speeds”, *La Rech. Aeronaut.*, no. 74, pp. 25–30, 1960.
- [39] D. H. Peckham, “Low-Speed Wind-Tunnel Tests on a Series of Uncambered Slender Pointed Wings with Sharp Edges”, *R&M 3186*, 1958.
- [40] R. D. Witcofski, D. C. Marcum, Jr., “Effect of Thickness and Sweep Angle on the Longitudinal Aerodynamic Characteristics of Slab Delta Planforms at a Mach Number of 20”, *TN-D 3459*, 1966.
- [41] M. V. Lawson, A. J. Riley, “Vortex Breakdown Control by Delta-Wing Geometry”, *Journal of Aircraft*, vol. 32, no. 4, pp. 832–838, 1995.
- [42] J. J. Wang, S. F. Lu, “Effects of Leading-Edge Bevel Angle on the Aerodynamic Forces of a Non-slender 50 Degree Delta Wing”, *Aeronautical Journal*, vol. 109, no. 1098, pp. 403–407, 2005.
- [43] M. S. Ghazijahani, M. M. Yavuz, “Effect of thickness-to-chord ratio on aerodynamics of non-slender delta wing”, *Aerospace Science and Technology*, vol. 88, p.298-307, 2019.
- [44] H. Kawazoe, Y. Nakamura, T. Ono, Y. Ushimaru, “Static and Total Pressure Distributions around a Thick Delta Wing with Rounded Leading Edge”, *25th AlAA Plasmadynamics Lasers Conference*, 1994.
- [45] J. Saltzman, T. G. Ayers, “Review of Flight-to-Wind-Tunnel Drag Correlation Edwin”, *Journal of Aircraft*, vol. 19, no. 10, pp. 801–811, 1982.
- [46] M. Mitchell, A. Morton, J. R. Forsythe, M. Cummings, “Analysis of Delta-Wing Vortical Substructures Using Detached-Eddy Simulation”, *AIAA Journal*, vol. 44, no.5, May 2006.
- [47] S. Görtz, “Detached-Eddy Simulations of a Full-Span Delta Wing at High Incidence”, *21st Applied Aerodynamics Conference*, 2003.

- [48] J. Roy, I. Mary, O. Rodriguez, "CFD Solutions of 70° Delta Wing Flows", *21st Applied Aerodynamics Conference*, 2003.
- [49] S. H. Peng, A. Jirasek, "Verification of RANS and Hybrid RANS-LES Modelling in Computations of a Delta-Wing Flow", *46th AIAA Fluid Dynamics Conference*, 2016.
- [50] J. Cai, S. Pan, W. Li, Z. Zhang, "Numerical and experimental investigations of a Nonslender Delta Wing with Leading-Edge Vortex Flap", *Computers & Fluids*, vol. 99, pp. 1-17, 2014.
- [51] A. M. Mitchell, "Experimental Data Base Selected for Numerical and Analytical Validation and Verification: ONERA 70-Deg Delta Wing'", *NATO RTO-TR-AVT-080*, chapter-3.
- [52] A. Kumar, K. Onkar, M. Manjuprasad, "Fluid-Structure Interaction Analysis of a Cropped Delta Wing", *12th International Conference on Vibration Problems*, 2015.
- [53] D. Missirlis, M. Kyriakou, K. Yakinthos, "Numerical modelling of the vortex breakdown phenomenon on a delta wing with trailing-edge jet-flap", *International Journal of Heat and Fluid Flow*, 2010.
- [54] C. Shih, Z. Ding, "Trailing edge jet flap of leading-edge vortices of delta wings", *AIAA Journal*, vol. 34, no. 7, 1996.
- [55] A. Mitchell, S. Morton, P. Morton, Y. Guy, "Flow Control of Vortical Structures and Vortex Breakdown Over Slender Delta Wings", *RTO NATO Advanced Flow Management: Part A – Vortex Flows and High Angle of Attack for Military Vehicles*, 2001.
- [56] G. Sharma, M. Naimuddin, G. Chopra, J. Sinha, G. Sharma, "Numerical Analysis of Flow Field over Compound Delta Wing at Subsonic and Supersonic Speeds", *IEEE Aerospace Conference*, 2016.

- [57] M. R. Allan, K. J. Badcock, B. E. Richards, “A CFD Investigation of Wind Tunnel Wall Influences on Pitching Delta Wings”, *24th AIAA Applied Aerodynamics Conference*, 2002.
- [58] M. Naimuddin, G. Chopra, G. Sharma, “Experimental & Computational Study on Compound Delta Wing”, *Journal of Basic and Applied Engineering Research*, 2014.
- [59] H. Golparvar, S. Irani, M.M. Sani, “Experimental Investigation of Linear and Nonlinear Aeroelastic Behavior of a Cropped Delta Wing with Store in Low Subsonic Flow”, *The Brazilian Society of Mechanical Sciences and Engineering*, 2015.
- [60] W. Huang, S. Li, L. Yan, J. Liu, “Mixing Enhancement Induced by a Delta Wing in Supersonic Flows”, *Turbomachinery Technical Conference and Exposition*, 2016.
- [61] "H. Luedeke, “Unsteady CFD Analysis of a Delta Wing Fighter Configuration by Delayed Detached Eddy Simulation”, *NNFM*, 2008.
- [62] A. Haque, J. Khawar, S. R. Ch, “Influence of Turbulence Modeling in Capturing Separated Flow Over Delta Wing at Subsonic Speed”, *Engineering Applications of Computational Fluid Mechanics*, vol. 2, no. 3, pp. 252-263, 2008.
- [63] S. Crippa, “Numerical Solutions for the VFE-2 Configuration on Unstructured Grids at KTH”, *NATO RTO-TR-AVT-113*, chapter 30, pp. 1-36.
- [64] S. Saha, B. Majumdar, “Flow Visualization and CFD Simulation on 65° Delta Wing at Subsonic Condition”, *Procedia Engineering*, vol. 38, pp. 3086-3096, 2012.
- [65] R. M. Cummings, S. A. Morton, S. G. Siegel, “Numerical Prediction and Wing Tunnel Experiment for a Pitching Unmanned Combat Air Vehicle”, *Aerospace Science and Technology*, vol. 12, pp. 355-364, July 2008.

- [66] S.E. Sayılır, “Control of Flow Structure on VFE-2 Delta Wing with Passive Bleeding Using CFD”, M.S. Thesis, Dept. Mech. Eng. Dept., METU., Ankara, Turkey, Jan 2018.
- [67] F. R. Menter, “Two-Equation Eddy-Viscosity Turbulence Models for Engineering Applications”, *AIAA Journal*, vol. 32, no. 8, pp. 1598-1605, 1994.
- [68] P. E. Smirnov, F. R. Menter, “Sensitization of the SST Turbulence model to Rotation and Curvature by Applying the Spalart-Shur Correction Term”, *Proceedings of ASME Turbo Expo 2008: Power for Land, Sea and Air*, GT2008-50480, 2008.
- [69] L.W. Traub, B. Moeller, O. Rediniotis, “Low-Reynolds-Number Effects on Delta-Wing Aerodynamics”, *Journal of Aircraft*, vol. 35, no. 4.
- [70] E. L. Fleeman, “Tactical Missile Design”, *AIAA Education Series*, AB053-02, p. 69-71, June 2001.